Final Report

for the

Compact, Low-Cost, Light-Weight, Superconducting, Ironless Cyclotrons for Hadron Radiotherapy

U.S. Department of Energy
Office of High Energy Physics
Accelerator Stewardship Program
Federal Award Identification Number: DE-SC0013499

April 4, 2019

by

Joseph V. Minervini
Leslie Bromberg
Philip Michael
Alexey Radovinsky

Massachusetts Institute of Technology
Plasma Science and Fusion Center
Magnets and Cryogenics Division

and
Daniel Winklehner

Massachusetts Institute of Technology
Department of Physics
Laboratory for Nuclear Science

77 Massachusetts Avenue
Cambridge, MA 02139

Table of Contents

Table of Tables

Table of Figures

Acknowledgements

This work was carried out under a grant from the U.S. Department of Energy, Office of High Energy Physics, Accelerator Stewardship Program, Federal Award Identification Number: DE-SC0013499. This was a joint award with ProNova Solutions, Inc[1]. We are especially grateful to Dr. Vladimir Derenchuk, Mr. Niek Schreuder, Mr. Joseph Matteo, and Mr. Jeff Pelletier for the valuable contributions to beam physics and clinical treatment requirements for the proton beam, as well as for understanding of the commercial aspects of proton radiotherapy.

---

[1] https://provisionhealthcare.com/about-us/innovative-solutions/proton-therapy-system/

Executive Summary

Superconducting cyclotrons are increasingly employed for proton beam radiotherapy treatment (PBRT). The use of superconductivity in a cyclotron design can reduce its mass by an order of magnitude and size by a factor of 3-4 over conventional resistive magnet technology, yielding significant reduction in overall cost of the device, the accelerator vault, and its infrastructure, as well as reduced operating costs. At MIT, previous work was focused on developing a very high field (9 T at the pole face) superconducting synchrocyclotron that resulted in a highly compact device that is about an order of magnitude lighter, and much smaller in diameter than a conventional, resistive cyclotron. This comparison is shown in the Introduction Section 1 .The results of the study reported here were focused on a conceptual design for a compact superconducting synchrocyclotron to demonstrate the possibility to further reduce its weight by almost another order of magnitude by eliminating all iron from the device. In the absence of magnetic iron poles, the magnetic field profile in the beam gap is achieved through a set of main superconducting split pair coils energized in series with a set of distributed field-shaping superconducting coils External magnetic field shielding is achieved through a set of outer, superconducting ring coils, also connected in series with the other coils, to cancel the stray magnetic field. These shielding coils replace the heavy iron yoke which is the conventional method to return the magnetic flux. It is noted that the 10 Gauss surface is located at a radius of about 3.5 m comparable in both ironless and conventional devices, even in the absence of iron in the ironless device. These concepts are introduced in Section 0.

Radiotherapy requirements for a 230 MeV/u proton beam are given in Section 0 and general requirements for the synchrocyclotron are given in Sections 0 and 0.

An important result from eliminating all magnetic iron in the flux circuit is the resulting linear relationship between the operating current and the magnetic field intensity. In the case with iron, the saturation of the magnetic field forces operation at one value of magnetic field. This feature design then enables continuous beam energy variation without the use of an energy degrader, thus eliminating secondary radiation during the in-depth beam scanning, increasing the ion current delivered to the patient and improving the beam quality. The beam energy is determined by the magnetic field strength at the extraction radius, and changing the field enables selection of the final beam energy. The magnetic field can be adjusted while maintaining the needed radial field profile. These concepts and the basic magnetic design are described in Section 6.

Details of the engineering design, including the superconductor and coils, structure, cryostat and weight, are given in Sections 7, 0, 9, and 10, respectively. Conceptual design of the RF acceleration system is given in Section 0 while Section 12 describes the process of energy variation and gives estimates of the ac losses during the magnetic field cycling.

Beam dynamics calculations are given in Section 13. The beam dynamics calculations show that protons can be injected, accelerated up to 230 MeV and extracted stably using the design reported here.

Finally, some concepts for design of a power system capable to provide the large variations in energy and power required for changing the beam energy are summarized in Section 14.

In summary, through the work summarized in this report, MIT, in collaboration with ProNova Solutions, LLC, we have demonstrated the feasibility of an ironless synchrocyclotron for use in the clinical treatment of cancer. Furthermore, the ironless synchrocyclotron approach can be scaled up to accelerate light ions up to carbon, offering significant treatment advantages over conventional proton therapies, and offers a path for more rapid introduction of this technology to clinical uses.

If further funding can be provided in the future, a detailed engineering design can be completed, followed by fabrication of a working prototype system which could then be commissioned and used for PBRT research purposes.

1 The Introduction

Hadron beams have been increasingly used over the past two decades as a method for treatment of cancer tumors. The use of hadron beams for cancer treatment was first proposed in 1946 [1] with clinical trials beginning in 1954 [2]. Although the number of hadron radiotherapy systems is small in comparison with the more conventional use of X-ray systems, their popularity has been increasing because, for several specific types of tumors, and especially for pediatric cancers, they offer significant advantages in dose delivery and in reducing damaging side effects over X-Rays. Historically these treatment systems have used particle accelerators of the synchrotron type or the cyclotron type. The overwhelming majority of these systems accelerate protons for Proton Beam Radio Therapy (PBRT), but there are a few synchrotron systems in Asia and Europe that use heavier carbon ions. The earliest synchrotron and cyclotron systems all used conventional resistive electromagnets. The first superconducting cyclotron used for cancer therapy was a proton cyclotron installed at the Harper Hospital in Detroit in 1990, but instead of directly irradiating a tumor, the proton beam was directed to a target to generate neutrons which were then used to treat the tumor.

The size, cost (capital and operating), and complexity of resistive cyclotron accelerators for ion beam radiotherapy is clearly a significant impediment to reducing the cost of ion beam delivery. The report from the 2013 workshop on Ion Beam Therapy outlined significant R&D that must be done to improve accelerator technology [3]. The report also indicates that presently only slow cycling synchrotrons are used for treatment with ions heavier than protons. Highly compact cyclotrons to accelerate heavier ions up to carbon could have major advantages compared with these gargantuan low-field systems [4]. Additional technical discussion of concepts needed to make ion beam therapy “smaller, lighter, and cheaper” is given in [5] which explores how the application of superconductor technology to cyclotrons can achieve these goals.

The use of superconductivity in a cyclotron design can reduce its mass an order of magnitude, yielding significant reduction in overall cost of the device, the accelerator vault and its infrastructure, as well as operating costs. Despite nearly 40 years of design effort [6]–[9] the basic magnetic configuration for superconducting synchrocyclotrons remains relatively unchanged from that proposed by Lawrence over 80 years ago for resistive-magnet-based cyclotrons [10], [11] The basic configuration still consists of a single, split pair solenoid embedded in a relatively massive iron return yoke, with the radial magnetic field profile in the acceleration zone shaped by the profile machined into the face of the iron pole tips.

At MIT, we have previously developed a design for a proton accelerator that results in a compact device that is small enough and light enough to mount directly on the beam delivery gantry, entirely eliminating the beam delivery system. Alternatively, it can be located outside the treatment room but in a shielded vault much smaller in volume than those required for a conventional resistive cyclotron, since the high field, compact superconducting design is about a third of the size of a conventional cyclotron. The MIT design is based on using a very high field superconducting magnet (9 T at the pole face, Nb_3Sn superconductor) in a synchrocyclotron type of accelerator. Elements of this design have been patented by MIT and are being licensed commercially [12]–[14]. This design, as well as superconducting cyclotrons designed by other companies use warm iron pole pieces for magnetic field shaping in the beam chamber and an iron yoke for flux return yoke and external field shielding. The use of a warm iron yoke requires the transmission of large electromagnetic loads across the cryostat boundary, loads that must be accommodated in the cryogenic design of the magnet vessel, substantially increasing the weight of the magnet system.

The main parameters of several commercial superconducting cyclotrons are compared with a conventional resistive cyclotron in Table 1 Comparison of Main Parameters of Several Commercial Cyclotrons.

Table 1 Comparison of Main Parameters of Several Commercial Cyclotrons

	Mevion S250	IBA S2C2	Varian Proscan	IBA C230
Magnet Type	Superconducting	Superconducting	Superconducting	Copper
R pole (m)	0.34	0.50	0.80	1.05
D Yoke (m)	1.80	2.50	3.10	4.30
Height (m)	1.20	1.50	1.60	2.10
B_o (T)	8.9	5.7	2.4	2.2
B_f (T)	8.2	5.0	3.1	2.9
Mass (mt)	***25***	***50***	***100***	***250***
T_f (MeV)	254	230/250	250	235

All the superconducting cyclotrons have lower mass than the conventional cyclotron and the mass is proportional to the peak magnetic field at the pole tip. Comparing the Mevion S250 operating at high field with the conventional system operating below the magnetic saturation limit of ~2T with iron, shows how the system mass can be reduced by a factor of 10.

In this report we present the conceptual engineering design of an iron-free superconducting synchrocyclotron with active magnetic shielding and variable beam energy, which, we believe will offer several advantages over traditional superconducting magnet technology, and beyond even those we introduced with the high field approach.

2 Iron-Free Superconducting Cyclotron Concept

Previous design studies to address design limitations imposed by reliance on iron-based technology concentrated primarily on isochronous machines. These studies examined the replacement of the iron poles with shaped superconducting coils as a means to enhance the flutter field achievable in a high field device [15], [16]. We recently developed [17] and patented [18] a conceptual design for a compact superconducting synchrocyclotron that demonstrates the possibility to further reduce its weight by almost another order of magnitude by eliminating all iron from the design. In an iron-free design, the heavy iron pole tips are replaced by a much lighter series of concentric field shaping coils that generate the magnetic field profile needed to guide the beam through acceleration and outer ring coils to reduce the field away of the cyclotron by electromagnetic shielding.

Implementation of this proposed iron-free design benefits from several significant advances in superconducting magnet technology pioneered in the magnetic resonance imaging (MRI) industry during the past 20 years, such as active magnetic shielding [19]. An iron-free design has the advantages of low weight, smaller accelerator vault volume, enhanced magnetic shielding, and structural efficiency, since all the large magnetic forces can be reacted within the cold mass, with no need to introduce heavy structural elements to bridge the cold and room temperature parts.

Another major advantage of the iron-free design is that the linear relationship between operating current and field magnitude facilitates the development of a synchrocyclotron providing beam energy variation without the use of an energy degrader, and/or for using a variety of accelerated particles in a single device. This could open up a whole new area for clinical treatment if the same facility can deliver multiple ion species, e.g. from protons through carbon. The radiation oncologist would be able to optimize treatment for each patient using the ion species best suited for their type of cancer.

An example of the difference between a superconducting synchrocyclotron designed with an iron pole and yoke and an ironless design is shown in Fig. 1. The basis for the comparison is a 250 MeV synchrocyclotron operating with a central field of ~9T and the same magnetic field profile in the beam gap.

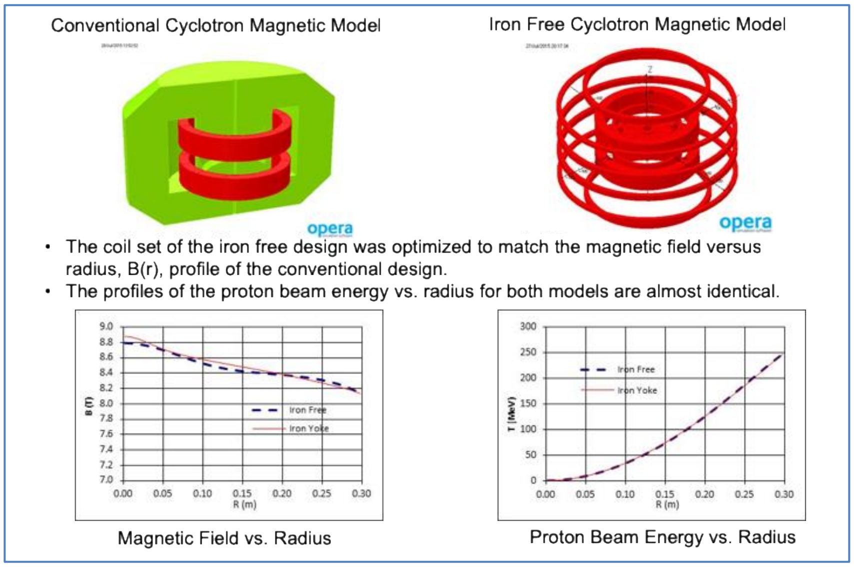

- The coil set of the iron free design was optimized to match the magnetic field versus radius, B(r), profile of the conventional design.
- The profiles of the proton beam energy vs. radius for both models are almost identical.

Fig. 1 Comparison of a high field superconducting synchrocyclotron with an ironless synchrocyclotron. The magnet systems for both designs are optimized to have matching magnetic field profiles and beam energy versus radius in the midplane acceleration region.

The improvement in magnetic shield of the leakage field is shown in Fig. 2. For the iron-free design the 10-G level occurs at a radius less than 2 m, whereas in the conventional design the calculated field at 2 m is 180 G. In the axial direction the field at the same, 2 m, distance from the isocenter is 10 G and 410 G respectively.

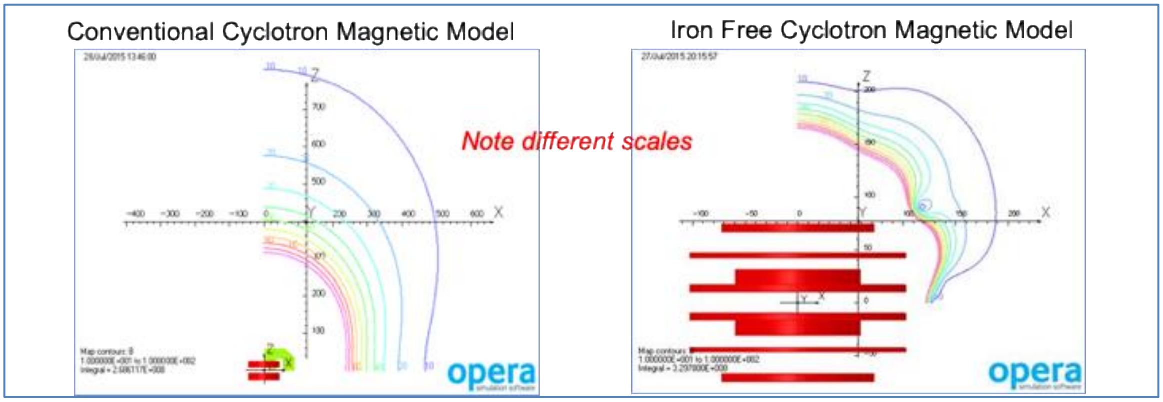

Fig. 2 Active magnetic shielding versus shielding with an iron yoke. The lines indicate fields from 10 G to 100 G with 10-G increments.

A layout of the high field, iron free design of Fig. 1, including the cryostat and structure, is shown in Fig. 3. The main parameters of a 250 MeV synchrocyclotron are shown in Table 2 comparing the main features for superconducting machines shielded by iron or by superconducting shielding coils. It can be seen that when compared on a similar magnetic design and final beam energy basis, the total weight of the device can be reduced from about 22 metric tons to 7 metric tons, although the amount of conductor is increased by a factor of about 2 and the stored energy is increased by a factor of about 3.

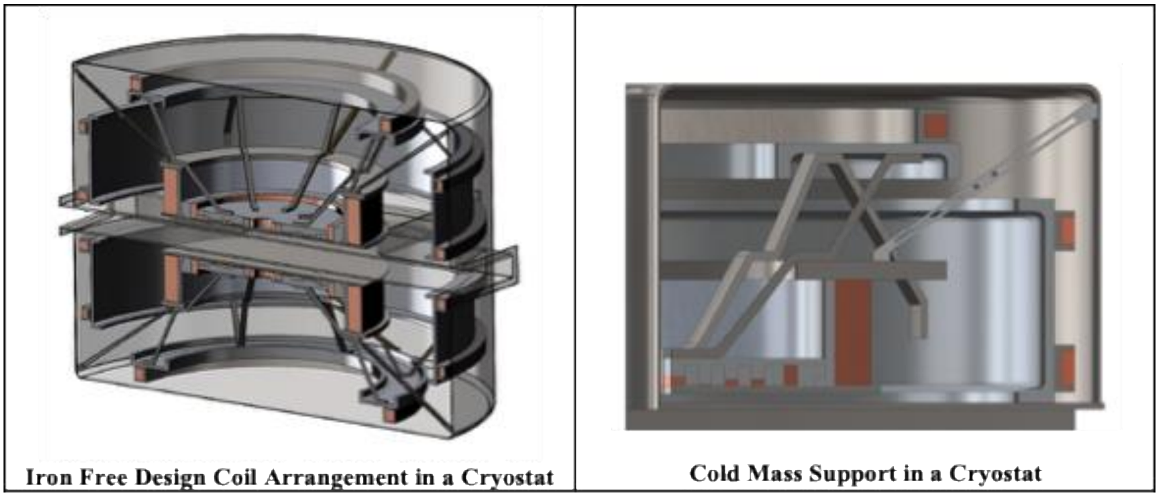

Iron Free Design Coil Arrangement in a Cryostat

Cold Mass Support in a Cryostat

Fig. 3 Layout of an iron-free cyclotron with self-shielding superconducting magnet with cryostat and internal support structure.

Table 2 Comparison of a compact superconducting 250 MeV synchrocyclotron with and without iron

Model		With Iron	Ironless
		Beam	
B_o	T	8.877	8.791
B_{ex}	T	8.132	8.109
R_{ex}	m	0.297	0.296
T_{ex}	MeV	247.2	245.7
		Coil	
E_m	MJ	9.6	32.0
I_{op}	A	2,000	2,000
B_{max}	T	10.98	11.60
OD	m	1.80	2.17
H	m	1.20	1.61
M_{cond}	kg	1,448	2,225
		Field	
R(10G)	m	5.0	1.8
Z(10G)	m	8.2	2.0
Magnet	mt	5,278	6,808
Total (Magnet + Iron)	mt	21,823	6,808

In this report we present design details for the superconducting magnet system of an iron-free synchrocyclotron that could generate a proton beam with final energy of 230 MeV at full operating current, but could also be rapidly swept to deliver a final energy level as low as 70 MeV. The beam energy delivered to the patient is directly related to the depth of the tumor. To sweep out the entire tumor treatment volume, the beam energy must be rapidly varied to affect the depth variation of the radiation dose in the tumor volume. Dose distribution in the transverse direction at each beam energy is performed either by traditional beam scattering and collimation or by the newer methods of transverse (e.g. raster or pencil) beam scanning.

3 230 MeV/u Proton Beam Radiotherapy Requirements

For clinical treatment of patients with Proton Beam Radiotherapy (PBRT) the charged particle beam has certain minimum requirements that must be met:

1. The proton beam shall have an absolute range of 38.0 + 0.5 -0.0 g/cm^2 in water.
2. The proton beam shall have a 1 hr range stability of 0.05 gm/cm^2, and a 1 year absolute range stability of 0.1 g/cm^2
3. A depth of penetration in the patient of 32 g/cm^2
4. A square field of 20 x 20 cm to a depth of 25 g/cm^2
5. A square field of 10 x 10 cm to a depth of 32 g/cm^2
6. Continuous depth modulation over the full range
7. Dose Rate of 200 cGy / minute minimum
8. Field uniformity of +/- 2.0%
9. Dose reproducibility +/- 0.01Gy.

The depth of penetration shall be measured to the 90% distal dose point, (i.e. the point beyond the Bragg peak where the dose falls to 90% of the value at the Bragg Peak maximum). It is expected that the dose will be measured with a parallel plate ionization chamber.

The residual range of a 250 MeV proton beam is approximately 38 g/cm^2 in water. When allowance is made for range absorption in scattering foils to produce a beam of broad lateral extent, a depth of penetration in a patient of 32 g/cm^2 can be expected.

The size of the square field shall be measured at the nominal Source to Axis Distance (SAD), in this case 2 m. The field size measurement is defined as the distance between the 50% dose points through the center of the field. It is expected that this measurement will be made with either film or a small detector such as a diode detector. The square field will be collimated out of a circular field with diameter approximately equal to 1.41 times the square field size.

Modulation depth is defined as the distance between the proximal 90% dose point and the distal 90% dose point. The K-250 system will provide a modulation depth that is continuously adjustable (in 1 mm increments) over the full depth of penetration.

Dose rate into a large field can be used along with the beam energy and irradiation volume to calculate a required beam current.

Field uniformity specifies how much the dose level can vary within the specified treatment field. In a typical conventional radiotherapy system this would just be the variation in lateral dose profile. In the case of proton therapy the field uniformity places a requirement on the lateral and depth uniformity taken together at any point in the 3-dimensional volume.

4 Reference Requirements for the Cyclotron Accelerator

1. Machine Type: Synchrocyclotron.
2. Final Energy: 230 MeV +3.0/-0.0 MeV

   This requirement is derived from the absolute H^+ range requirement.
3. Energy Spread: $|\Delta E/E| \leq 0.25\%$

   This requirement is derived from the H^+ intrinsic range straggling of 1%. A beam energy spread of ±0.25% makes is clinically acceptable with respect to this straggling.
4. 1 year absolute Energy Variation: $|\Delta E/E|_\infty \leq 0.13\%$.

   This requirement is derived from the 1 hr range stability, and represents a range variation of less than 0.5 mm in water.
5. Ion Species: H^+
6. Extraction Efficiency: ≥ 50%
7. External Beam Intensity:
8. Minimum: 5 enA
9. Maximum: 50 enA

   The minimum external beam intensity is derived from the requirement for a 2 Gy standard dose into a field of 20 cm x 20 cm at a penetration of 30 cm during a 1 minute treatment time.

5 Synchrocyclotron Requirements

5.1 Weak Focusing

The superconducting magnet shall provide the magnetic guide field for a proton synchrocyclotron. A synchrocyclotron is a weak focusing cyclotron in which the relativistic mass increase of the protons is compensated by decreasing the acceleration frequency *synchronously*. Weak focusing accelerators are governed by the requirement that the field index

$$n = -\left({}^{rdB}/_{Bdr}\right) \geq 0$$

shall exceed zero (as indicated) over the whole acceleration interval in the radial coordinate r. The field index is usually determined by a combination of fields from superconducting coils and magnetized iron. For this application there will be no iron or other magnetizable material present. This guide field has two important symmetries. There exists a plane, which shall be known as the median plane, on which $B_r = 0$ for all r. There exists an axis, which shall be known as the symmetry axis, for which $B_r = 0$ for all z. The symmetry axis is normal to the median plane. The maximum energy possible in a given synchrocyclotron guide field is determined by the condition:

$$2\sqrt{n} = \sqrt{1-n} \; or \; n = 0.2$$

The full energy radius and the corresponding magnetic field at full energy radius are inversely related in a synchrocyclotron when the final energy is constant. For protons, the relationship between the final energy, final radius and magnetic field at final radius is

$$E = \frac{(erB)^2}{2m_o}$$

A particular field index solution for a 250 MeV proton synchrocyclotron at 5.5 T central field shall be known as the Wu Solution [20]. It is possible to extend the Wu solution to higher central fields, but as the central field is raised the maximum radius decreases in proportion according to the above relations.

This magnet for a 230 MeV proton synchrocyclotron shall be defined by scaling the Wu Solution for the field index to the magnetic field at the extraction radius at the given extraction energy. This is specified as the normalized values of B/B(0) vs. r/r(230 MeV) +/- 2% listed below in Table 3 below.

Table 3 Wu solution to normalized R, B

$r/r_{extraction}$	$B_z/(B_z @ r_{extraction})$
0	1.088059
0.026247	1.087152
0.052493	1.084597
0.07874	1.081327
0.104987	1.077747
0.131234	1.074205
0.15748	1.070762
0.183727	1.06757
0.209974	1.064584
0.23622	1.061837
0.262467	1.059283
0.288714	1.056921
0.314961	1.054725
0.341207	1.052657
0.367454	1.050722
0.393701	1.048879
0.419948	1.047124
0.446194	1.045421
0.472441	1.043763
0.498688	1.042115
0.524934	1.040467
0.551181	1.038781
0.577428	1.037049
0.603675	1.035242
0.629921	1.03331
0.656168	1.031307
0.682415	1.029161
0.708661	1.026938
0.734908	1.024645
0.761155	1.022356
0.787402	1.020115
0.813648	1.017942
0.839895	1.015775
0.866142	1.013561
0.892388	1.011251
0.918635	1.008927
0.944882	1.006569
0.971129	1.004084
0.997375	1.000735
1	1

5.2 Magnet

1. Magnet type: superconducting, comprised of the following coil sets:
    a. Main Field Coils, split pair (upper and lower)
    b. Gap Field Profile Coils, split pairs (uppers and lowers)
    c. External Field Magnetic Shielding Coils, multiple with symmetric split pairs
2. Orientation: Fixed with synchrocyclotron symmetry axis parallel to floor.
3. Return Yoke and Pole: None
4. Conductor-Cable-In-Conduit-Conductor (CICC)

5.3 Ion Source

Ion Source Type: gaseous feed, cold cathode, pulsed arc discharge.

Extracted current: Either pulsed or constant as the magnetic field is being varied; extracted ion composition: H^+ and potentially H_2^+ (H_2^+ may impact space charge, and thus extracted total current, at the extraction region.

Ion Source Hours per annual quarter: 57 hr

Basis: 4 patients/hr×1fr./patient. ×1min./fr. ×1hr/60 min ×12hr/dy ×5.5dy/wk×13wk/quarter

Electrode Lifetime: MTBF ≥ 100 hr

Basis: Pulsed operation, quarterly maintenance and 2x safety factor.

Electrode Material: HfC

Gas Flow: ≤ 0.1 SCCM

Initial Beam Phase Requirement: Pulse Rise to RF start time is adjustable

5.4 Acceleration

5.4.1 RF System:

Acceleration gaps per turn: 2- Single 180° dee and 180° dummy dee Design Peak Electric Field: ≤75 kV/cm

dee angle initial- 160˚ dee angle final - 160˚

dee – dummy dee Minimum Gap: 6 cm

dee – Liner Vertical Minimum Gap: 10 cm

dee – Liner Radial Minimum Gap: TBD

Starting Frequency (f_0): 75 MHz (determined by highest beam energy for initial beam acceleration)

Final Frequency (f_{ext}): 34 MHz (determined by lowest energy at final beam acceleration)

Resonator Type: ¾ wavelength structure with mechanical rotating condenser

RF drive: Programmable waveform generator, broadband amplifier, phase locked to rotating condenser drive

Rotating Condenser Frequency: 3600 RPM Rotating Condenser Sectors: 16

Rotating Condenser Initial Value: 10 pF

Rotating Condenser Value at Extraction: 58 pF

5.4.2 Central Region:

Ion Source Maximum chimney diameter: 4 mm

Gap 1 Spacing: 1 mm

Gap 1 Magnetic Field: 5. 0 T

5.4.3 Acceleration:

Bunch Design Phase Error: -30°

dee Voltage (V_0): 10 kV

Synchronous Phase Energy gain per revolution: 34.6 keV

Average Energy gain per turn: 20 keV (50% margin)

Number of Revolutions (n): 12,500

Single Bunch Full Acceleration Time (n/f): 102 μs

Proton γ at 230 MeV: γ=1.267

5.5 Beam Structure

5.5.1 Micro Structure

Initial RF period (75 MHz): 13.3 ns

Maximum Initial Bunch Capture Phase Width($\Delta\varphi_b$): ≤ 20°

Maximum Initial Bunch Time Width (Δt_b): 0.39 ns

Number of Capture Bunches per acceleration cycle: 10

Req. Captured Protons per Bunch (N_b): $6.25\ 10^6$ protons

Protons per acceleration cycle (N_A): $6.25\ 10^7$ protons

5.5.2 Macro Structure

Repetition rate: 1000 Hz

Macro Duty Factor: 10% (1000×0.102ms/s)

Nominal Design Current: 6.25 10^{10} protons/s

(10x Design Current: 6.25 10^{11} protons/s)

Intensity Control: individual macro pulse rejection (1/1000)

Beam Stop: central region bias stop in one acceleration cycle

5.6 External Beam Matching

1. Extraction Efficiency: ≥ 50%, as measured from the internal H^+ beam current at full energy radius to external H^+ beam current on first scattering element.
2. Horizontal Emittance at match point: TBD
3. Vertical Emittance at Match point: TBD
4. Radiation Requirements due to Non-extracted Beam

An extraction efficiency of 50% means that the cyclotron will experience a radiation dose from the lost beam. The lost beam will have an energy close to the design energy of 230 MeV, so we assume explicitly that the lost beam is at full energy. The lost beam will concentrate in the azimuthal vicinity of and in the extraction channel. The lost beam at full energy will result in spallation neutron production with a broad distribution. We assume at the volumetric solid mass of the cyclotron receives a volumetric percentage of the total neutrons flux. The average and maximum design extracted currents [Section 3.] will determine average and peak instantaneous, daily, weekly, yearly, and lifetime neutron doses.

5.7 Vacuum System

1. Configuration: beam chamber and cryostat shall maintain separate vacuums against atmospheric pressure.
2. Operating Beam Chamber Pressure: $\leq 1.0 \cdot 10^{-6}$ T
3. Beam Chamber Pumping Speed: $\leq 500\ \ell s^{-1}$
4. Beam Chamber Pumping System: turbomolecular pump with external roughing pump
5. Cryostat: no direct pumping; roughing via inter-stage of beam chamber turbo pump
6. Cryostat Helium Leak Requirement: no detectable signal, 1 hr accumulation test at sensitivity level of $1.0 \cdot 10^{-9}\ \mathrm{T}\ell s^{-1}$

5.8 Cryogenics

1. Cryogenic states: warm, cool down, stand by, cold, and warm up
2. Operating Temperature: 4.5 K
3. Standby Temperature: ≤ 20 K
4. Steady State Heat Load:
    - @ 4.5 K: TBD
    - @ 65 K: TBD
    - Current leads: TBD, HTS Leads
5. Cryogen Supply: none; Cooled by cryocoolers
6. Cool Down Rate:
    - Warm to stand by: TBD Standby to cold: TBD
7. LN2 reservoir: none
8. LHe reservoir: none

6 Basic Magnetic Design

The Variable Beam Energy cyclotron operates in an AC mode associated with a given variation of the operating current in its superconducting magnet. The design of the magnet to a large extent is defined by the ultimate parameters specified at the “Basic Design Point" corresponding to the maximum beam energy, i.e. for 230 MeV protons. This design will be referred to as the “Basic Magnetic Design”.

A Variable Beam Energy synchrocyclotron operates in an AC mode by adjusting the operating current in its superconducting magnet to produce a desired extracted beam energy. (note: although isochronous cyclotrons have been more commonly used for this application, it is easier to implement the iron free design in a synchrocyclotron. The differences between these two types of cyclotron as they relate to variable energy designs are discussed in [17], [21]. The design of the cyclotron magnet is determined by ultimate parameters corresponding to the maximum beam energy delivered from the cyclotron, i.e. for 230 MeV protons. The corresponding magnet design is referred to as the “Basic Magnetic Design.” The basic magnetic design reported here is based on a magnetic model designated internally at the PSFC as PN230-ab7am [22].

The major characteristics of the magnet for a variable-energy, 230 MeV cyclotron are summarized in Table 4. Most of the geometric parameters, radius, *R,* vertical position, *Z*, are self-explanatory. It is important to note that the parameters shown in Table 4 are different for this ironless design than those shown in Table 2, because the peak field was reduced on purpose to lower the peak magnetic field at the coil windings to allow us to design this machine with NbTi superconductor. The higher field designs require use of Nb_3Sn which is a more expensive type of superconductor and also more difficult to fabricate into a coil because of its very brittle nature and requirements for reaction heat treatment at temperatures above ~650C. This choice results in a cyclotron with somewhat increased radius and mass.

Table 4 Magnet Design

Beam	
Maximum central magnetic field (at R=0, Z=0)	4.980 T
Maximum magnetic field at extraction (at R=R_{ex}, Z=0)	4.596 T
Extraction radius, R_{ex}	0.501 m
Maximum beam energy, $T(R_{ex})$	226.3 MeV/u
Coil	
Stored magnetic energy, E	31.1 MJ
Outer diameter of cryostat, *OD*	3.00 m
Overall height of cryostat, *OH*	2.02 m
Magnitude of fringe magnetic field	
In radial direction, B(at R=3.5m, Z=0)	11 Gauss
In axial direction, B(at R=0, Z=4.5m)	12 Gauss

Fig. 4 depicts the coil build, Fig. 5 the field on the surface of the conductor, and Fig. 6 the stray fields in the vicinity of the magnet.

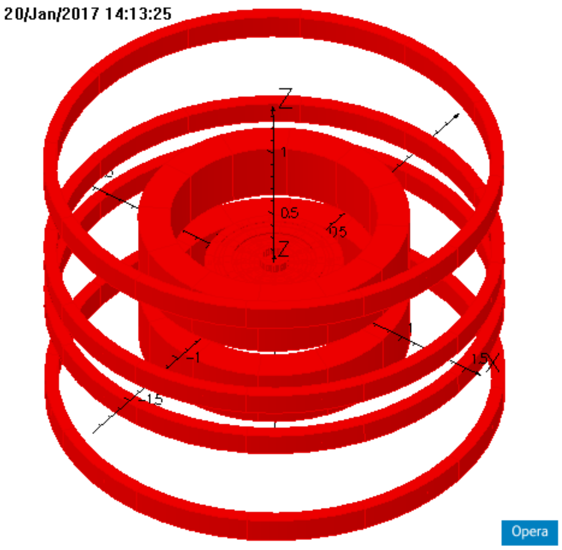

Fig. 4 Coil Build PN230-ab7am.

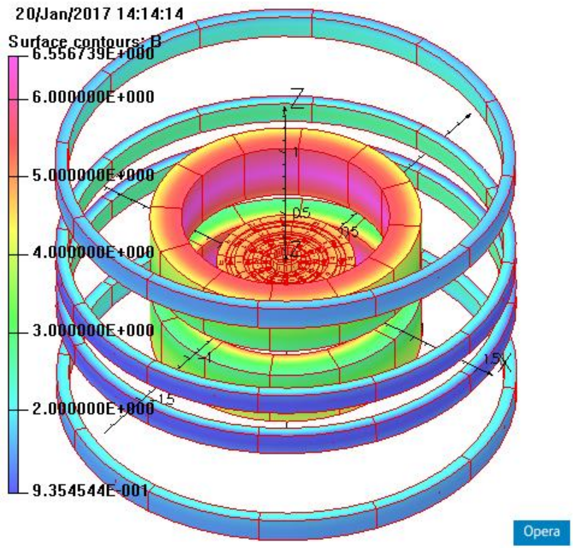

Fig. 5 B-field on the Surface of the Conductor.

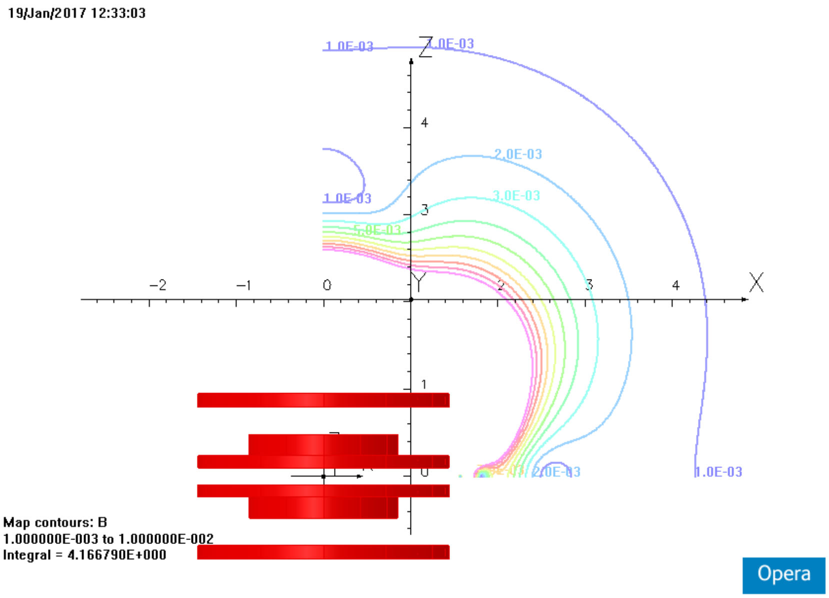

Fig. 6 Stray Fields in the Axial Cross-section. (10 Gauss to 100 Gauss with 10-Gauss increments).

The major parameters characterizing performance of the cyclotron at 230 MeV are shown in Fig. 7-Fig. 11. The tune diagram is shown in Fig. 12. Note that νz (νr) crosses only one, secondary, resonance line, 3νz=1. Extraction happens in the vicinity of the major resonance, νr = 2νz.

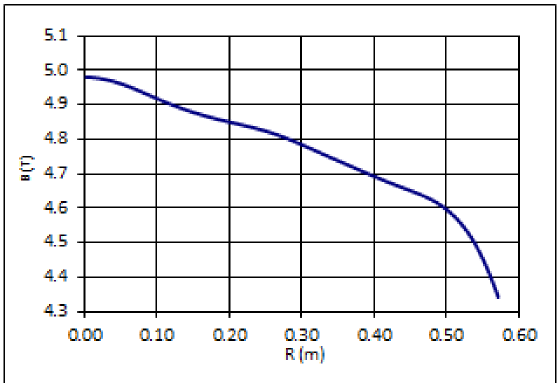

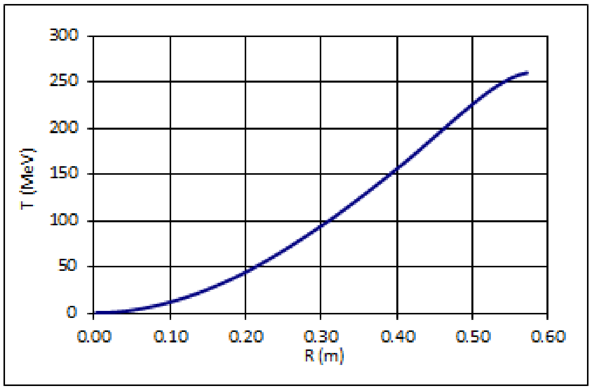

Fig. 7 Field Profile, B vs. Radius.

Fig. 8 Beam Energy vs. Radius.

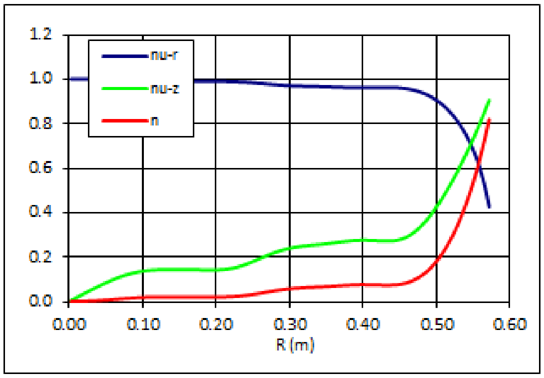

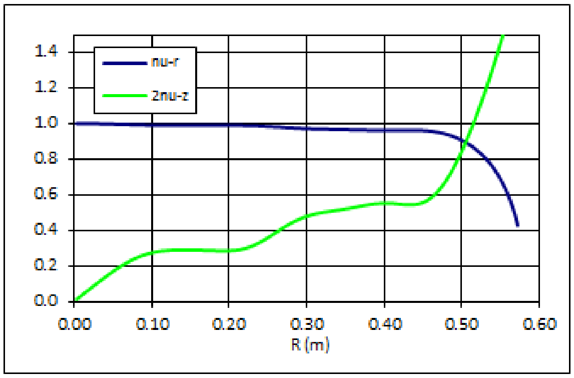

Fig. 9 Betatron Frequencies and Index vs. Radius.

Fig. 10 ν_r and $2\nu_z$ Intersect at R_{ex} =0.5 m.

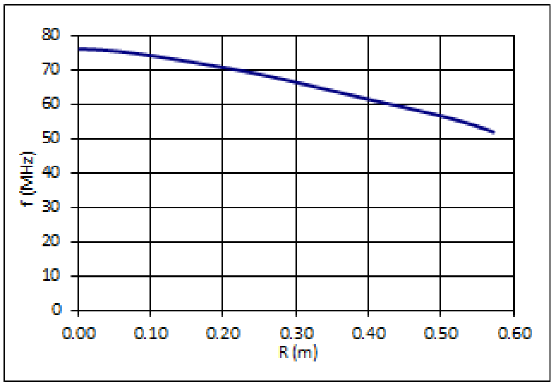

Fig. 11 Acceleration Frequency vs. Radius.

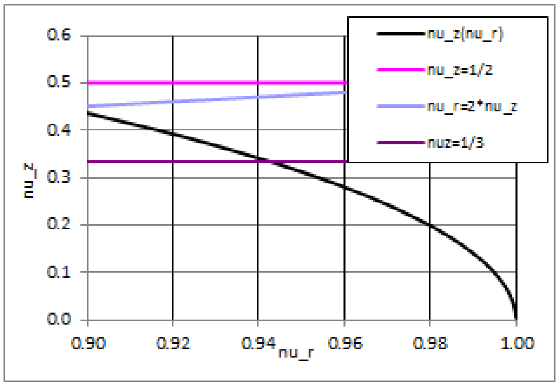

Fig. 12 Tune Diagram.

Table 5 and Table 6 show parameters of the solenoidal windings of the upper half of the magnet: coordinates, (R1,Z1) and (R3,Z3), of the inner-lower and upper-outer corners of the envelope of the solenoids, reference name of the conductor, average current density over the winding, J_{wp}, operating current, I_{op}, dimensions of the insulated conductor, H and W, numbers of turns in radial and axial directions, Nr and N_z, total number of turns, N_{tot}, total ampere turns, NI, peak fields[2], B_{max}, axial force, F_z, coil volumes, average coil densities calculated using per turn fractions of the SS conduit, superconductor and epoxy impregnated insulation based on the cable design in the next section, dens, and weights, M. The total weight of the conductor, M_{cond}, is calculated for ALL coils of both upper and lower parts of the magnet. Breakup of the turn numbers presumes that the solenoids will be layer wound, so to simplify layer to layer transitions the number of the layers is adjusted to even numbers[3].

---

[2] B_{max} and F_z are calculated using the program SOLDESIGN. Positive F_z is away from the mid-plane.

[3] Half-filled transitions at the top/bottom of the coils were not modeled in this approximation.

Table 5 Coil Design

Coil	*R1*	*Z1*	*R3*	*Z3*	*Cond*	J_{wp}	I_{op}	*H=W*	N_r	N_z	N_{tot}
	m	m	m	m		A/mm^2	A	mm			
1	0.65120	0.10000	0.84880	0.48000	NbTi-a	52	3000	7.60	26	50	1300
2	0.07407	0.10000	0.09747	0.16240	NbTi-b	33	500	3.90	6	16	96
3	0.09997	0.10000	0.15457	0.10390	NbTi-b	33	500	3.90	14	1	14
4	0.15530	0.10000	0.20990	0.11170	NbTi-b	33	500	3.90	14	3	42
5	0.21063	0.10000	0.26523	0.10390	NbTi-b	33	500	3.90	14	1	14
6	0.26597	0.10000	0.32057	0.12340	NbTi-b	33	500	3.90	14	6	84
7	0.32130	0.10000	0.37590	0.10780	NbTi-b	33	500	3.90	14	2	28
8	0.37663	0.10000	0.43123	0.11950	NbTi-b	33	500	3.90	14	5	70
9	1.36200	0.79264	1.43800	0.95224	NbTi-a	52	3000	7.60	10	21	210
10	1.36200	0.09370	1.43800	0.23810	NbTi-a	52	3000	7.60	10	19	190

Table 6 Coil Design

Coil #	*NI*	B_{max}	F_z	*V*	*dens*	*M*
	MA-t	T	MN	m^3	kg/m^3	kg
1	3.90E+00	6.56	-17.52	0.3538	6081	2,152
2	4.82E-02	5.36	0.00	0.0008	5503	4
3	7.03E-03	4.96	0.00	0.0002	5503	1
4	2.11E-02	5.00	0.00	0.0007	5503	4
5	7.03E-03	5.04	0.00	0.0003	5503	2
6	4.22E-02	5.13	-0.02	0.0024	5503	13
7	1.41E-02	4.88	0.00	0.0009	5503	5
8	3.51E-02	4.96	-0.01	0.0027	5503	15
9	6.31E-01	2.32	1.13	0.1067	6081	649
10	5.71E-01	2.79	-0.54	0.0965	6081	587
Total M_{cond}						6,863

7 Circuits and Cable Design

The current baseline design used NbTi Cable in Conduit Conductor (CICC) shown schematically in Fig. 13.

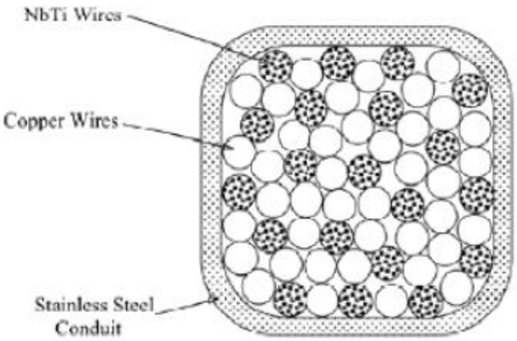

Fig. 13 Schematic of a Cable in Conduit Conductor.

The magnet is comprised of two circuits. Circuit A includes the Main (#1) and Shielding (#9, #10) coils connected in series and carrying transport current, I_{op} = 3 kA. Circuit B is formed by the Field Shaping (#2 - #8) coils with I_{op} = 0.5 kA. At the working point total energy in the system is E_{em} = 31.07 MJ, energy stored in magnets of circuits A and B when the other circuit is off is E_A = 30.7 MJ and E_B = 14.5 kJ. This corresponds to the following inductances, L_A = 6.62 H, L_B = 0.12 H, M_{AB} = 0.24 H. Energy stored in circuits A and B when all coils are energized is 30.9 MJ and 194 kJ respectively. This accounts for the coupled energy split equally between circuits A and B.

Coils of circuit A and B are made of NbTi CICC conductors, NbTi-a and NbTi-b respectively. They were sized using CICCTool Excel program presented in Appendix A. General characteristics of these conductors are shown in Table 7. Here T_{op}, B_{op} and I_{op} are operating temperature, maximum field and conductor current, W_c and H_c are width and height of the conductor without insulation, T_{wall} is thickness of the conduit wall, T_{ins} – thickness of insulation; A_{env}, A_{ss}, A_{ins}, A_{he} and A_{comp} are cross-sectional areas of the insulated conductor envelope, of SS sheath, insulation, helium-filled void and composite strands; J_c, J_{op} and J_{wp} are critical, operating and smeared current density; f_c is fraction of critical, T_c, T_{cs} and dT are critical and current sharing temperature and temperature margin. The last group of rows indicates the quench protection characteristics. The dump resistor, R_{dump}, is sized so that at the end of the dump the whole energy trapped in Circuit A the temperature of the hot spot, T_{hot}, is 150 K and that the time constant of discharge, t_{dump}, in Circuit B is the same as in Circuit A; V_{dump} is the maximum dump voltage at the start of the discharge through the dump resistor.

Table 7 NbTi CICC Design

Circuit		*A*	*B*
Conductor		NbTi-a	NbTi-b
Top	K	4.5	4.5
Bop	T	6.56	5.36
I_{op}	A	3000	500
W_c	mm	7.20	3.50
H_c	mm	7.20	3.50
T_{wal}l	mm	0.70	0.30
T_{ins}	mm	0.20	0.20
A_{env}	mm^2	57.76	15.21
A_{ss}	mm^2	17.66	3.66
A_{in}S	mm^2	6.47	3.17
A_{he}	mm^2	10.70	2.64
A_{cu}	mm^2	20.03	4.64
Asc	mm^2	2.91	1.09
A_{comp}	mm^2	15.29	5.73
Cu/SC		6.89	4.26
f_{he}		31.80%	31.54%
J_c	A/ mm^2	2120	2421
J_{op}	A/ mm^2	1033	459
J_{wp}	A/ mm^2	52	33
f_c		0.49	0.19
T_c	K	6.62	7.16
T_{cs}	K	5.59	6.66
$dT=T_{cs}-T_{op}$	K	1.09	2.16
Quench Protection			
E_{em}	MJ	31.10	0.20
R_{dump}	ohm	0.56	0.13
t_{dump}	sec	12.44	12.46
V_{dump}	V	1,666	64
T_{hot}	K	150	81

It is presumed that the void inside the conduit is filled by helium so that at the operating temperature it is in the supercritical phase. Here and below, the parameters of the NbTi composite strand are defined in correspondence with the specification for the Furukawa low AC loss Type C wire [23]. More details are in Appendix A.

8 Structural Assessment

Structural assessment of the present design was performed using an axisymmetric Opera model shown in Fig. 14. The model uses 1/36th rotational symmetry with a reflective symmetry about the mid-plane. The windings are modeled by isotropic[4] elastic media with the equivalent elastic module scaled from that of the SS conduit by a stress factor, $f_e = A_{env} / A_{SS}$. Respective stress factors for A- and B-type conductors are $f_{eA} = 3.27$ and $f_{eB} = 4.16$. The as modeled isotropic elastic moduli of the A- and B-type windings are those in the hoop direction, 205 GPa/f_e, equal to 48 GPa and 61 GPa respectively. This neglects the carrying capacity of the impregnated insulation and the strands of the cable. The coils are supported by the cold mass (CM) structure made of Al-6061-T6, except for the SS 316 structural base plate supporting the Main and the Field Shaping coils. In the model elastic modulus and Poisson coefficient of SS (Al) is 205 GPa (81 GPa) and 0.25 (0.33). There are no slip planes between the Winding and the CM structure. Field Shaping coils are surrounded by the structure; the Main coil is stuck to the SS base plate and free both at the ID and OD; the Shielding coils are supported by a 2-cm thick channel at top, bottom, and OD surfaces.

Stresses in the SS components of the Winding and the cold mass structure are conservatively compared with the monotonic allowable for welded materials by ASME code, $S_m = \min[1/3S_{uts}, 2/3S_y]$. For 316 SS at 4K $S_{uts} = 1759$ MPa, Sy = 862 MPa and Sm = 575 MPa. For Al-6061-T6 at 4K $S_{uts} = 496$ MPa, $S_y = 362$ MPa and $S_m = 165$ MPa.

Fig. 15 and Fig. 16 show that Von Mises stresses in the CM structure are below 120 MPa and 62 MPa in SS and Al respectively. Note that an attempt to model the base plate made of aluminum returned unacceptably high, 180 MPa, Von Mises stresses in the aluminum base plate.

Fig. 17 - Fig. 20 show Von Mises, Hoop, Axial and Radial stresses in the Winding. All stresses are below 62 MPa.

Note the non-uniformity of axial stresses near the base of the Main coil where they fluctuate and even change sign. This non-uniformity can be mitigated by adding a slip plane between the bottom of the Main coil and the SS base plane. Analyses (both by Opera and SOLDESIGN) show that the integrated axial pressure at this interface (i.e. the axial force on the Main coil) is 17.5 MN. This corresponds to an average normal pressure of 19 MPa. For a coil made of He cooled CICC this pressure shall be acceptable.

Fig. 21 shows that the maximum hoop strain in the winding is 0.098 % which is well within an acceptable range for strain in the superconductor and winding pack

---

[4] Analyses performed for other projects indicate that effect of the anisotropy due to lower equivalent radial and axial elastic modulus is usually insignificant.

Hoop stresses in the SS Conduit can be derived from these results in several ways. One way is by multiplying hoop strain by the elastic modulus of the SS. Respective hoop stresses are shown in Fig. 23. Another way of calculating hoop stresses in the Conduit is by reverse scaling hoop stresses in the Winding by multiplying them by stress factor, f_e[5]. Fig. 24 shows these stresses in the same range as in Fig. 23. They are very close, except for the vicinity of the base of the Main coil due to the same reasons as discussed above.

According to Fig. 22, axial displacements of the energized winding are less than 1 mm. This is due to the as-modeled design of the CM structure. It uses azimuthally continuous conical shells connecting coils and the CM structure between themselves. These shells can be segmented by introducing cuts to reduce eddy currents during ramping. Another possible design option is shown in Fig. 25.

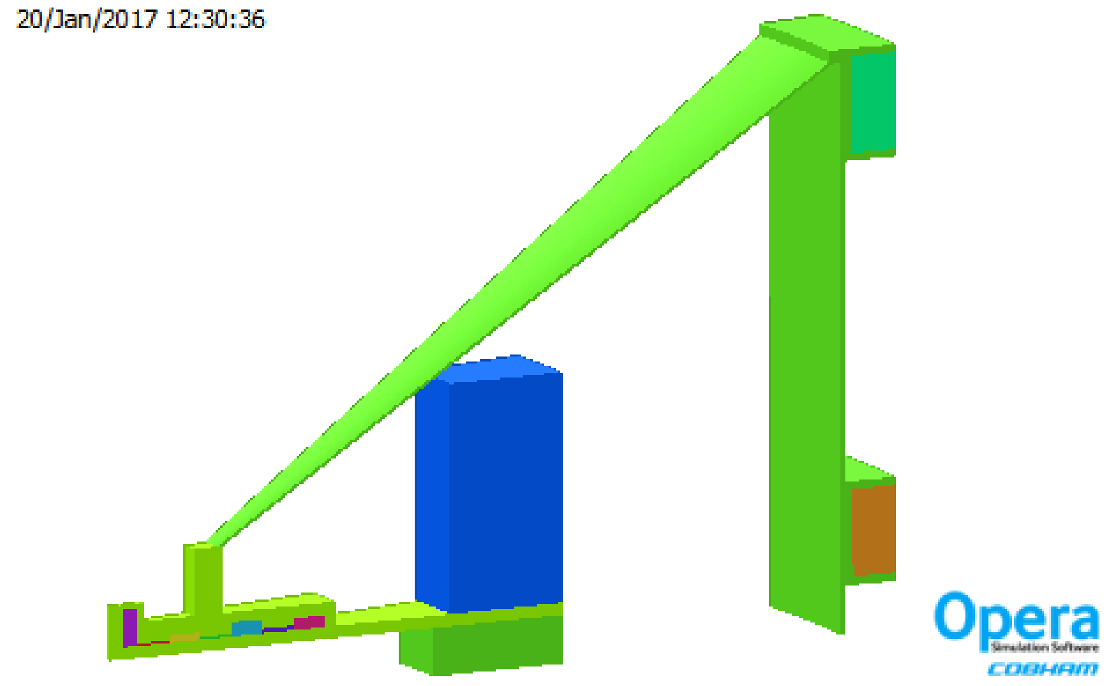

Fig. 14 Axisymmetric structural model.

---

[5] Here the same stress factor, fe = 3.6, was used for all coils.

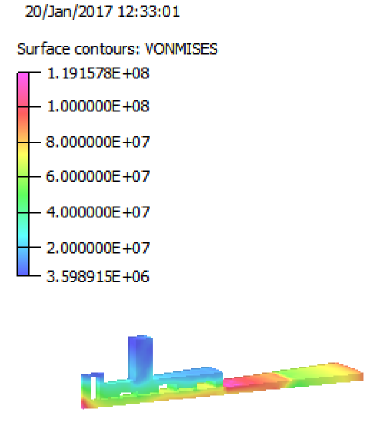

Fig. 15 Von Mises Stress in SS CM Structure

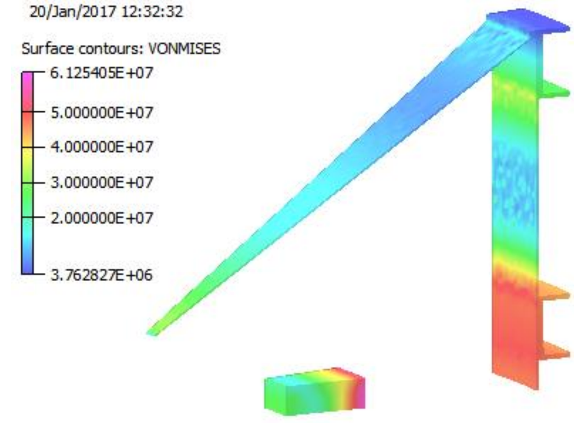

Fig. 16 Von Mises Stress in Al CM Structure

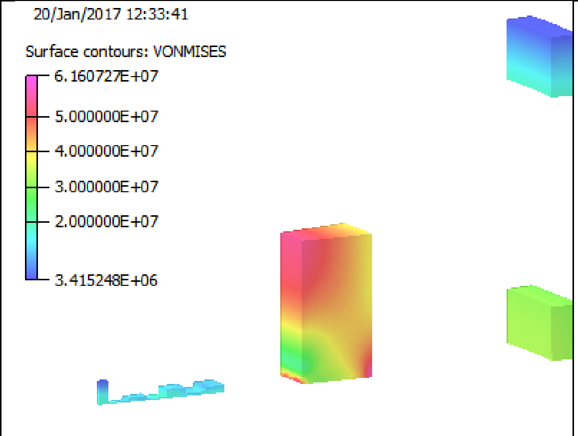

Fig. 17 Von Mises Stress in the Winding

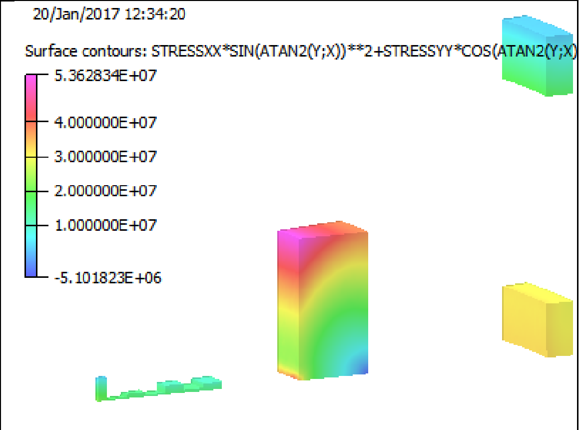

Fig. 18 Hoop Stress in the Winding

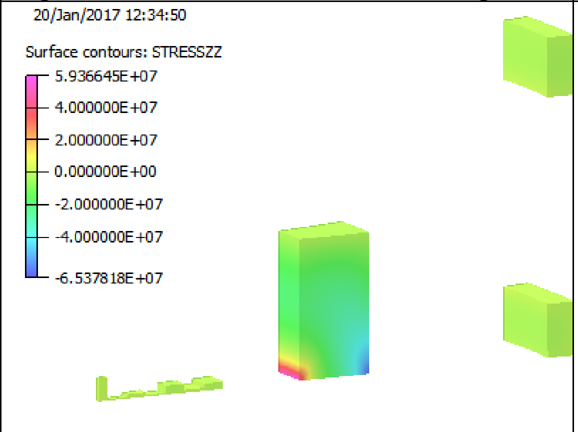

Fig. 19 Axial Stress in the Winding

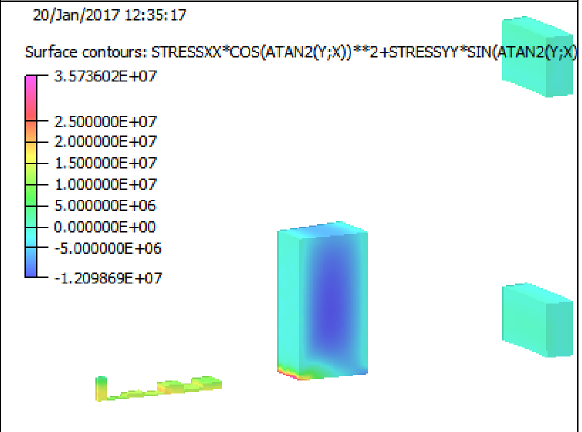

Fig. 20 Radial Stress in the Winding

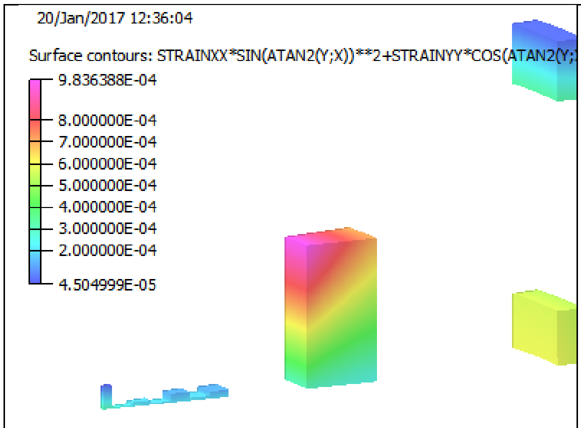

Fig. 21 Hoop Strain in the Winding

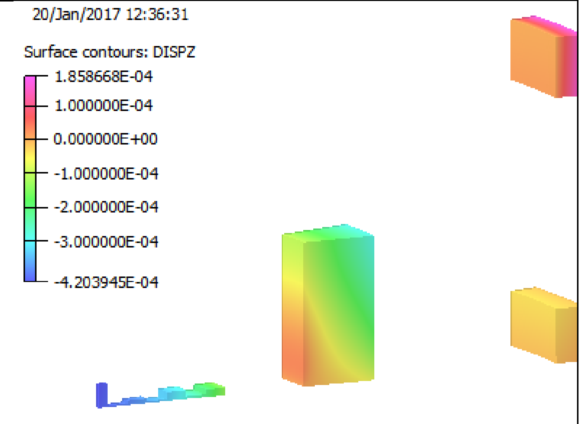

Fig. 22 Axial Displacements of the Winding

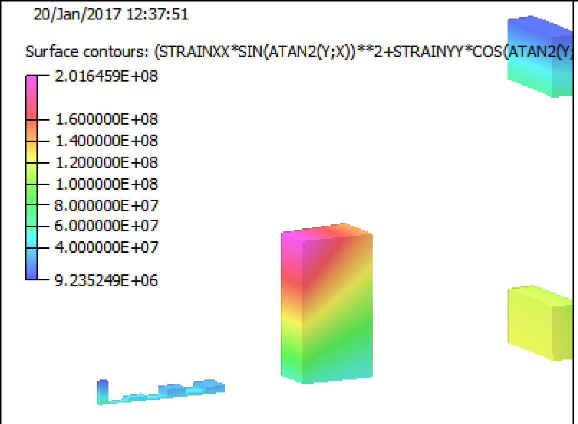

Fig. 23 Hoop Stress in SS Conduit by Hoop Strains

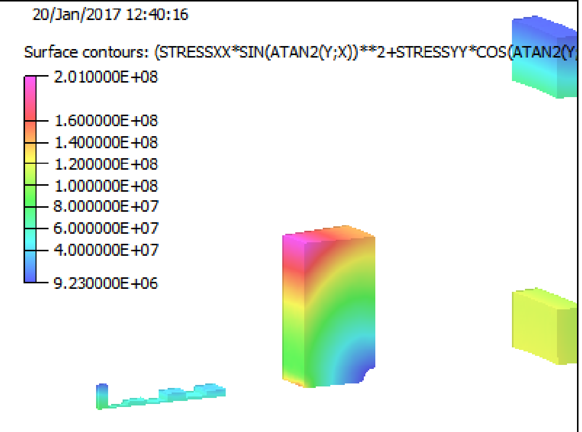

Fig. 24 Hoop Stress in SS Conduit by Hoop Stress in the Winding

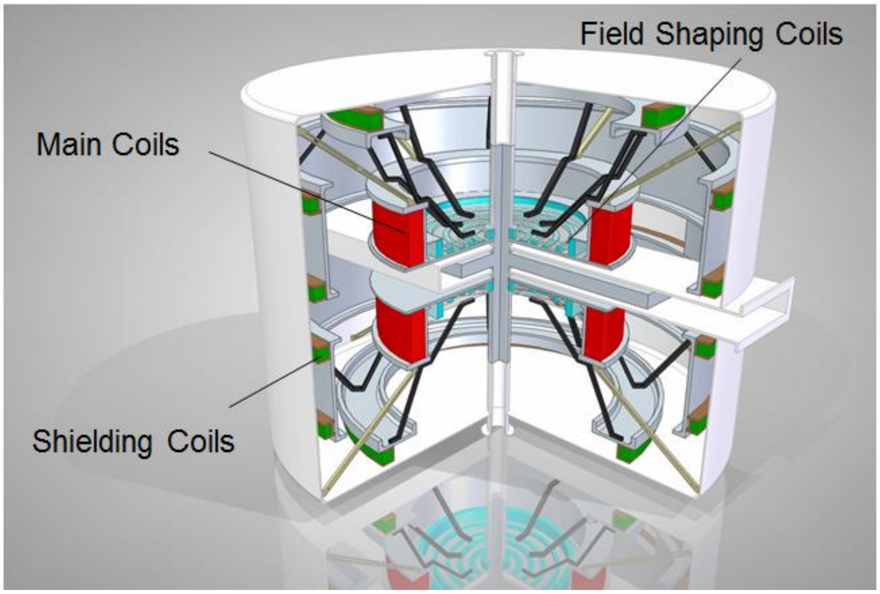

Fig. 25 Optional Design (Schematic)

9 Cryostat Design

The selection of NbTi superconductor for the main and field shaping magnets vastly reduces the active power needed to operate the cyclotron. At the same time, the use of superconducting coils introduces the need to create and sustain an approximately 4K operating environment. The housing used to create the required operating environment is called a cryostat.

The magnet cryostat must be optimized with respected to several major constraints, including:

1. Structural forces, including
   a. Vacuum loads on the cryostat walls
   b. Electromagnetic loads between coil elements
   c. Gravity load on the magnet cold mass, and
   d. Shipping forces during transport and siting

2. Thermal heat loads, including
   a. Conduction along and power generation in the current leads
   b. Thermal radiation from the outer room temperature boundaries, and
   c. Thermal conduction along structural and gravity supports

3. Electromagnetic design
   a. To the extent possible, coils should be "close" to beam path to limit field peaking and permit maximal flexibility in field shaping
   b. Constrained by:
      i. Thickness of vacuum boundary
      ii. Thickness of thermal radiation shielding
      iii. Required assembly / thermal contraction gaps.

A schematic cross-section of the reference design cryostat for the iron-free cyclotron is shown in Fig. 26. The cross-hatched elements show the relative placements for the main, field-shaping, and field shielding coil sets. The blue shaded elements show the coil formers and inter-coil structure. The orange shaded elements show the placement of the thermal radiation shields. The dark green shaded elements represent large bore, G-10 support cylinders that position the coil sets with respect to the grey-shaded, room temperature, cryostat walls, which also serve as the cryostat vacuum boundary. In this design, the harmonic extraction coils are thermally connected to, and indirectly cooled by the main coils. The upper field-shaping coils are enclosed in a separate small cryostat that can be removed to provide access to the cyclotron beam chamber. The following sections describe the main constraints on the cryostat design and how these constraints influence the overall cryostat design.

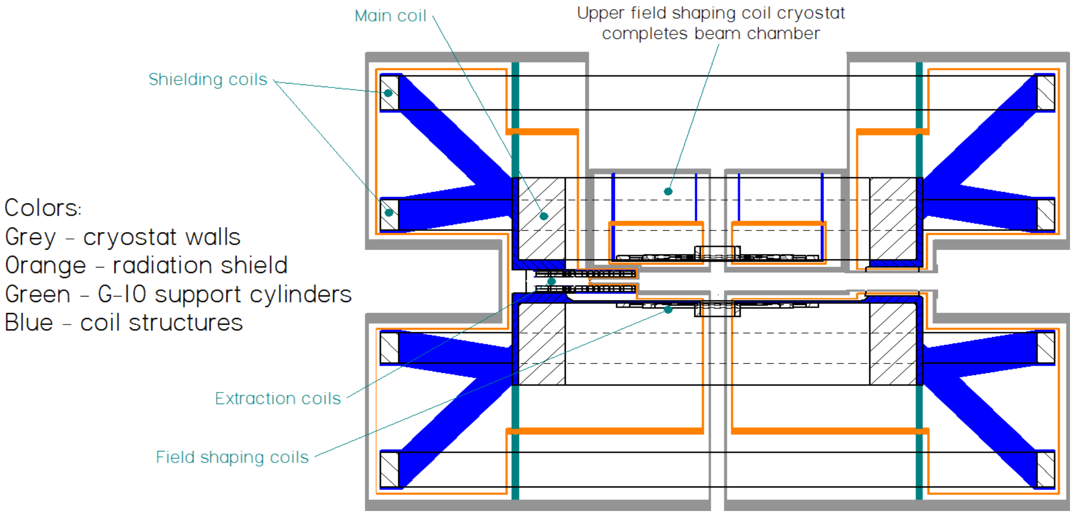

Fig. 26 Schematic cross-section of the reference cryostat design

9.1 Vacuum Loads

To minimize the gas conduction heat load on the superconducting coils, the cryostat must be leak tight and capable of sustaining a moderate to high vacuum environment with internal vacuum pressure typically below 10^{-5} Torr. The internal cryostat vacuum is the first and primary means of insulation for the coil.

First, consider the cryostat faces at the mid-plane/beam chamber region. The ion beam is extracted at a radius of 0.501 m. This requires a slightly larger diameter beam chamber. Allowing 10 cm per side clearance for auxiliary equipment yields minimum 1.02 m diameter for the beam chamber. The atmospheric pressure load on this minimum diameter is ~85 kN (8.5 ton). We must design for this load since the beam chamber and the main cryostat will have separate vacuums and there will be times when the cryostat is evacuated but the beam chamber is at ambient pressure.

Moving to the outer cylindrical cryostat vacuum vessel we must allow space for the Shielding Coils. The diameter to the outer surface of the Shielding Coils is 2.88 m. Allowing 5 cm per side (radiation shield plus clearances) to the vacuum wall yields a minimum diameter of 2.98 m. The resulting atmospheric pressure load on this minimum diameter is ~700 kN (70 ton).

- The maximum stress, σ_{max}, and maximum deflection, δ_{max}, for a flat, circular plate with simply supported edges of radius, R, thickness, t, and elastic modulus, E, subject to uniform pressure, w, are given by:

$$\sigma_{max} = 1.24 \frac{w\,R^2}{t^2} \qquad (1)$$

$$\delta_{max} = 0.696 \frac{w\,R^4}{E\,t^3} \qquad (2)$$

Note: The delta equation coefficient uses psi and inch units of measure

- Using a design stress limit of 2/3 yield (140 MPa for stainless steel) and external 0.1 MPa pressure, the respective thicknesses of the beam chamber and shielding coil flanges should be approximately 15 mm and 44 mm, with corresponding central deflections of 6.7 mm and 19.7 mm, respectively.
- The Beam Chamber deflection can be reduced to below 3 mm by increasing the wall thickness to 20 mm.
- Thickness and deflection of the Shielding Coil flange can be reduced using dished heads, or segmenting the vacuum flange into annular pieces, or using internal compression/coil support structure.
- The beam chamber flange will flatten when the beam chamber is evacuated.

9.2 Electromagnetic Loads

We note that the cryostat outer vacuum walls will be made from non-magnetic material, typically a non-magnetic stainless steel, like AISI 304 or AISI 316. Stainless steel is selected for several reasons. It has high elastic modulus, high yield strain, and following electro-polishing, it provides a very low outgassing surface, essential for preserving cryostat vacuum.

A special advantage of the ironless magnet design is that there is no warm iron yoke requiring a strong electromagnetic force support method to transfer loads from the cold mass to the warm iron through the cryostat walls. This means all the main electromagnetic loads can be supported by an internal cold structure directly between the three principal coil sets. This greatly simplifies the cryostat design (and cost) because it must only support vacuum and gravity loads.

There is a 17.5 MN (1750 ton) force on the main coils towards the cyclotron mid-plane. It is principally supported by a thick stainless steel cylindrical pieces between main coil pairs. Cut-outs in the support cylinder to accommodate the beam chamber must be minimized in order to minimize deflections and field errors.

A 42 kN (4.2 ton) force on the field shaping coils towards the cyclotron mid-plane must also be supported. The shaping coils loads are ~400 times smaller than those on the main coils and thus require a much simpler support structure than the main coil. This then permits designs with shaping coils in a separate cryostat from the main coils if desired.

The shielding coils undergo a 540 kN (54 ton) force pushing them away from the cyclotron mid-plane. This requires then, a relatively simple tension structure.

The shipping loads are discussed below in the section on thermal conduction loads.

9.3 Thermal heat loads from the current leads

The most significant heat load associated with operation of a large superconducting magnet results from the need to bring the magnet operating current from room temperature power supplies to the cryogenically cooled superconducting magnet. There are two main modes for cooling these current leads. One requires cold gas to be introduced at the low end of a pair of resistive current leads, the other relies on thermal conduction to a cooling source located at an intermediate temperature between room temperature and the magnet temperature. Optimized designs for both types of leads have evolved significantly over the last half century to the point where standard design values are readily available. A pair of leads is used for each coil set to bring current both into and out from the cryostat.

The total current to the iron-free cyclotron coils is 3.5 kA, i.e., 3 kA for the series connected main and shielding coils and 0.5 kA for the field shaping coils.

Conduction cooled leads typically require heat removal of 84 W/kA-pair at ~70 K resulting in 294 W total, and approximately 0.2 W/kA-pair near 4 K resulting in 0.7 W total. A high-temperature superconducting link is then used to transmit the current from this intermediate cooling station to the magnet, at a heat load of roughly 0.2 W/kA-pair. Alternatively, vapor-cooled leads require 4.2 K gas flow rate (cooling power) of 1.5 liter/hr/kA-pair (1 W/kA-pair), or 10.5 liter/hr total (7W).

Assuming equal coefficient of performance, a refrigerator between room temperature and:

70 K has Carnot efficiency of roughly 30%

4 K has a Carnot efficiency of roughly 1.5%

After accounting for the difference in cooling mode and refrigerator efficiencies we find that removing the heat lead from the current leads using 4 K helium gas requires ~1/2 the room temperature power (490 W vs. 970 W) compared to conduction cooling of the leads to a cold head at ~70 K.

Other considerations such as complexity of operation, maintenance and initial capital cost also affect which cooling mode is ultimately selected for the cryostat current leads.

9.4 Conduction heat loads

For the gravity supports, typically the heat load to 77 K will be between ½ and 2 W per ton of cold mass. This is especially true if all electromagnetic loads can be supported entirely within the cold mass as we will do for this design.

For a cold mass of ~10 ton, the 70 K structural heat load should be below 20 W. Conduction heat loads to 70 K will thus be small compared to conduction current lead and radiation heat loads.

The use of G-10 compression cylinders in the heat path from 300 K to 70 K can significantly reduce the conduction heat load due to structural supports. The integrated thermal conductivity between 300 K and 70 K for G-10 is roughly 150 W/m.

9.5 Radiation heat loads between 300 K and 70 K

An ~70 K radiation heat shield typically made from 1.5~3 mm thick, high conductivity material like copper or high purity aluminum is generally inserted between the cryostat's room temperature walls and the magnet system to minimize thermal radiation heat load on the coil. Depending on size, the shield may also be reinforced with a layer of stainless steel in parallel. We calculated the heat loads between 300 K stainless steel and various 70 K surfaces using the following values:

- 43 W/m^2 for polished bare copper.
- 12 W/m^2 for copper covered with 3M aluminum tape.
- 6.5 W/m^2 for both copper and stainless steel surfaces coated with 3M aluminum tape.
- 2.5 W/m^2 for copper covered with ~25 layer thick MLI blanket (roughly 10~12 mm total thickness).

Gaps are used to either side of the 70 K radiation shield to accommodate assembly tolerances, differential thermal contractions among components, and limit residual gas heat transfer (gap should be larger than anticipated residual gas mean free path). The residual gas's mean free path is kept low by maintaining moderate vacuum inside the cryostat. Typical radiation shield gaps are: 10~25 mm to 4 K surface, smaller toward the mid-plane bore, larger elsewhere.

A gap of 15 mm to the 300 K surface is added in addition to MLI blanket thickness to allow for assembly clearance and eliminate direct conduction to the MLI blanket. Where absolutely needed, gaps can be reduced to ~3 mm to either side of the radiation shield at the cost of significant increase in local radiation, conduction, and residual gas heat loads. Threaded nylon and G-10 rod are often used as low thermal conductivity supports to maintain gaps between surfaces.

9.6 Transient and Steady State Heat Removal

The magnet design uses a concept called Cable-in-Conduit-Conductor (CICC). The CICC superconductor design was invented and developed at the MIT Plasma Science and Fusion Center for fusion magnet applications. This concept is now used internationally as the baseline conductor for all presently operating and future designs of large scale fusion experiments, including tokamak, helical, and stellarator type magnetic configurations. It has several major advantages over single strand wires or monolithic cables including:

1. Using small diameter round superconducting multifilamentary wires, it can be bundled into single and multi-stage cables carrying large currents.
2. The small wire and superconducting filament diameters result in low ac losses under changing magnetic fields and currents.
3. The cable is cooled by single phase, supercritical helium contained within the conduit (jacket).
4. The small strand diameter results in a very large wetted perimeter for excellent steady state and transient heat transfer of ac losses and other types of disturbance

energy into the surrounding helium. The helium near 4 K has about 100 times higher heat capacity than the solid metallic components.

5. The conduit can be made from a high strength structural steel giving the magnet excellent strength and mechanical properties.
6. Each conductor turn can be fully insulated with fiberglass tape and the winding pack can be epoxy impregnated yielding excellent mechanical and high voltage electrical integrity to the windings. This is particularly important for magnets that are cycled many times.

In most applications the net heat load into the coil windings is removed by force flowing the supercritical helium through each conductor length. In the design approach taken here, we use the sealed CICC concept wherein the conductors are filled with high pressure gaseous helium at room temperature and then completely sealed tight. The coils are then cooled by external means to operating temperature of about 4.5 K. At this temperature, the single phase mass of fluid in the conductor has a drop in pressure to about 3 bar. It is the fluid trapped in the conduit which gives the conductor very high electrothermal stability.

In our design, all the ac losses (magnetic hysteresis and eddy/coupling current losses) are taken adiabatically in the conductor and helium volume. Due to its high heat capacity the temperature of the system only rises by mK over many treatment cycles. The net heat load into this winding pack is then removed conductively by thermal connections to the 2nd stage cold head of one or more cryocoolers. In this type of system then, there is no “bath” or “pool” of boiling liquid helium. This will simplify the logistics of operation tremendously as there is never a need to transfer liquid helium or recover and re-condense helium gas boiloff. The CICC is filled with the helium at the factory and then sealed. No servicing is required. Only the cryocoolers will receive normal yearly or bi-yearly maintenance. Thus the refrigeration system is “hands-free”. The system is cooled down and maintained cold by the cryocoolers.

9.7 Cyclotron Assembly-Beam Extraction Components

To extract the beam at arbitrary energy requires active control over the beam extraction system. The method chosen in the baseline cyclotron was to use a pair of pulsed extraction coils to perturb the beam orbit as it neared the extraction radius to rapidly bring the beam from the final stable orbits to extraction.

This design places several constraints on the extraction coils. First and foremost, they must be compact to easily fit within the cryostat boundaries, leaving sufficient clearance to minimize any scrape off of the beam as it passed through the extraction coils. Next, because it is indirectly conduction-cooled by contact with the main coils it should have slightly higher critical temperature than NbTi. Among the possible conductor choices, filamentary conductors are preferred, such as Nb_3Sn, Bi-2212 and the newly developed, exfoliated fine filament REBCO conductors developed by Brookhaven Technology Group. High-strength conductors, such as the mechanically reinforced Bi-2212 wires developed by Solid Material Solutions simply the mechanical design of the coil supports.

The use of high critical temperature, high current density conductors permits use to maintain a +/- 1cm gap from mid-plane to surface of cryostat vacuum boundary as the beam path passes through the extraction coils.

High current density design permits small overall coil surface area, allowing for an ~3.5 mm thick, stainless steel vacuum walls to the beam chamber facing side of the coil to limit vacuum bending stress below the 2/3 yield stress of stainless steel

We selected a minimum 3 mm gap between the coil and vacuum boundary walls to a 1.5 mm thick radiation shield plus 3 mm gap as a reasonable compromise between the resulting radiation and residual gas heat loads on the coil and the proximity of the coils to the cyclotron mid-plane.

A close-up view of the cryostat section in the vicinity of the extraction coils is shown in Fig. 27. The figure shows respective gaps between the elements discussed above. As before the cross-hatched elements show the coils, the grey shaded elements, the vacuum walls, the orange shaded elements, the radiation shield, and the blue shaded elements, the coil structural supports. Provision for both the beam clearances and internal cryostat clearances leaves requires that the extraction coil facing the beam be positioned ~22 mm from the cyclotron mid-plane (yielding 44 mm separation between the coil surfaces).

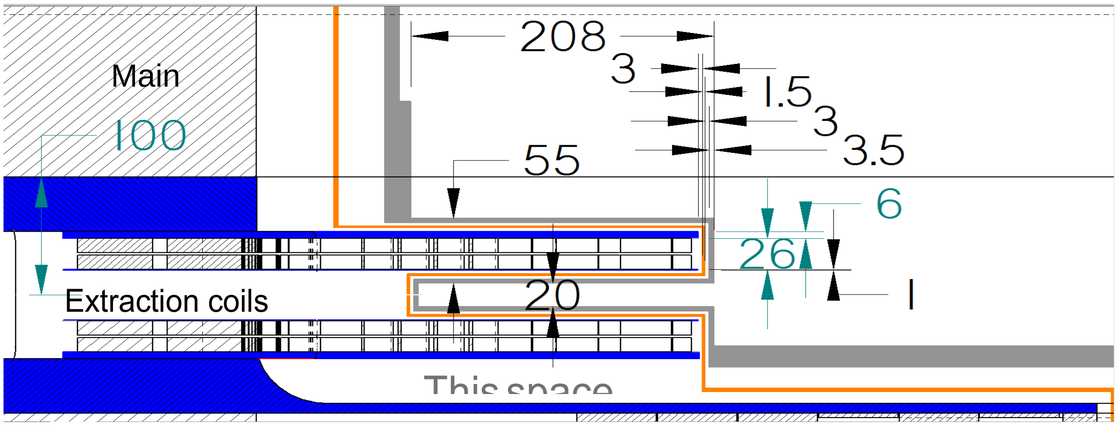

Fig. 27 Close-up section view of the cryostat details near the beam extraction coil

9.8 Beam port dimensions

Because the extraction coils are principally attracted to the nearest main coil there is minimal need for axial support (~1mm thickness), applied principally towards mid-plane side of each coil

Mounting the extraction coils directly to the main coil compression ring not only simplifies the mechanical support, cooling scheme, and extraction coil cryostat design, but restricts ability for in-service adjustment of bump coil position.

An expanded section view of the beam extraction port as it passes through the main coil support structure is shown in Fig. 28.

The 84 mm gas between the cryostat's outer walls in this area facilitates access to beam path for installation of collimation/path correction equipment. As in the case of the extraction coils, the gaps between the cryostat outer walls, radiation shield and main coil support structure is minimized to provide better clearances at the cost of slightly higher local heat loads.

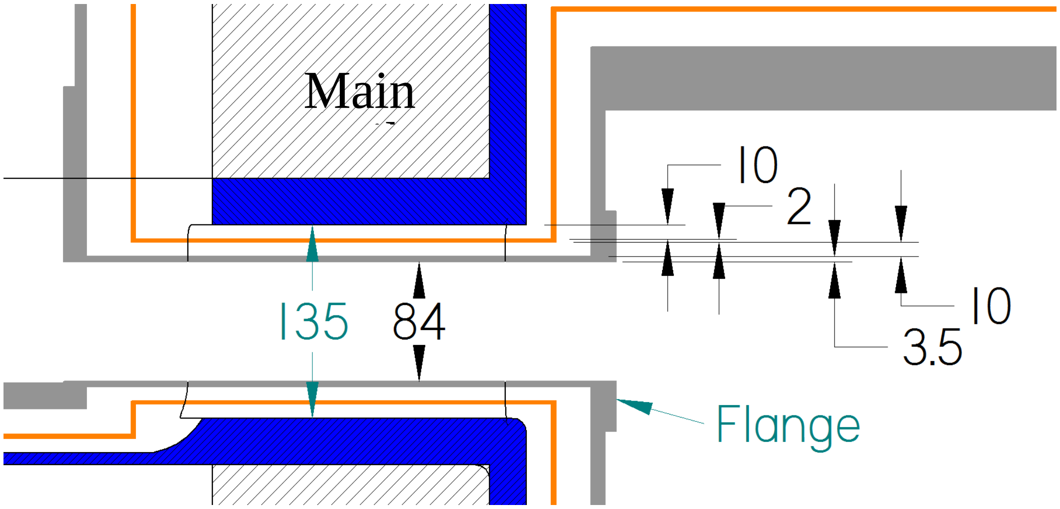

Fig. 28 Expanded section view of the beam extraction port as it passes through the main coil support structure.

9.9 Design challenges

A sectional view of the cyclotron cryostat with the upper field shaping coils removed is shown in Fig. 29. The ability to remove these coils greatly facilitates access to the beam chamber for RF system installation, while minimizing the width of the beam chamber port passing through the main coil support structure. Minimizing the transverse width of the beam chamber access produced stiffer main coil support with less chance of field errors due to main coil deflection. Preliminary estimates indicate that that insertion of the required radio-frequency components through a horizontal port would locally remove ~25% of support cylinder area, resulting in significantly non-axisymmetric deformation of the main coils.

On the other hand, use of a removable cryostat section complicates the support for the field shaping coils due to the non-axisymmetric cryostat design. The removable cryostat section needs to be carefully designed to maintain symmetric position of field shaping coils about midplane as the electro-magnetic force varies from one beam energy to the next.

The lower vacuum boundary wall also needs to be partially carved out to accommodate the upward facing cryostat wall covering the upper extraction coil.

The removable cryostat also requires a slightly more complicated cooling scheme, to ensure that both cryostat sections are adequately cooled. The additional surface area of room temperature walls also adds slightly to the radiation heat load, as do the separate set of room temperature to field-shaping coil current leads and gravity supports.

A more complete final design of the cryostat would consider the implications of a single, unitized cryostat compared to the two-part cryostat proposed here. A few of the main trade-offs would be; field quality, ease of assembly, and cost.

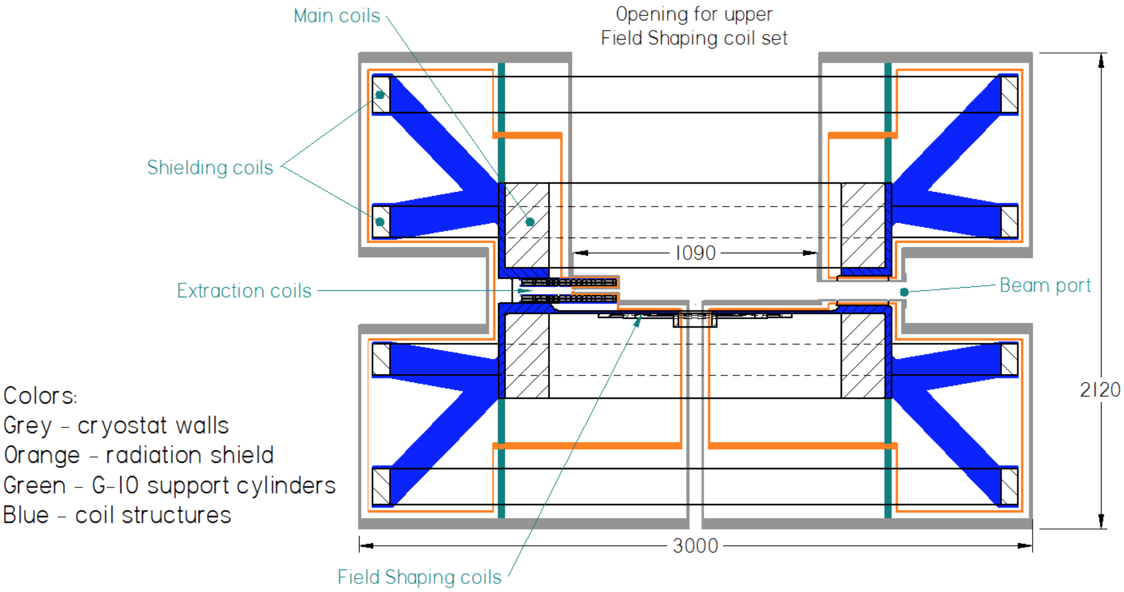

Fig. 29 Section view of cyclotron cryostat with upper field shaping coils removed.

10 Weight Parameters

The following tables characterize weights of the conductor and magnet components are instrumental for making cost estimates.

Table 8 shows length of the cable as well as volume, density and mass of components, i.e. composite strand, copper stabilizer, stainless steel sheath and insulation.

Table 8 Winding Parameters

Conductor		NbTi-a	NbTi-b	All
Length	m	19289	1052	
V_{comp}	m^3	0.2949	0.0060	
$dens_{comp}$	kg/m^3	8502	8502	
M_{comp}	kg	2508	51	2559
V_{cu_stab}	m^3	0.1475	0.0000	
$dens_{cu}$	kg/m^3	8960	8960	
M_{cu_stab}	kg	1321	0	1321
V_{ss_sheath}	m^3	0.3406	0.0038	
$dens_{ss}$	kg/m^3	7990	7990	
M_{ss_sheath}	kg	2722	31	2752
V_{ins}	m^3	0.1248	0.0033	
$dens_{ins}$	kg/m^3	1800	1800	
M_{ins}	kg	225	6	231
Total M_{cond}	kg	6551	82	6863

Table 9 shows overall height, diameter of the cryostat, its surface area, thickness, volume, density and mass.

Table 9 Cryostat Weight

OH	m	2.02
OD	m	3.00
A_{surf}	m^2	37.73
T_{crst}	m	0.0125
Volume	m^3	0.47
dens	kg/m^3	8000
M_{crst}	kg	3773

Table 10 shows thickness, density and mass of an Al radiation shield sized for the cryostat.

Table 10 Radiation Shield Weight

T_{sh}	m	0.0048
dens	kg/m^3	2700
M_{sh}	kg	485

Table 11 shows the weight of the cold mass support structure using volumes from the Opera model.

Table 11 Cold Mass Structure Weight

Material		SS 316LN	Al-6061-T6
V_{str}	m^3	0.142	0.554
M_{str}	kg	1135	1496

And finally, Table 12 summarizes all components and shows that the weight of the magnet is close to 14 tons.

Table 12 Magnet Weight

Coils	kg	6,863
CM structure	kg	2,630
Cryostat	kg	3,773
Shield	kg	485
Total	**kg**	**13,752**

11 RF System and Acceleration Chamber

11.1 RF power supply for a variable energy synchrocyclotron

A key feature to the ironless design is the enabling the energy of the proton treatment beam to be set to any desired value by tuning the magnetic field in the cyclotron to a corresponding value.

During the treatment phase of the cycle, the RF equipment should operate in conventional modes for synchrocyclotrons, sweeping through a range of frequencies. The beam energy needs to be changed requiring readjustment of the RF waveform. Typically, up to 15 energy levels are needed to cover the entire treatment volume. Four times repainting strategy requires up to sixty changes in energy during a targeted 2 minute patient treatment time.

11.1.1 RF system implications

Specifications of the cyclotron and RF unit are shown in Table 13. The extracted beam from the synchrocyclotron has variable energy, and each extracted energy corresponds to a range of swept frequencies. The beam rep-rate is 1 kHz. The RF needs to sweep the frequency of interest. The frequency sweep varies with extracted energy. The sweep duration is about 0.5 ms, with a reset of about 0.5 ms. For the highest extracted energy (230 MeV), the RF starts at about 76 MHz to accelerate the beam near the axis of the machine, and decreases to about 54 MHz at extraction. Similarly, at the lowest extracted energy (70 MeV), the RF starts at 47 MHz and then decreases to about 29 MHz.

The change in frequency per step in energy is about 0.5%. The frequency span decreases slightly with energy, as described below. There is a 0.5 s delay between changes in frequency spans, as the magnetic field in the cyclotron is varied.

In order to best accelerate the beam, it is desirable that the frequency ramp rate be adjustable, not linear in time. In principle, it would be ideal to have frequency control of the unit, in order to match the RF phase to that of the beam. However, it would be adequate to be able to adjust the frequency sweep rate using a preprogrammed waveform generator (open loop, but adjustable). The ramp rate may differ for different extracted beam energies.

Table 13 RF Acceleration Requirements

repetition rate	kHz	1
Change in frequency span	s	0.5
Change in upper/lower frequencies		0.50%
Highest frequency span (230 MeV)	MHz	76-54
Lowest frequency span (70 MeV)	MHz	41-33
Dee's capacitance	pF	54-66
Voltage across Dee's	kV	20

Shown in Table 13 is the requirement for the accelerating voltage across the dees. In order to be able to accelerate the beam in about 1 ms, about 5-10 kV are required across the dees. We are specifying the voltage across the dees. The beam loading is small, as the average beam current is in the nA level, and the beam energy is 230 MeV. Most of the power is dissipated in the driving circuit.

Fig. 30 shows the RF frequency that results in resonant conditions for protons as a function of radius, for 230 MeV extraction beam energy. The magnetic field determines the frequency at each radius. As the beam accelerates, the RF is not changing frequency linearly. Because of the need of optimizing the beam acceleration for the different energies, it is desirable that the frequency be adjustable as a function of time, as mentioned above, in a preprogrammed way (open loop), or in a closed-loop. However, to start with, open loop frequency control would be adequate.

Fig. 31 shows the peak frequency (*i.e.*, for acceleration near the axis of the machine) relative to the frequency required at full energy. Also shown in the Figure is the frequency of the RF at beam extraction, as a function of the beam energy, relative to the frequency required at full energy. The RF frequency decreases less for the extraction location, due to relativistic effects at the highest extracted energy which decreases the energy required for resonance at extraction of the beam, for the highest beam extracted energy. Thus, the span (bandwidth) of the RF changes with energy. Therefore, scaling the frequency with the magnetic field is not applicable, and more control of the variation of the frequency with time is needed than a simple scaling. In principle, the RF may remain on beyond the extraction time, if that is useful.

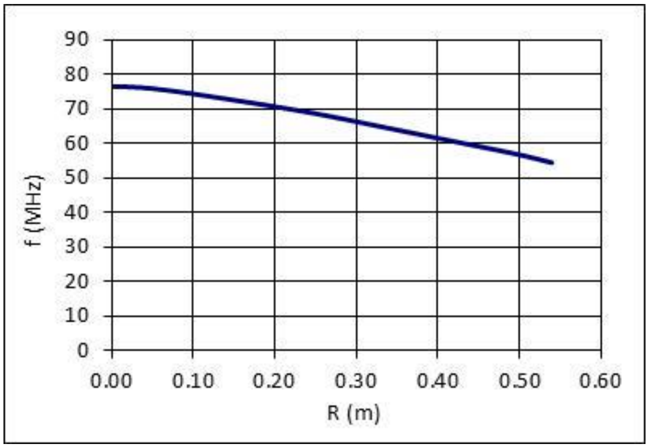

Fig. 30 Frequency as a function of radius for 230 MeV beam.

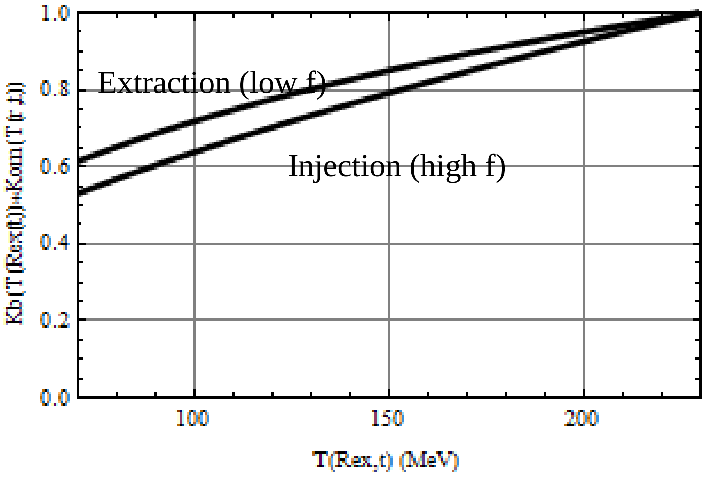

Fig. 31 Ratio of central frequency and extraction frequency as a function of beam energy.

The capacitance of the dees in the accelerating chamber is shown in Fig. 32 as a function of frequency. At the lower frequencies, the capacitance decreases. There is no resonance near the region of interest. The fundamental resonance frequency is over 100 MHz.

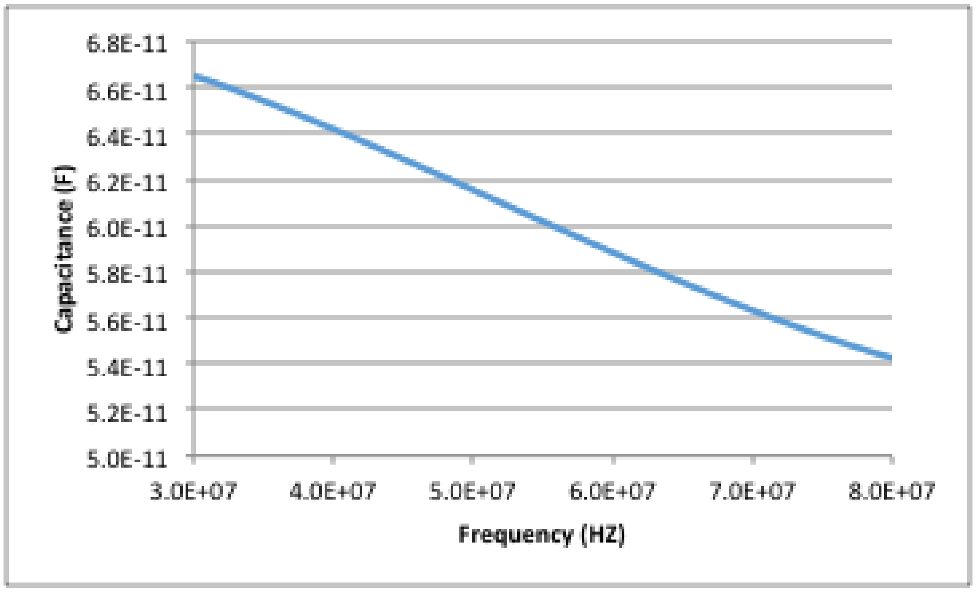

Fig. 32 Capacitance of the dee-structure as a function of frequency

The geometry is shown in Fig. 33. Only half of the cyclotron accelerating cavity and one dee are used, with a symmetry boundary condition on the midplane. The corresponding electric field profile is shown in Fig. 34.

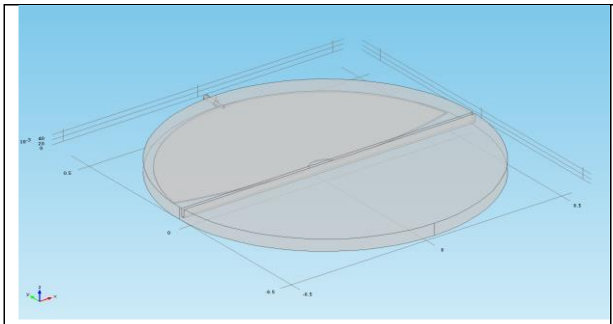

Fig. 33 RF Cavity.

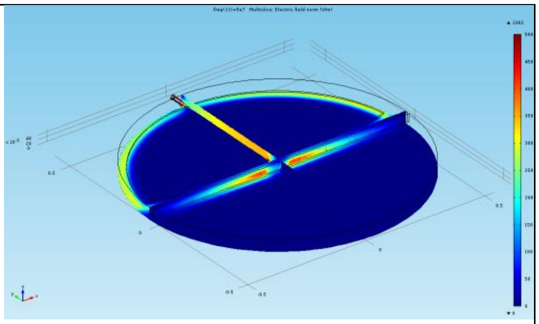

Fig. 34 Electric field distribution in cavity.

It is desirable to have a specific rate of change of frequency, which is different for different extracted energies. For example, Fig. 35 shows an illustrative time-dependent frequency for the case of 230 MeV extraction energy.

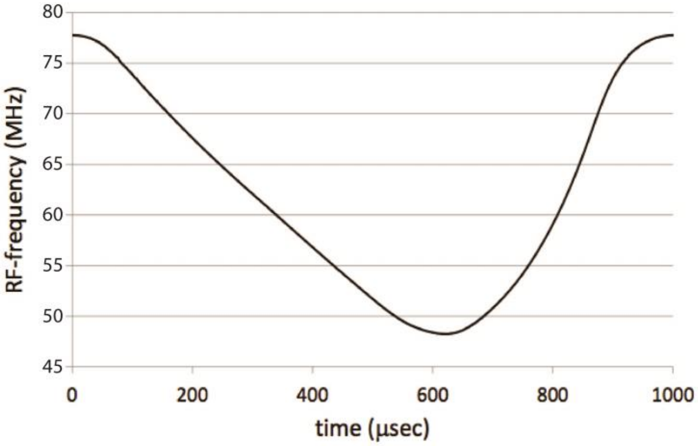

Fig. 35 Frequency vs time for the case of 230 MeV extraction energy.

Fig. 36 shows illustrative the performance of the electronics. The waveform shown in Fig. 28 is repeated a number of times (up to 500). Then the accelerator configuration is modified (by decreasing the magnetic field and the RF sweep) in about 0.5 s, before repeating the process for another 0.5 s (Fig. 29).

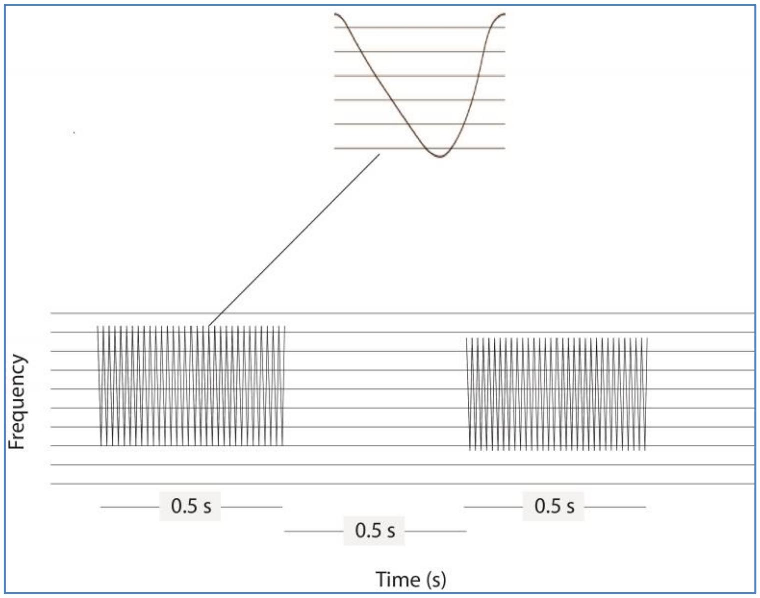

Fig. 36 Illustrative RF operation.

Control over the voltage during the frequency span would also be beneficial. This feature would be particularly useful if we have accurate control of df/dt during the acceleration phase. It would also be adjustable, that is, the dV/dt across the gap would also dependent on the time, and it would be different for different extraction energies. It does not require large modulation. A change of 3 dB would be sufficient for the optimized operation of the synchrocyclotron.

11.1.2 Power supply considerations

Two potential solutions were investigated. The use of a rotating capacity (RotCo)[6] is the conventional means of driving synchrocyclotrons. The other one, more speculative, uses solid state equipment.

11.1.2.1 Rotating capacitor

Traditionally, a mono-energetic synchrocyclotron (SC) uses a rotating-vane capacitor (condenser) in the tuned resonant power oscillator circuit to achieve the required frequency sweep. The sweep, of course, is not necessarily linear in time depending on the field index and designed field map, and the proposed machine will need to sweep the frequency range in 500 μs with a dwell time of 500 μs. A conventional rotating capacitor typically gives a frequency spread of as much as 1.5:1, which is perfectly suitable to a mono-energetic machine. However, the required frequency spread in the proposed machine is nearly twice that which is achievable by a conventional single rotating capacitor approach.

Additionally, the usual approach for a rotating capacitor solution requires a high-power electron tube with the resonant tank in the circuit. Such a tube-based approach

---

[6] Variable Rotating Capacitor for Synchrocyclotron, Michael Abs, US Patent 20140103839A1

automatically ties the system to a device (the power tube) whose obsolescence and difficulty in sourcing increases daily. The ironless cyclotron requires roughly 10 kV across the dees, and of course, a constant amplitude across the range. Achieving this with a single rotating condenser in a plate circuit, even with feed-forward or close-loop amplitude control would is possible but challenging.

There are several possibilities for matching the requirement. A first approach is to use a single sweep, but inject the beam at different times during the sweep, to match cyclotron frequency in the central region, as the magnetic field is varied. The time of injection (referenced to the RF field sweep) varies with magnetic field (and thus, final ion beam energy).

The second approach is to use a fast moving RotCo to apply the variation in the resonant frequency required for the acceleration, while using a second variable capacitor to vary the center frequency of the oscillator.

A third approach is to combine the rotating capacitor with vanes that can be rotated with respect to each other, in order to vary the capacitance of the rotating condenser, and thus the resonant frequency. This approach requires substantial development, and if such a development would be undertaken, the option of the all solid-state components deserves attention.

11.1.3 Solid state approach

We have also explored a solid-state, truly variable-frequency amplitude-modulated approach. We acknowledge the help of Fred Niell of Nielltronix, Inc.

A solid-state biased-ferrite based tuner is used to provide the required D voltage at the full range of frequencies and frequency ramp speeds. This tuner directly supports the immediate requirements of the cyclotron, but also provide additional flexibility in frequency, ramp, and amplitude variation. The overall RF system is designed to integrate seamlessly with the dee supports and vacuum chamber of the eventual machine. The conceptual design is a 1/2 wave microwave-ferrite-loaded and liquid-filled resonator, utilizing perpendicular biasing of the ferrite, and an external solenoidal bias field (Fig. 37). The tuner will also utilize general-purpose power-transformer ferrite for a flux return path in order to minimize bias-field power and voltage compliance requirements. The bias field will be servo loop controlled with a phase detector and power amplifier arrangement to automatically tune the resonator to the imposed drive frequency. RF power will come from a wide-band RF amplifier fed by a computer-programmable LLRF oscillator. Amplitude in the dees will be either feedback or feedforward controlled as required by the customer. The overall system will allow agile frequency and voltage control, while still achieving the required pulse repetition rate of 1 kHz shown in Fig. 37. This ambitious target will leverage recent advancements in microwave ferrite materials and current research in biased ferrite tuners.

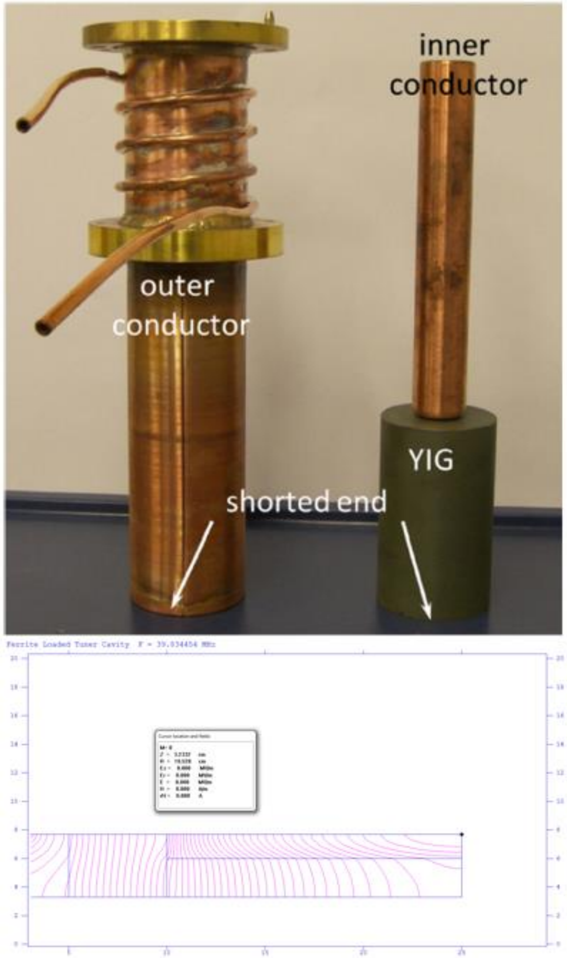

Fig. 37 Above: conceptual foreshortened 1/2 wave prototype cavity. Below: Superfish simulation of the cavity with smaller garnet toroids.

The oscillator would utilize the latest microwave garnet ferrites in a perpendicular bias arrangement, with input and output taps set to the appropriate impedances, obviating the need for high power matching circuitry.

A number of potential topologies for the tuner and associated RF driver, well-suited to operation at the full required bandwidth and power.

11.2 RF System Approach

Current approaches to the biased-ferrite resonator have moved beyond that of the parallel-bias-field quarter-wave NiZn ferrite resonator days. The most recent upgrades to the FNAL booster RF system have allowed the overall loaded Q of the cavity to swing between 300 and 1200 in operation. This loss means that the power required to achieve the 10kV in the present work would be far in excess of what makes sense, not to mention cooling the lossy ferrites.

Recently, perpendicular bias ferrite cavities, pioneered at LAMPF and other modern accelerators, allow for high Q microwave materials to operate in lower frequency resonators. The associated low-loss, high Δf cavity approach makes it well suited this application. The difficult portion of the cavity design will be choosing a magnetic yoke, bias field, and resonator structure that will allow rapid cycling. Recently, the slip-stacking injector cavities at FNAL have demonstrated fast tuning with Al-doped garnet ferrites through careful design of the solenoid, yoke, and tuner modules. Wider Δf is certainly possible with greater amounts of ferrite in the cavity and a greater tolerance for losses.

Fig. 38 shows an example biased cavity made of EIA 6-1/8 straight section, with quasi-Helmholtz field windings, and a ferrite flux return structure. The garnet is shown with a nearly uniform field in red-orange, while the bias coils are shown in blue. Using volume integrals method, the inductance of the coil and ferrite arrangement shown is 74 µH with a peak current of 100 A achieving 700G in the garnet. Via the method of volume integration of the model, the inductance of the coil arrangement to achieve the proper flux density for the material's 4π Ms and required frequency is only 74 µH with an applied current of 100 A. The cavity would use AL-0800 Al:YIG garnet ferrites. This approach alleviates the bias current power supply requirements over typical parallel-bias tuner arrangements, and to first order would only require 1.2 kW of bias power on average at the required 1 kHz rep rate.

The next level of challenges lies in achieving the required frequency swing with the necessary power density. Preliminary calculations show that the swing in frequency from 30-76 MHz is easily achievable with an overall minimum cavity Q of approximately 1500. Given that the garnet is immersed in cooling fluid, a power density of over the traditional rule-of-thumb of 0.6 W/cm^3 will be allowed. Water cooling of the outer jacket above the flux return structure will allow convective pumping of the dielectric fluid, and consequently, cooling of the ferrite. Losses in the material are roughly given by $P \cong 2.2\pi f \mu'' V \langle H \rangle^2$ $P \cong 2.2\pi f \mu'' V \langle H \rangle^2$ where V is the volume of ferrite, and μ'' is the imaginary component of the complex permeability. In this case, Models indicate that the power in the ferrite will be approximately 3 kW to achieve the required 10 kV with a power density close to 1 W/cm^3. Cooling may need more aggressive spacing between toroid ferrites, or a dead line before and after the garnet. Cooling of the ferrite and cavity walls will be achieved by winding a copper cooling line around the inactive region of the resonator wall, and soldering the cooling pipe to the cavity wall for good heat transfer. Heat will be removed from the ferrite by filling the entire resonator with Shell Diala-ZX transformer oil, and convective transfer in the oil. In any event, this dissipation is manageable.

The garnet ferrites can be obtained from Trak Ceramics Inc. and Trans-Tech Inc.

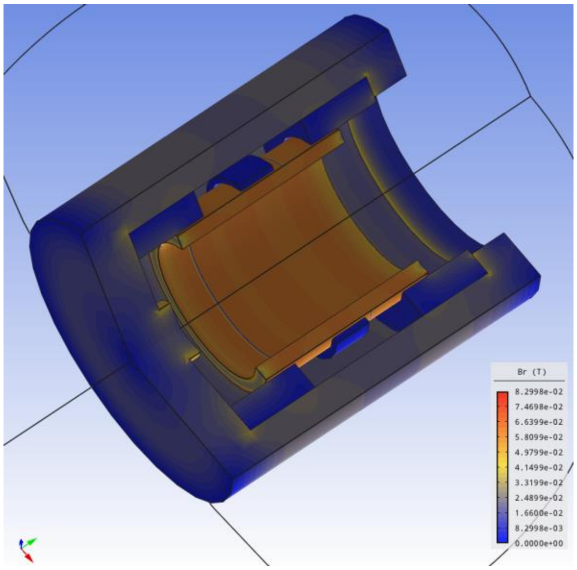

Fig. 38 Quasi-Helmholtz bias coil arrangement with flux return yoke.

12 Variable Beam Energy

Variable beam energy is accomplished by modulating the coil current, which results in linearly proportional change of the magnetic field in the beam space. This process, which we have patented [24], has implications both for the magnet itself and for the beam controls. They are addressed separately in this chapter.

12.1 Magnet Field and Operating Current Modulation

Let us assume that the beam energy at extraction is a given function of time, T(R_{ex}, t). This function will be defined later. The following defines governing equations of a variable synchrocyclotron. They are:

$$\gamma\ (R_{ex}, t) = 1 + \frac{T(R_{ex}, t)}{E_0} \tag{3}$$

where E_0 = 938.27 MeV, R_{ex} = 0.501 m, T(R_{ex}, 0) = 230.03 MeV

$$B\rho(R_{ex}, t) = \frac{p(R_{ex}, t)}{q} = m_0 \frac{c}{e} \sqrt{(\gamma(R_{ex}, t)^2 - 1)} \tag{4}$$

where m_0 = 1.67262E-27 kg, e = 1.60218E-19, c = 299792458 m/s

Field at Extraction,

$$B(R_{ex}, t) = \frac{B\rho(R_{ex}, t)}{R_{ex}} \tag{5}$$

Magnet Energy,

$$E_m(t) = E_m(0) * K_b(t)^2 \tag{6}$$

Here

$$K_b(t) = \frac{B(R_{ex}, t)}{B(R_{ex}, 0)} = \frac{I_{op}(t)}{I_{op}(0)} = \sqrt{\frac{T(Rex, t)\big(2E_0 + T(Rex, t)\big)}{\mathrm{T}(Rex, 0)\big(2E_0 + \mathrm{T}(Rex, 0)\big)}} \tag{7}$$

is the field/coil current scaling coefficient, $E_m(0)$ is the maximum EM energy of the magnet at the Basic Working Point corresponding to t = 0. For the current design, $E_m(0)$ = 31 MJ, $I_{op}(0)$ = 3 kA and B(R_{ex},0) = 4.637 T.

An expected beam energy versus time scenario consists of repetitive patterns comprised of two parts, a constant energy (and respectively magnet coil current) portion during painting a single layer and a transition to the next layer accomplished by ramping the operating current of the magnet.

For a T_{min} = 70 MeV and T_{max} = 230 MeV synchrocyclotron the layer to layer beam energy change was defined as constant ΔT = 4.5 MeV linear ramps, each lasting Δt_{L2L} = 0.5 seconds. The constant beam energy intervals during which the in-layer painting takes place are set to a constant, dt_{lay} = 0.5 s, for each layer.

Within time intervals, during which the beam stays in a single layer, the terminal voltage is zero. For the purposes of specifying the requirements for the magnet these intervals can be dropped assuming dt_{lay} = 0 s and layer-to-layer transitions can be considered as a continuous process governed by equations (6), (7) and the T(R_{ex}, t) scenario. For a 230 MeV cyclotron this means that the beam energy, T(R_{ex}, t), is linearly reduced from T(R_{ex},0) = 230 MeV to 70 MeV in 17.8 seconds at a rate of 9 MeV/s by the following function of time.

$$T(R_{ex},t) = T(R_{ex},0) * \left(1 - \frac{t}{25.56}\right) \tag{8}$$

for $0 < t < 17.8$ s

The following diagrams in Fig. 39-Fig. 44 illustrate the variation of the characteristics of the magnetic system as a function of time.

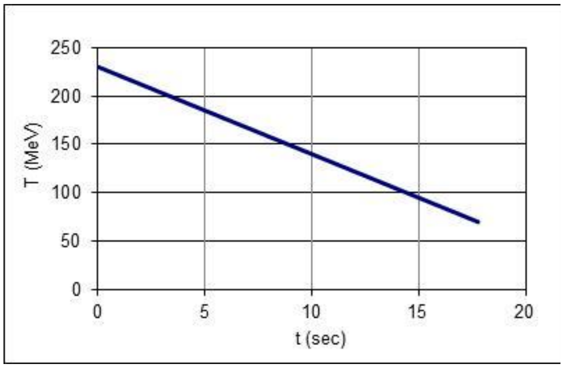

Fig. 39 Beam energy vs. time

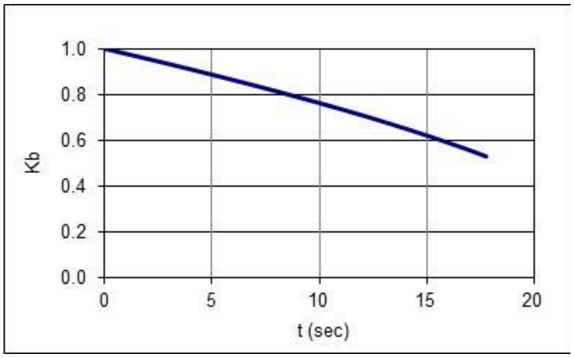

Fig. 40 Field/Coil Current Scaling coefficient vs. time

Let us assume that the coils are in series. Then the terminal voltage will vary as

$$V(t) = \frac{P(t)}{I_{op}(t)}, \qquad where\ P(t) = \frac{dE_m(t)}{dt}\ and\ I_{op}(t) = K_b(t) * I_{op}(0) \tag{9}$$

Lest us first address the more challenging Circuit A[7]. The stored EM energy, E_m(t), the power, P(t), the operating current, I_{op}(t), and the terminal voltage, V(t) are shown in Fig. 41 - Fig. 44 as a function of time.

---

[7] Ramping voltages in the less challenging Circuit B are addressed in the next section. Current change in Circuit B is proportional to that of Circuit A.

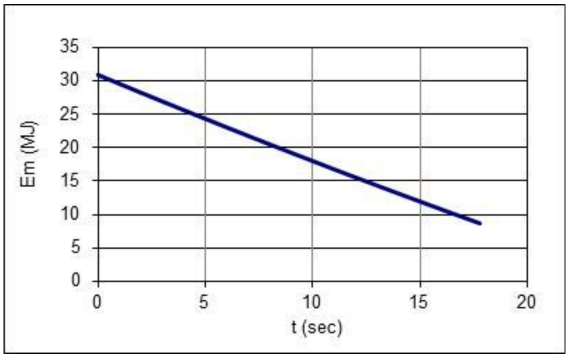

Fig. 41 EM energy vs. time

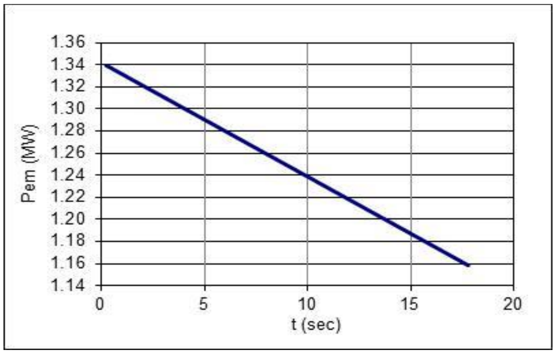

Fig. 42 EM Power vs. time

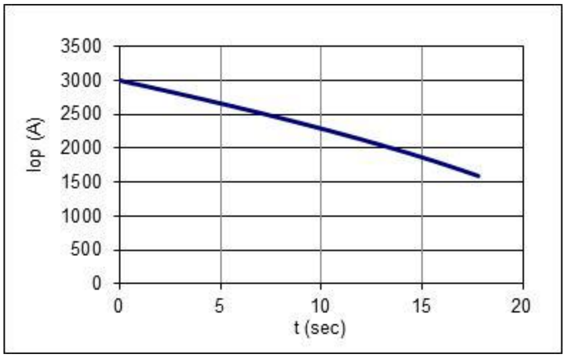

Fig. 43 Operating Current vs. time

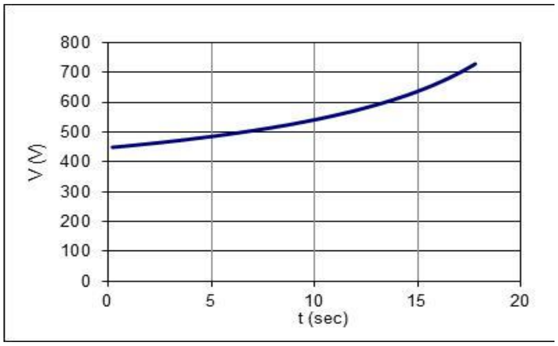

Fig. 44 Terminal Voltage vs. time

A more convenient representation of the characteristic parameters of the magnet can be presented using the beam energy as a parameter.

From (6) - (8) and

$$L\frac{dI_{op}(t)}{dt} = V(t) \tag{10}$$

$$L = 2 * \frac{E_m(0)}{I_{op}(0)^2} \tag{11}$$

and

$$\frac{dI_{op}(t)}{dt} = \frac{dI_{op}(t)}{dT(R_{ex},t)}\frac{dT(R_{ex},t)}{dt} \tag{12}$$

where the inductance, L, of the magnet is defined by the EM energy, $E_m(0)$, and current, $I_{op}(0)$, at the Basic Design Point corresponding to $T(R_{ex},0)$, we can directly derive the following formulae

$$\mathrm{I}_{op}(\mathrm{t}) = \mathrm{I}_{\mathrm{op}}(0)\sqrt{\frac{T(R_{ex},t)\big(2E_0 + T(R_{ex},t)\big)}{\mathrm{T}(R_{ex},0)\big(2E_0 + \mathrm{T}(R_{ex},0)\big)}} \tag{13}$$

$$\mathrm{V}(t) = L * \mathrm{I}_{\mathrm{op}}(0)\frac{\big(E_0 + T(R_{ex},t)\big)}{\sqrt{T(R_{ex},t)\big(2E_0 + T(R_{ex},t)\big)\mathrm{T}(R_{ex},0)\big(2E_0 + \mathrm{T}(R_{ex},0)\big)}}\frac{\mathrm{dT}(R_{ex},t)}{\mathrm{dt}} \tag{14}$$

$$\mathrm{P}(t) = \mathrm{V}(t) * I_{op}(\mathrm{t}) \tag{15}$$

Per (9) $\frac{dT(R_{ex},t)}{dt}$ = 9 MeV/s and the following Fig. 45, Fig. 46 and Fig. 47 show the operating current, the terminal voltage and the driving power as a function of the beam energy.

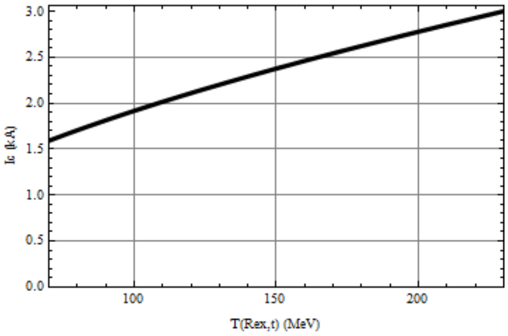

Fig. 45 Operating Current vs. Beam Energy

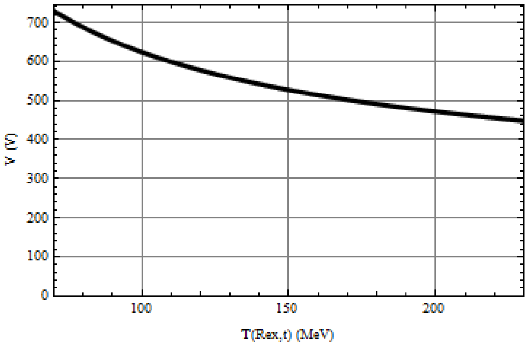

Fig. 46 Terminal Voltage vs. Beam Energy

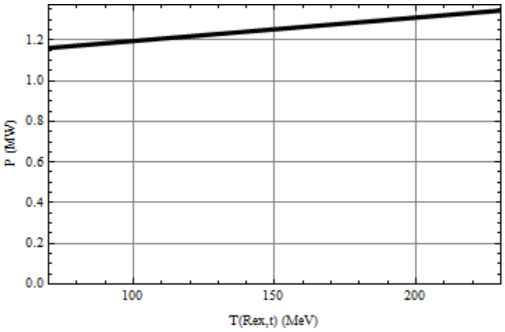

Fig. 47 EM Power vs. Beam Energy

The ranges of variation of these parameters, 1.59 kA < I_{op} < 3 kA, 0.45 kV < V < 0.73 kV, 1.16 MW < P < 1.34 MW, in respective pairs of (Fig. 43 and Fig. 45), (Fig. 44 and Fig. 46) and (Fig. 42 and Fig. 47) are in agreement.

As said above, the beam energy versus time scenario consists of repetitive patterns comprised of two parts, a constant energy (and respectively constant magnet coil current) portion during painting a single layer and a variable beam energy transition to the next layer.

Fig. 48 shows the beam energy vs. time scenario, T(t), for 4 cycles of in-depth repainting. Each cycle takes about 17.8 seconds adding up to 71.2 s for 4 cycles. This simplified scenario follows the above logic of dropping the constant beam energy, $\Delta t_{L2L,}$ time increments, during which the coil current stays constant.

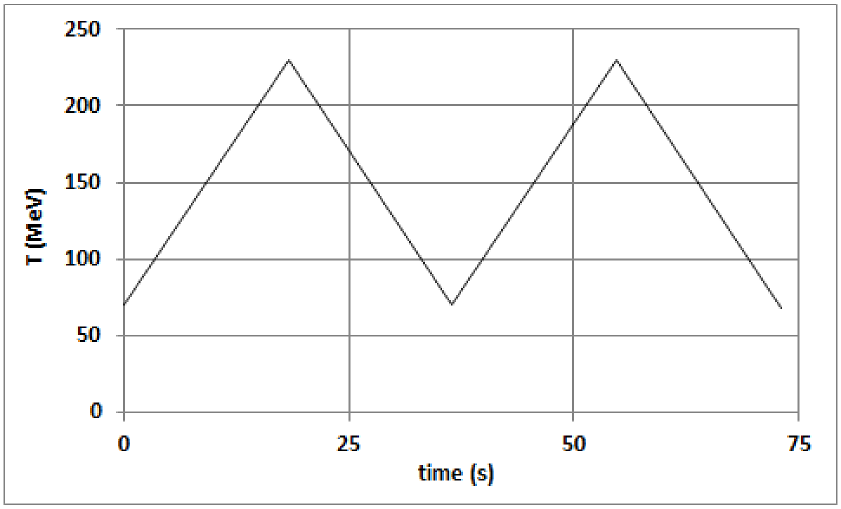

Fig. 48 Simplified Beam Energy vs time Scenario

Fig. 49 - Fig. 52 show the beam energy, coil current, terminal voltage and driving power as a function of time for a more realistic scenario including both $\underline{\Delta} t_{L2L}$ = 0.5 s and $\underline{\Delta} t_{lay}$ = 0.5 s increments. They depict only one of four ramps shown in Fig. 47. The challenging voltage and power requirements to the magnet power supply are illustrated in Fig. 50 and Fig. 51.

The duration of the cycle is 37 seconds, which will add up to about 2.5 minutes for 4 cycles.

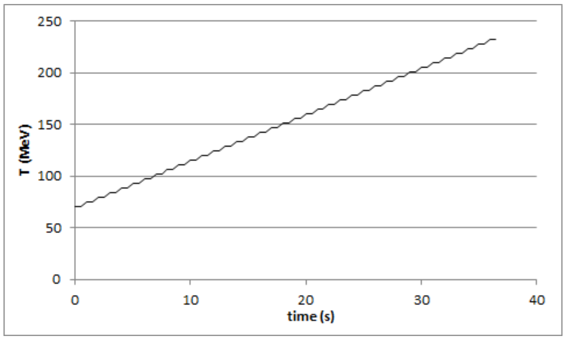

Fig. 49 Beam Energy vs time, First Ramp

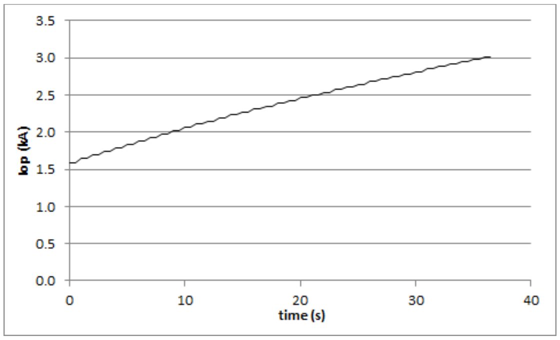

Fig. 50 Coil Current vs time, First Ramp

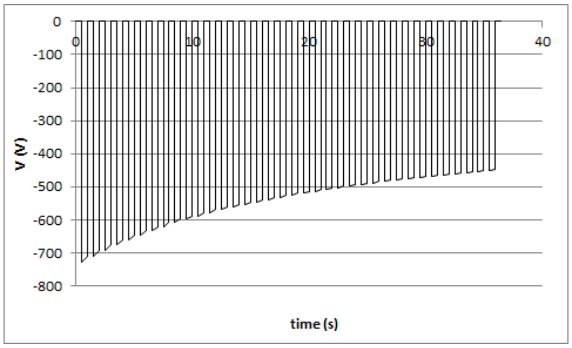

Fig. 51 Terminal Voltage vs time, First Ramp

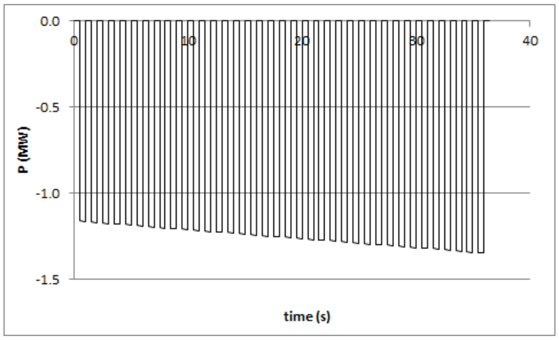

Fig. 52 EM Power vs time, First Ramp

12.2 AC Losses and Ramping Voltage

The magnet design permits accelerating the beam to variable energies. Let us assume that the range of the beam energies is between 70 MeV and 230 MeV and that the magnet current is ramped between I_{op} and alpha* I_{op} in t_{ramp} = 17.8 sec. For this particular, fixed R_{ex} = 50 cm, design B_{ex}(230 MeV) = 4.64 T, B_{ex}(70 MeV) = 2.46 T and alpha = 0.53.

There are several magnet-related issues associated with the energy variation. The first one is the account of AC, coupling and eddy losses in the conductor. Coupling and eddy losses will be assessed later. AC losses, e, in the superconductor were calculated using the Kim model[8],

$$e = \frac{2}{3\pi} d_f B_0 J_0 \ln\left(\frac{B_0 + B_f}{B_0 + \alpha B_f}\right) \tag{16}$$

where d_f = 6.5 μm is the SC filament diameter[9], B_0 = 0.38 T, J_0 = 4e10 A/m^2, $\alpha = B_i/B_f$, B_i and B_f - initial and final local B-field.

---

[8] Martin N. Wilson, "Superconducting Magnets," Oxford Press, 1983. See (8.64)

[9] Furukawa wire spec, see reference above.

AC losses in each of the conductors at the locale of the maximum field are shown in Table 14.

Table 14 AC Losses in SC

Conductor		NbTi-a	NbTi-b
B_0	T	0.38	0.38
J_0	A/m^2	4.00E+10	4.00E+10
d_f	m	6.50E-06	6.50E-06
alpha		0.53	0.53
B_f	T	6.56	5.36
e_h	J/m^3	5349	5261
	mJ/cc	5	5

Introducing these losses into the CICC tool shows that even for multiple, say 4, up-down in-depth repaintings the associated temperature rise changes T_{op} only in the third digit.

Another consequence of the ramping is the need to access the driving voltages. They can be easily defined using circuit equations defined in the previous section as shown in Table 15.

Table 15 Driving Voltage during Ramps

Circuit		A	B
I0	A	1590	265
I1	A	3000	500
t_{ramp}	s	17.8	17.8
dI/dt	A/s	544	20
L	H	6.82	0.12
M	H	0.24	0.24
V_{ramp}	V	544	20

Ramping voltages are much smaller than those during the quench dump.

12.3 Scaling Beam Controls

Modulation of the beam control parameters in a variable beam energy synchrocyclotron can be done in a multitude of different ways, in other words it does not have a unique implementation.

Let us consider conditions, which have to be satisfied so that the beam trajectories for any beam extraction energy are the same. This issue has specifics for the parts of the trajectory before and after extraction. Let us address them one at a time.

12.3.1 Non-Linear Frequency Ramp during Acceleration

Before extraction, i.e. during acceleration we have control over the particle by moderating both the RF frequency and the per turn particle energy gain (by adjusting the gap voltage).

Let us extend assumptions made in Section 12.1 (for the extraction radius) to the whole acceleration trajectory by adding another independent variable, r, the radius of the particle trajectory.

The governing equations are, beginning with the equation of equilibrium,

$$m_0 * \gamma(r,t) * \omega(r,t)^2 * r = B(r,t) * e * \omega(r,t) * r \tag{17}$$

Relativistic equations,

$$\gamma(r,t) = \sqrt{1 + \left(B(r,t) * \frac{e * r}{m_0 * c}\right)^2} = 1 + \frac{T(r,t)}{E_0} \tag{18}$$

Let us assume that,

$$\mathrm{\omega(r,t)} = K_b(\mathrm{t}) * K_\omega(\mathrm{r,t}) * \mathrm{\omega(r,0)} \tag{19}$$

$$\mathrm{B(r,t)} = K_b(\mathrm{t}) * \mathrm{B(r,0)} \tag{20}$$

where $K_b(0) = 1$ and $K_\omega(r, 0) = 1$ are unities at the Basic Design Point, t = 0.

The Basic Design Point beam profile, B(r, 0), is defined in Section 6.

Equations (17) - (18) at t = 0 yield a corresponding RF frequency profile

$$\omega(r,0) = e * \frac{B(r,0)}{\left(m_0 * \gamma(r,0)\right)} \tag{21}$$

where $\gamma(r,0) = \sqrt{1 + \left(B(r,t) * \frac{e*r}{m_0*c}\right)^2}$

Equations (17) - (21) yield the following correction coefficient for the RF frequency

$$K_\omega(\mathrm{r,t}) = \frac{\mathrm{\gamma(r,0)}}{\mathrm{\gamma(r,t)}} \tag{22}$$

Field profile, B(r, 0), field/coil current scaling coefficient, $K_b(t)$, defined by (3) - (8), jointly with (21) and (22) fully define frequency and field modulation both radially and as a function of the beam extraction energy (i.e. time).

The field and the frequency scaling parameters (19-20) can be written as a function of beam energy during acceleration, $T(r,t)$, and at extraction, $T(R_{ex},t)$, as

$$K_b\big(T(R_{ex},t)\big) = \sqrt{\frac{T(R_{ex},t)\big(2E_0 + T(R_{ex},t)\big)}{\mathrm{T}(R_{ex},0)\big(2E_0 + \mathrm{T}(R_{ex},0)\big)}} \tag{23}$$

$$K_b\big(T(R_{ex},t)\big) * K_\omega\big(T(r,t)\big) = \sqrt{\frac{T(R_{ex},t)\big(2E_0 + T(R_{ex},t)\big)}{\mathrm{T}(R_{ex},0)\big(2E_0 + \mathrm{T}(R_{ex},0)\big)}} * \left(\frac{1 + \frac{T(r,0)}{E_0}}{1 + \frac{T(r,t)}{E_0}}\right) \tag{24}$$

This form is convenient for assessing the range of variation of the coil current and of the acceleration frequency with respect to their definitions for the Basic Design in Section 6.

Fig. 53 shows the field scaling coefficient (23) as a function of extraction energy. Fig. 54 shows two traces of the frequency scaling coefficient (24), the upper one is at extraction and the lower one is in the central region, where the beam energy can be assumed to be zero, $T(r,t) = T(r,0) = 0$. Both the field and the frequency coefficients grow with the extraction beam energy reaching a unity at the Basic Design Point.

This implies that the minimum frequency, 34.9 MHz, occurs at extraction in the mode corresponding to the minimum beam energy of 70 MeV and the maximum frequency, 76.6 MHz, is at the beginning of acceleration at the Basic design point.

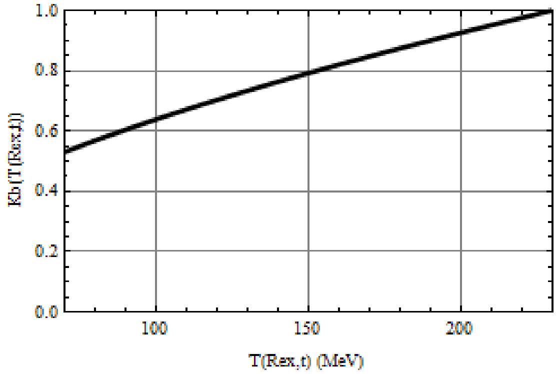

Fig. 53 Field Scaling Coefficient vs Beam Energy at Extraction for Basic Design.

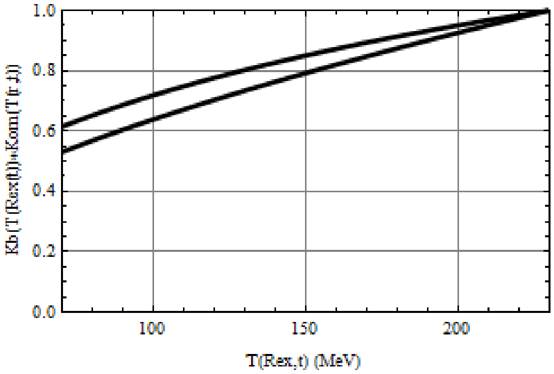

Fig. 54 Acceleration Frequency Scaling Coefficient at Extraction (top) and in the Central Region (bottom) vs Beam Energy at Extraction for Basic Design.

The last parameter that shall be matched is the particle energy as a function of both radius (r) and beam extraction energy (t). From (18-20) we can derive

$$T(r,t) = E_0 * \left(\sqrt{1 + \left(K_b(t) * B(r,0) * \frac{e * r}{m_0 * c} \right)^2} - 1 \right) \tag{25}$$

Matching T(r,t) can be achieved by a run-time adjustment of the per turn RF voltage. Quantitative assessment of this variation will be done after defining more parameters of the RF system, per-turn gain in particular.

12.3.2 Linear Frequency Ramp during Acceleration

From the standpoint of the instrumental implementation of this RF system the most challenging feature is varying the RF frequency during the time of flight. This frequency variation has to follow different scenarios as a function of the extraction beam energy. A state-of-the-art instrument for the RF frequency vs time variation is a rotating capacitor, RotCo [25]. It is tuned for a single frequency vs time profile for the IBA S2C2 synchrocyclotron as shown in Fig. 55 reproduced from [26].

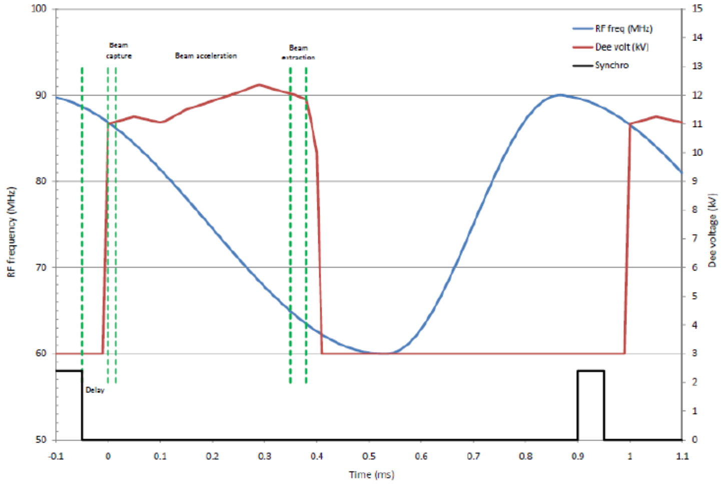

Fig. 55 RF frequency and voltage during acceleration cycle in IBA S2C2.

Note that during a single acceleration cycle (a) the frequency (blue line) is an almost linear function of time and (b) the dee voltage can be varied as a function of time. These features will be discussed below.

The alternative RF strategy proposed in this study for the variable energy synchrocyclotron assumes that a RotCo-type device will be used for varying the RF frequency during the flight. This approach may significantly simplify the instrumental implementation of the RF system.

Let us assume that we use a single RF frequency generator designed to repetitively produce a constant-slope frequency, $f(\tau)$, versus time, τ, main ramp,

$$f(\tau) = f_{00} + f'\tau. \qquad for \quad 0 \leq \tau \leq \tau_c \tag{26}$$

Here f_{00} is the initial frequency, f' is the slope and τ_c is the duration of the slope within the cycle.

The RF frequency is related to the extraction beam energy, T_{ex}, and the magnetic field profile, $B(\tau, T_{ex})$, as

$$f(\tau) = \frac{e}{2\pi m_0}\frac{B(\tau, T_{ex})}{\gamma(\tau, T_{ex})} \qquad and \tag{27}$$

$$\gamma(\tau, T_{ex}) = 1 + \frac{T(\tau, T_{ex})}{E_0} \tag{28}$$

where m_0 = 1.67262E-27 kg, e = 1.60218E-19 C.

Let us consider the baseline design, PN230-ab7a[10], in which the beam energy varies between 70 MeV and 230 MeV, the field profile (at the baseline 230 MeV) has B(r = 0) = 5.03 T and B(r = R_{ex}) = 4.64 T. The frequency varies between f_{max}=76.61 MHz (at r = 0, T_{ex} = 230 MeV) and f_{min} = 34.89 MHz (at r = R_{ex}, T_{ex} = 70 MeV). For this exercise we assume in (26) the duration and the initial frequency of the ramp τ_c = 1E-3 s and calculate f_{00} = f_{max} = 76.61 MHz and the slope, f' = -4.17E-4 MHz/s. This ramp is depicted in the diagram in Fig. 56.

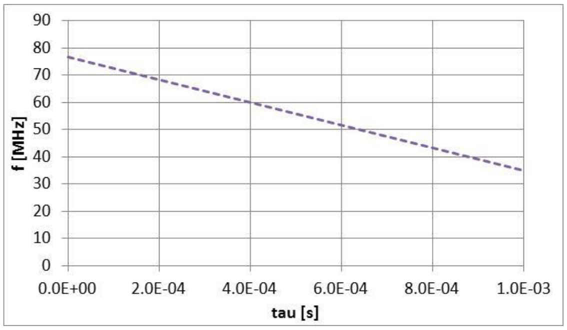

Fig. 56 Main constant-slope f(τ) ramp for PN230-ab7a model.

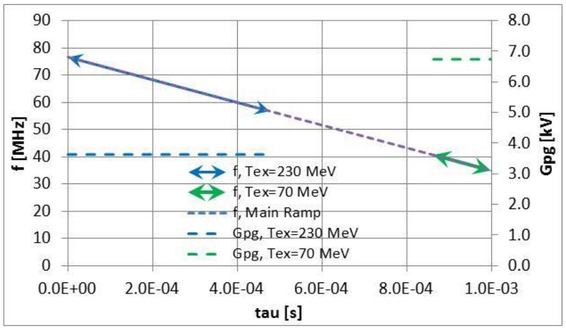

Fig. 57 Main and corresponding to T_{ex} = 70 MeV and 230 MeV f(τ) and G_{pg} ramps for PN230-ab7a model.

---

[10] Design PN230-ab7a preceded PN230-ab7am. They are very close; except for the present one is adjusted to use 2 circuits and an integer number of turns in the magnet windings.

This main ramp is designed to accommodate sub-ramps corresponding to the acceleration for any particular extraction energy, T_{ex}, in the given range, T_{min} = 70 MeV < T_{ex} < T_{max} = 230 MeV.

$$f(\tau) = f_{00} + f'\tau \tag{29}$$

for $\tau_0 \leq \tau \leq \tau_{ex} = \tau_0 + \tau_{of}$

Sub-ramps corresponding to these, extreme, extraction energies are depicted in Fig. 57.

The parameters of a sub-ramp are defined by the following sequence of equations:

Field-scaling coefficient,

$$k_b(T_{ex}) = \sqrt{\frac{T_{ex}\,(2E_0 + T_{ex}\,)}{T_{max}\,(2E_0 + T_{max}\,)}} \tag{30}$$

where E_0 = 938.27 MeV

Initial and final frequency,

$$f(\tau_0) = \frac{e}{2\pi m_0} k_b(T_{ex}) B(r = 0) \tag{31}$$

$$f(\tau_{ex}) = \frac{e}{2\pi m_0} \frac{k_b(T_{ex}) B(r = R_{ex})}{\gamma_{ex}} \tag{32}$$

Where $\gamma_{ex} = 1 + \frac{T_{ex}}{E_0}$

Start of ramp, τ_0, time of flight, τ_{of}, and end of ramp, τ_{ex},

$$\tau_0 = \frac{f_{max} - f(\tau_0)}{f'} \tag{33}$$

$$\tau_{of} = \frac{f(\tau_{ex}) - f(\tau_0)}{f'} \tag{34}$$

$$\tau_{ex} = \tau_0 + \tau_{of} \tag{35}$$

Number of turns,

$$N_t = f_{av}\tau_{of} \tag{36}$$

where $f_{av} = (f(\tau_0) + f(\tau_{ex}))/2$ is the average frequency.

Assuming that gain per turn, G_{pt}, is constant and number of gaps per turn is N_{gpt}, we can calculate corresponding gain per gap,

$$G_{pt} = \frac{T_{ex}}{N_{turns}} \tag{37}$$

$$and \qquad G_{pg} = \frac{G_{pt}}{N_{gpt}} \tag{38}$$

Table 16 shows the above parameters of the sub-ramps calculated as a function of T_{ex} in the given range. Gain per gap is calculated assuming 1 dee and 2 gaps per turn, N_{gpt} = 2.

Table 16 $f(\tau)$ vs T_{ex} ramp characteristics of sub-ramps as for PN230-ab7a model

T_{ex}	$k_b(T_{ex})$	$f(\tau_0)$	$f(\tau_{ex})$	f_{av}	τ_0	τ_{of}	τ_{ex}	N_t	G_{pt}	G_{pg}
MeV		MHz	MHz	MHz	s	s	s		kV	kV
70	0.530	40.63	34.89	37.76	8.62E-04	1.38E-04	1.00E-03	5194	13.5	6.7
80	0.568	43.54	37.03	40.29	7.93E-04	1.56E-04	9.49E-04	6294	12.7	6.4
90	0.604	46.30	38.99	42.65	7.26E-04	1.75E-04	9.02E-04	7476	12.0	6.0
100	0.639	48.93	40.81	44.87	6.63E-04	1.95E-04	8.58E-04	8739	11.4	5.7
110	0.672	51.45	42.50	46.97	6.03E-04	2.15E-04	8.18E-04	10081	10.9	5.5
120	0.703	53.87	44.08	48.98	5.45E-04	2.35E-04	7.80E-04	11499	10.4	5.2
130	0.734	56.21	45.56	50.89	4.89E-04	2.55E-04	7.44E-04	12992	10.0	5.0
140	0.763	58.48	46.96	52.72	4.35E-04	2.76E-04	7.11E-04	14558	9.6	4.8
150	0.792	60.68	48.28	54.48	3.82E-04	2.97E-04	6.79E-04	16196	9.3	4.6
160	0.820	62.83	49.53	56.18	3.30E-04	3.19E-04	6.49E-04	17904	8.9	4.5
170	0.847	64.92	50.72	57.82	2.80E-04	3.40E-04	6.21E-04	19680	8.6	4.3
180	0.874	66.97	51.85	59.41	2.31E-04	3.62E-04	5.94E-04	21524	8.4	4.2
190	0.900	68.97	52.93	60.95	1.83E-04	3.84E-04	5.68E-04	23433	8.1	4.1
200	0.926	70.93	53.95	62.44	1.36E-04	4.07E-04	5.43E-04	25407	7.9	3.9
210	0.951	72.86	54.94	63.90	9.00E-05	4.29E-04	5.19E-04	27444	7.7	3.8
220	0.976	74.75	55.88	65.31	4.46E-05	4.52E-04	4.97E-04	29543	7.4	3.7
230	1.000	76.61	56.78	66.70	0.00E+00	4.75E-04	4.75E-04	31703	7.3	3.6

Fig. 58 - Fig. 63 depict parameters of Table 16 shown as a function of the extraction beam energy.

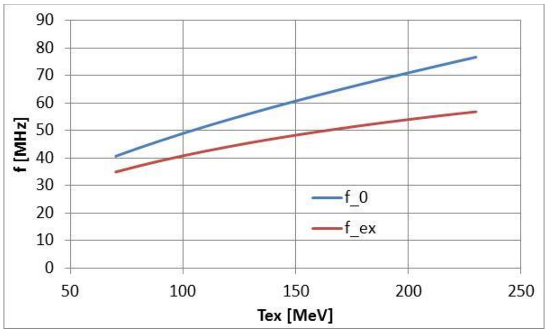

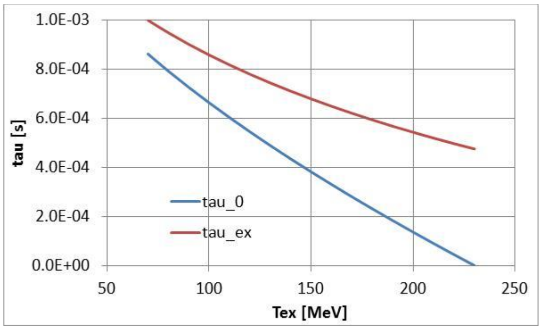

Fig. 58 Initial and final frequencies, f(τ_0) and f(τ_{ex}), of sub-ramps as a function of T_{ex}, PN230-ab7a model.

Fig. 59 Initial and final times, τ_0 and τ_{ex}, of sub-ramps as a function of T_{ex}, PN230-ab7a model.

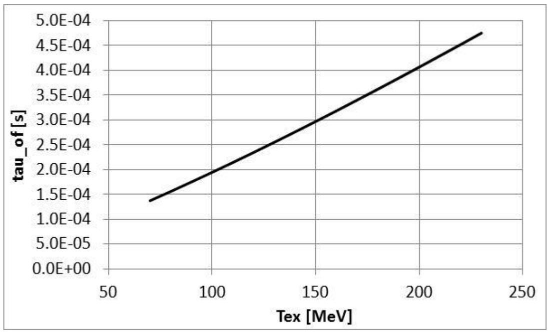

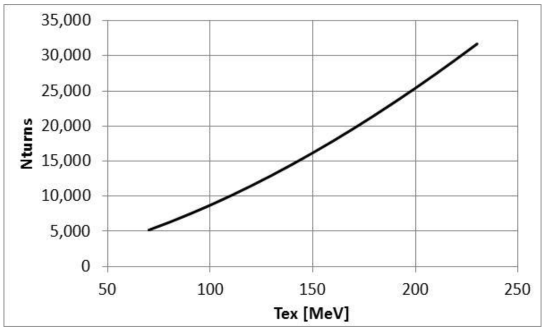

Fig. 60 Initial and final times, τ_0 and τ_{ex}, of sub-ramps as a function of T_{ex},, PN230-ab7a model.

Fig. 61 Number of turns, N_t, as a function of T_{ex}, PN230-ab7a model.

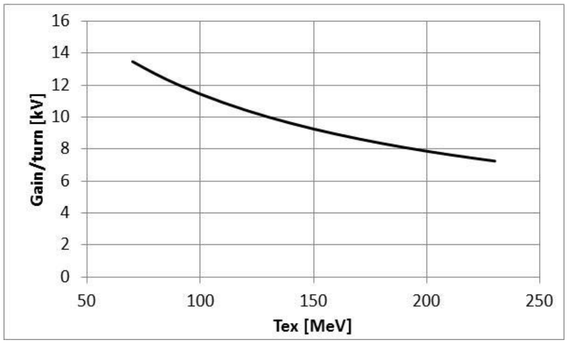

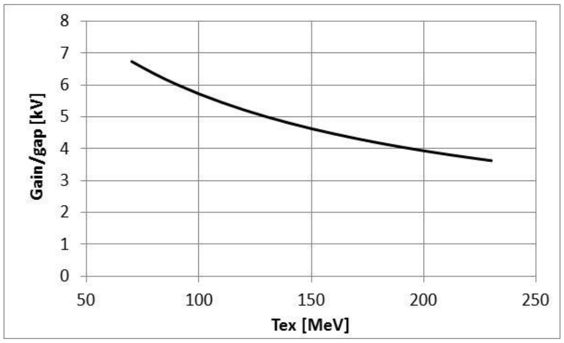

Fig. 62 Gain per turn, G_{pt}, as a function of T_{ex}, PN230-ab7a model.

Fig. 63 Gain per turn, G_{pg}, as a function of T_{ex}, PN230-ab7a model.

Note that the fundamental parameter defining the RF voltage is the duration of the ramp, τ_c, these data are calculated for τ_c = 1E-3 s. It yielded the maximum per-gap voltage of 6.7 kV. Would we reduce τ_c by a factor of 2, τ_c = 5E-4 s, the maximum per-gap voltage will double to 13.5 kV.

12.3.3 Beam Dynamics after Acceleration

Leaving the beam extraction method and apparatus temporary undefined let us assume that the particle is no longer accelerated by the RF system, resides at some fixed point in space and has an energy defined by the equations in Section 12.3.1. For the convenience, let us consider that this is an extraction point.

The particle comes to this point (at R_{ex}) with the following characteristics:

Extraction Energy: $T(R_{ex}, t)$

Extraction Mass: $m(R_{ex}, t) = m_0 * \gamma(R_{ex}, t)$,

where $\gamma(R_{ex}, t) = (1+T(R_{ex}, t)/ E_0)$

Extraction Velocity: $v(R_{ex}, t) = \omega(R_{ex}, t) * R_{ex} = K_b(t) * K_\omega(R_{ex}, t) * R_{ex} * \omega(r,0)$,

where $K_\omega(R_{ex}, t) = \gamma(R_{ex}, 0)/\gamma(R_{ex}, t)$

In the Field: $B(r, t) = K_b(t) * B(r, 0)$

It is clear right away that at this point the momentum,

$$p(R_{ex}, t) = m(R_{ex}, t) * v(R_{ex}, t) = K_b(t) * p(R_{ex}, 0),$$

where $p(R_{ex}, 0) = m_0 * \gamma(R_{ex}, 0) * R_{ex} * \omega(r, 0)$

scales the same way as $B(r, t)$, i.e. is proportional to $K_b(t)$.

Since in general terms

$$m * v * dv/dx \sim e * v * B \qquad \text{(here v is the particle velocity)}$$

then $(dv/dx)/v \sim (e*B)/(m*v) \sim (e * K_b * B_0)/(p_0 * K_b) \sim (e * B_0)/p_0$

and the shape of the trajectory is independent of the extraction beam energy.

Let us check it using VF Opera modeling. If the above theory is correct protons with properly scaled energy launched at the same spot into the properly scaled magnetic field shall be the same. Note that VF Opera Reference Manual claims that "the TRACK command calculates the trajectories of charged particles through the electric and/or magnetic fields (including full relativistic correction) …".

Table 17 shows "proper" (using formulas from Section 2.3.1) scaling of the magnetic field generated by scaling the current density in the COND file as a function of the beam extraction energy, $T(R_{ex}, t)$, scaled in two equal increments between T = 230 MeV to T = 70 MeV.

Table 17 Proper" Scaling of Beam Energy/Magnetic Field Modulation

$T(R_{ex}, t)/T(R_{ex}, 0)$	T	γ	Rigidity	B_{ex}	$K_b = B/B0$	J_{wp}
	MeV		T * m	T		A/cm^2
1.000	230.0	1.245	2.322	4.637	1.000	5200
0.652	202.2	1.215	2.162	4.318	0.931	4842
0.304	70.0	1.075	1.231	2.459	0.530	2757

Three models were analyzed, each having the same coil geometry but different coil current density corresponding to $T(R_{ex}, t)/T(R_{ex} (0) = 1.0$, 0.652 and 0.304. The proton was launched in the circumferential direction from the same spot in the mid-plane at R_{ex} = 50.1 cm with the respective energy $T(R_{ex}, t)$. Fig. 64 and Fig. 65 show the trajectories of the proton in the axial and lateral perspectives. They all form perfectly coincident circles and lie in the same plane.

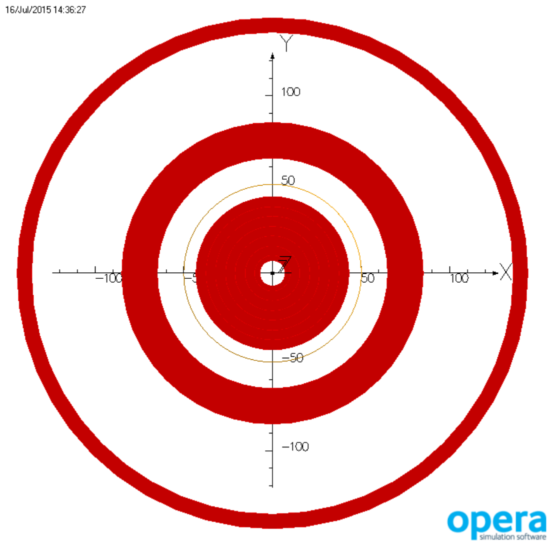

Fig. 64 Proton Trajectory at 3 Energies in a Scaled Field, Top View.

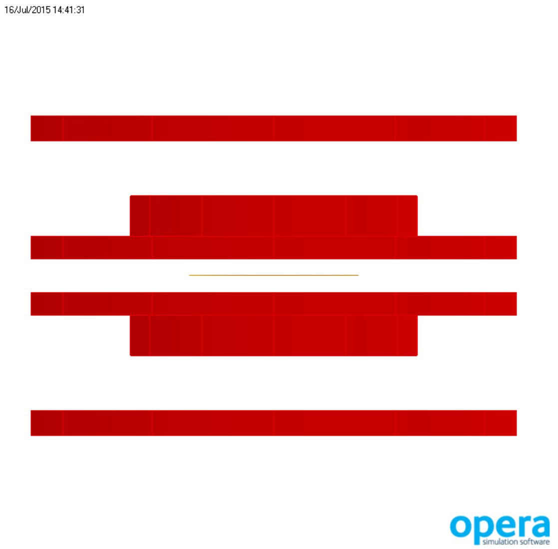

Fig. 65 Proton Trajectory at 3 Energies in a Scaled Field, Side View.

This numerical experiment confirms the above conclusion that for a properly scaled coil current matching the scaled beam energy the trajectories of the particle are the same.

This feature opens the opportunity of using regenerative extraction by magnetic bumps generated by small coils with the current scaled by the same proportion as in the Main/Shaping/Shielding coils.

13 Beam Dynamics in the Ironless Cyclotron

13.1 Introduction

13.1.1 Choice of Ion

Typically, synchrocyclotrons are operated with an internal ion source, producing either H^- or protons. For a compact, high-field machine like this design represents, the usage of H^- is not feasible, because of Lorentz stripping. This effect occurs in high fields at moderate to high energies, where – due to relativistic effects – the magnetic field of the cyclotron is partially seen as an electric field by the ion. This electric field, if strong enough can lead to a stripping off of the only very weakly bound (~0.75 eV) valence electron, thereby creating a neutral atom that would no longer follow the design path determined by the magnetic field. The process is detailed in [27] and [28]. Even for a moderate field of 1 T, Fig. 66 shows that 50% of an H^- beam would be lost when accelerated to 225 MeV. This is far below the desired maximum field strength of 4.9 T for this compact machine. Protons are thus the ion of choice for the beam dynamics studies.

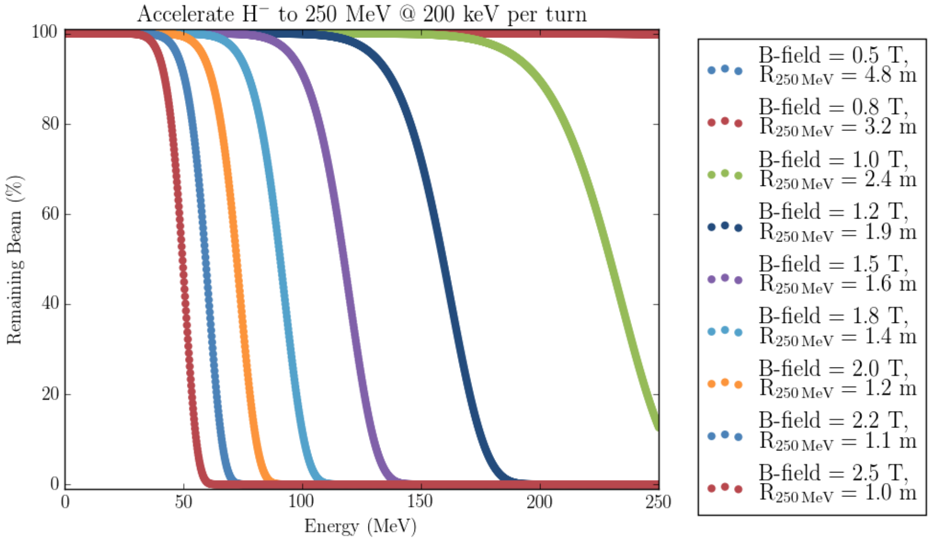

Fig. 66: Remaining beam as function of magnetic field strengths at 200 keV energy gain per turn. For 1 T average field (green curve), the 50% loss limit lies at ~225 MeV.

13.1.2 Different Acceleration Schemes and Test Cases

As was discussed briefly in Section 6 (Basic Magnet Design) and in more detail in Section 12 (Variable Beam Energy), in a synchrocyclotron, the magnet is weakly focusing (radially decreasing field), and the frequency has to be adjusted as a function of radius (i.e. time of flight of the ions) in order to compensate for relativistic mass increase, which would otherwise lead to phase-slip. In previous compact synchrocyclotrons (e.g. IBA's S2C2 [29]–[31]), a RotCo is used to generate a frequency-versus-time profile that exactly matches the required synchronous frequency at each orbit radius and corresponding energy.

In order to smoothly adjust the final beam energy, one can reduce the magnetic field strength. The dee voltage and RF frequency have to be adjusted accordingly. As was discussed in Section 12, for the present design, two options have been investigated: a) Scaling the non-linear frequency profile exactly to the needs of the scaled field to achieve, in principle, the same number of turns and identical particle trajectories. b) A linear frequency profile. Table 18 lists the corresponding study parameters.

Table 18 The Most Important Parmaters for the 6 Beam Dynamcis Test Cases

Parameter	Case 1a	Case 2a	Case 3a	Case 1b	Case 2b	Case 3b
Final Energy [MeV]	70	150	230	70	150	230
B (center) [T]	2.64	3.94	4.98	2.64	3.94	4.98
B (extraction) [T]	2.44	3.64	4.60	2.44	3.64	4.60
f_{RF} (start) [MHz]	40.26	60.13	75.91	40.26	60.13	75.91
f_{RF} (end) [MHz]	34.58	47.86	56.28	34.58	47.86	56.28
f_{RF} slope [MHz/µs]	non-linear	non-linear	non-linear	-5.64e-2	-5.64e-2	-5.64e-2
Turns	~25000	~25000	~25000	3764	11745	23000
V_{dee} peak [kV]	2.8	6.3	10.00	18.6	12.77	10.00

"a" denotes non-linear frequency ramp, "b" the proposed alternative linear frequency ramp. A slope was chosen here that keeps the dee voltage at 10 kV for the nominal case of 230 MeV final beam energy.

13.2 Central Region

With the high magnetic field requirement and the typically low injection energy in a synchrocyclotron, the orbit radius of the first turn is small, which puts a stringent upper limit on the size of the ion source and central region elements. An example for a high-field, compact synchrocyclotron that performs well is IBA's S2C2. The proton radius of the first turn in the S2C2 is about 2.5 mm [26]. This extremely small. Nevertheless, a cold-cathode PIG type ion source this small is still able to reliably produce more than 6 mA of DC beam current. The source can be pulsed to only deliver beam at the beginning of the acceleration cycle. However, during each RF period, beam is extracted and accelerated at unfavorable phases in addition to the design phase. Posts can be used to block the paths of these particles. A process often called phase-selection. Fig. 67 shows a 3D CAD rendering of the preliminary design of the central region for the ironless cyclotron with phase-selection posts. Similar to the S2C2, the central region is envisioned to be removable separately from the dees for easy alignment and maintenance. In addition, biasing the whole central region to 1-2 kV can help with multipacting.

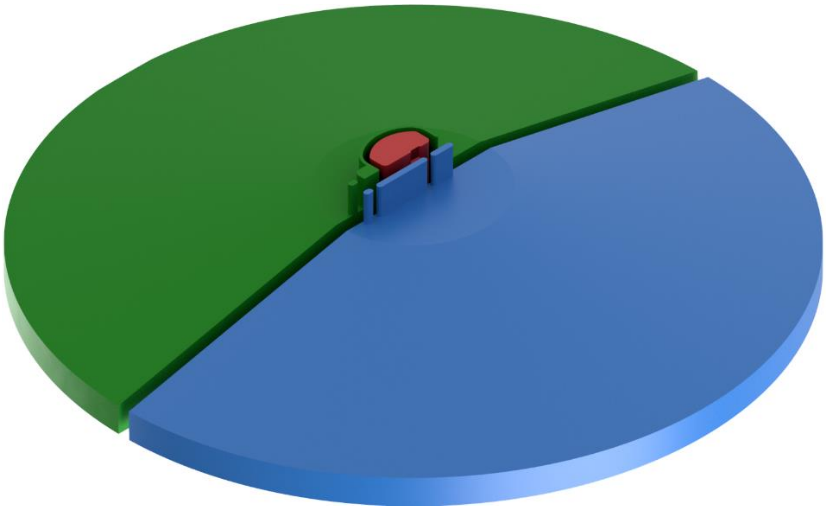

Fig. 67: 3D CAD rendering of the bottom half of the central region. The ion source (red) can be biased up to -15 kV to adjust the radius of the first turn. The beam is shielded from this field by an enclosure on the dummy-dee (green). The dee (blue) has additional pillars for phase selection.

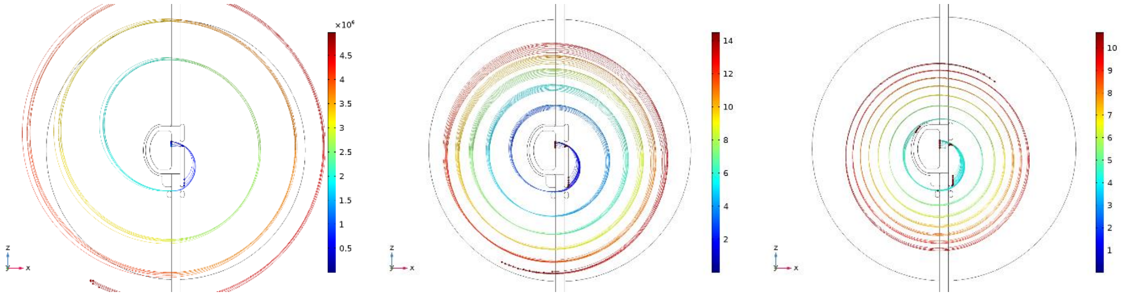

Fig. 68: Test cases 1b, 2b, 3b (from left to right). Test cases 1a, 2a, 3a are identical to the image on the right. Ions are started from a single point in the center of the ion source opening. 100 ions are tracked, each starting at a different time, filling one RF period, to see the phase selection. The ion source negative bias is increased to compensate for the reduced magnetic field and increased dee voltage. This keeps the first half-turn at the same radius, yielding the desired phase selection effect.

Simulations of the beam dynamics from the source to 100 ns of acceleration were performed with the Multiphysics Software COMSOL® [32] to show the feasibility of the design. Space charge was neglected for the time being and the magnetic field was assumed constant at B (center) during these studies. These are valid assumptions given the small radius of the central region (constant B-field) and the small beam currents required for patient treatment. Fig. 68, right shows the first 100 ns of acceleration for a beam with 230 MeV final energy (case 3a/3b). As cases 1a and 2a use a “collinear” approach, where frequency and dee voltage are scaled to reproduce the same particle trajectories at lower B fields, they look identical to 3a. However, in cases 1b and 2b, the dee voltage actually goes up with reduced magnetic field (to keep the slope of the frequency ramp constant as described in Section 12) and the phase selection during the first half-turn would not happen. By negatively biasing the source body to -15.35 kV and -6.3 kV, for 70 MeV and 150 MeV final energy, respectively (cases 1b and 2b), the particles are forced on a similar orbit before experiencing the full acceleration as can be seen in Fig. 68 left and middle. The higher the source bias, the smaller the selected phase window, which is trivially explained by the fact that the phase window with electric field pointing in x-direction shrinks from 180 degrees (0 kV on source) to 68 degrees (-15.35 kV on source). Note: This is not considering transit time factors (TTF), so the actual phase window is smaller still. Since the phase window selected using the posts is about 30 degrees, this is not a problem. Effects of the negative source bias on the plasma inside the source have to be investigated further and tested experimentally. At this point, we have not seen any showstoppers with respect to smooth energy scaling stemming from the ion source and central region design perspective.

13.3 Acceleration

After clearing the central region, the particles need to undergo acceleration to reach the required extraction energy. The six test cases were used as representative cases for smooth energy scaling, spot checks with other energies were performed that showed no deviation from the presented results. In Section 12, some preliminary single-particle tracking was presented that was performed with the FEA code OPERA [33] these were repeated for all six test cases using the well-established Particle-in-Cell code OPAL [34]. For this purpose, a simple dee – dummy dee assembly was created (see Fig. 69) the electric field was calculated in OPERA, saved in a file and loaded as external RF field in OPAL. As a preliminary step, the static equilibrium orbits for the magnetic field map were calculated and the resulting tunes at discrete radii were compared to the tunes obtained from OPAL’s tune-finder (see Fig. 70).

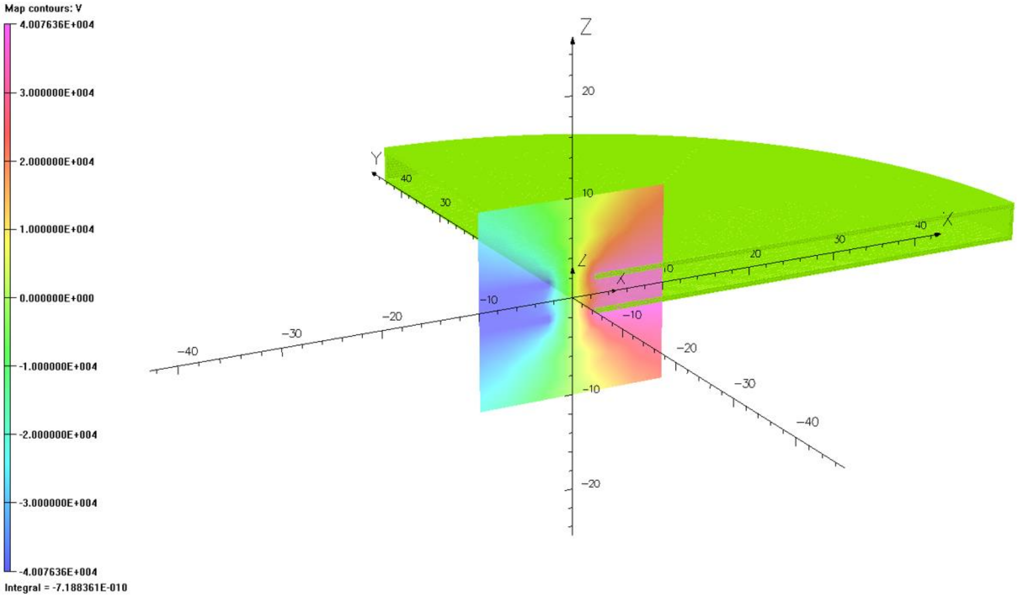

Fig. 69: Simple OPERA model of a dee (dummy dee not shown and model cut in half for symmetry) with the resulting potential map in the center. The field can be scaled linearly for the different cases.

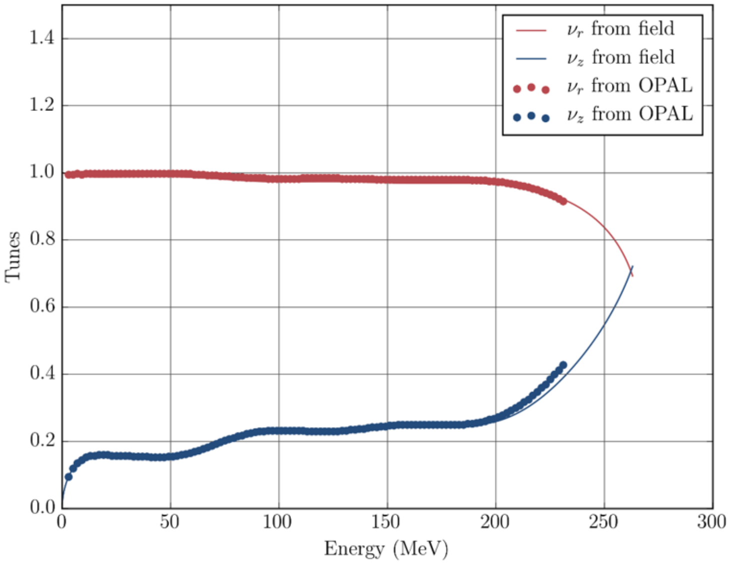

Fig. 70: Tunes from static equilibrium orbit calculations in OPAL (dots) compared to the theoretical values calculated directly from the magnetic field (solid lines). Good agreement can be seen.

As expected, good agreement was found between OPERA single-particle tracking and OPAL single-particle tracking. Furthermore, the multiparticle tracking with OPAL yielded similar results when comparing the beam centroid position to the single-particle tracking. As an example, the energy gain versus time and centroid radial position versus time are plotted in Fig. 71.

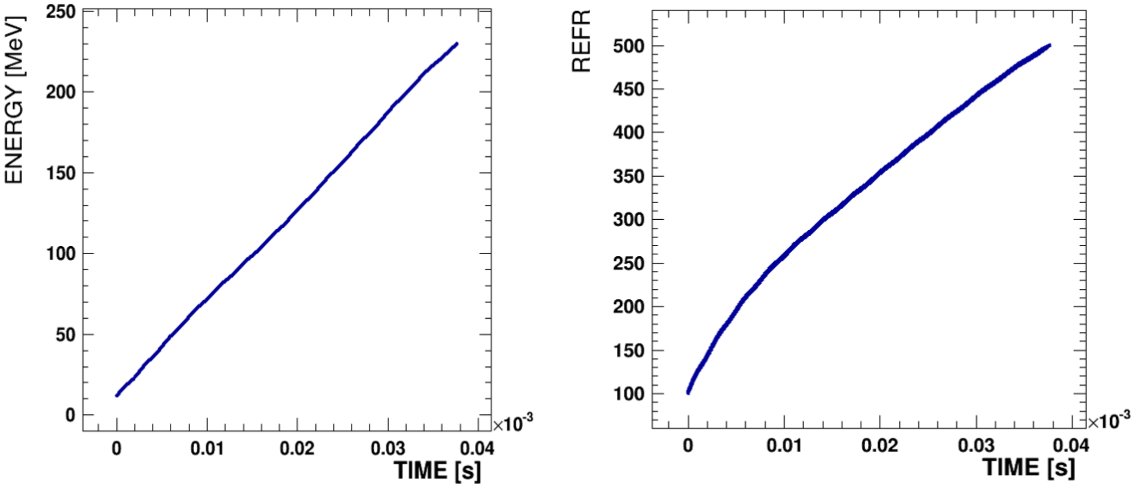

Fig. 71*: Energy and beam centroid radial position versus time for a 10000-particle simulation using OPAL. This is the 230 MeV case, which is representative for all cases.*

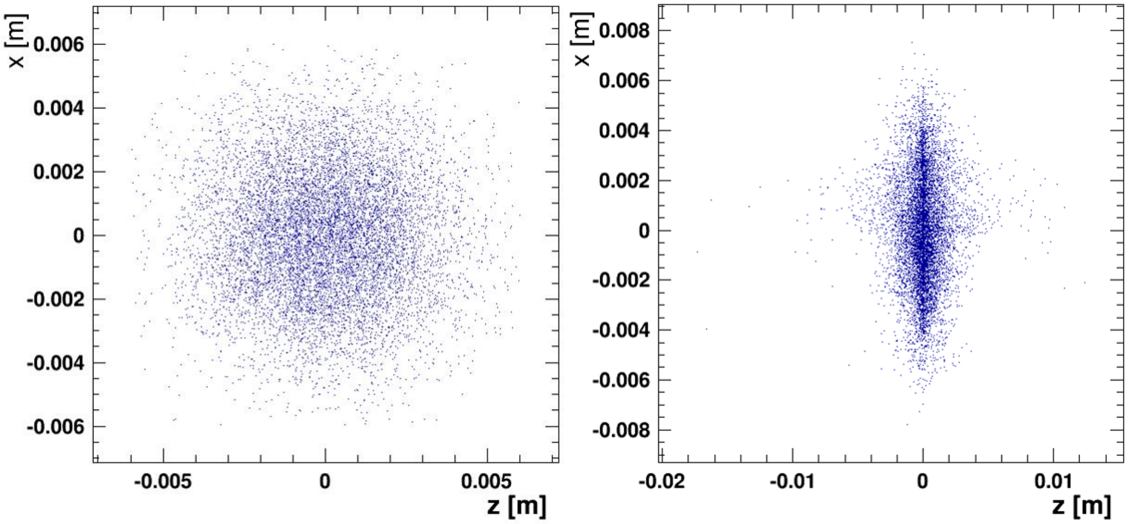

Fig. 72*: 2D projection of the starting bunch (left) and final bunch at 230 MeV (right) corresponding to* **Fig. 71***. The beam is initialized as a Gaussian sphere at R = 10 cm. Later simulations were re-run with a starting position of 5 cm, yielding similar results. Z denotes the vertical direction, x is aligned such that it corresponds to the radial direction.*

Starting with a spherical Gaussian beam of σ = 2 mm, the beam grows negligibly in vertical direction and mildly to just under 3 mm RMS-radius in radial direction for all test energies. A 2D projection of the bunch at the start and the end of the 230 MeV simulation can be seen in Fig. 72. It should be noted that the more realistic particle distributions obtained from the central region simulations were not used as the input for the acceleration simulations, due to time constraints in the present study.

13.4 Extraction

To cleanly extract beam with minimal energy spread, a septum is typically used to peel off the last turn and guide the particles into an extraction channel. In order to do this without losses and activation of the septum, a resonance is excited, that leads to a large turn separation at the highest energies.

13.4.1 Regenerative Extraction

Based on an idea by Teng and Tuck [35], LeCouteur proposed a rigorous mathematical treatment of the particle dynamics in a "peeler-regenerator" system for extraction from a synchrocyclotron, or more simply "regenerative extraction system" [36]. This was later reviewed and expanded on by others [37]. The basic idea of regenerative extraction is to lock in the radial tune $\nu_r = 1$ by means of a second order perturbation in the magnetic field. Thus this is often called a $\nu_r = 2/2$ resonance. The second order perturbation is a "regenerator" field which linearly increases with radius r starting at a radius $r_{0,r}$ and a correspondingly decreasing "peeler" field that linearly decreases with r starting at a radius $r_{0,p}$. The two perturbations sit at angles θ_r and θ_p and have azimuthal extent $\Delta\theta_r$ and $\Delta\theta_p$, respectively. As described in the references above, the equations of motion of a particle inside the radial extent of both peeler and regenerator can be linearized and described by transfer matrices. In the main field of the cyclotron, each particle energy is associated with an equilibrium orbit radius r_{eq}. We can then define x and x' as the radial excursion from the equilibrium orbit, and the angle with the tangent to the equilibrium orbit, respectively. Similarly, we define z and z' as the excursion from the cyclotron median plane, and the angle of the particle momentum vector with the median plane. The particle transformation for traveling an angle α in azimuthal direction is then given by:

$$\begin{bmatrix} x \\ x' \end{bmatrix} = M_{T,r}(\alpha) \cdot \begin{bmatrix} x_0 \\ x_0{}' \end{bmatrix}$$

$$\begin{bmatrix} z \\ z' \end{bmatrix} = M_{T,z}(\alpha) \cdot \begin{bmatrix} z_0 \\ z_0{}' \end{bmatrix}$$

where $M_{T,r/z}(\alpha)$ are the transfer matrices for radial and vertical motion. For motion in the main field without acceleration or perturbations, they take this form:

$$M_{T,r/z}(\alpha) = \begin{bmatrix} \cos(\nu_{r,z}\alpha) & \dfrac{1}{\nu_{r,z}}\sin(\nu_{r,z}\alpha) \\ -\nu_{r,z} \cdot \sin(\nu_{r,z}\alpha) & \cos(\nu_{r,z}\alpha) \end{bmatrix}$$

with ν_r and ν_z the tunes of the cyclotron defined as:

$$\nu_r = \sqrt{1-n}$$

$$\nu_z = \sqrt{n}$$

$$n = -\frac{dB}{dr}\frac{r}{B}$$

Where n is called the *field index* of the main field. The *action* of the regenerator and the peeler on the beam can be described as a *thin lens*, where the angles x' are changed, but not the position x. The corresponding transfer matrices are:

$$P(Q_j) = \begin{bmatrix} 1 & 0 \\ -Q_j & 1 \end{bmatrix}$$

where j denotes the jth perturbation and Q_j is defined as follows:

$$Q_j = -n_j \Delta\theta_j = \frac{dB}{dr}\frac{\rho}{B_0}\Delta\theta_j$$

with $\Delta\theta_j$ the angular width of the perturbation (as defined above) and $\frac{dB}{dr}$ positive for a regenerator and negative for a peeler. For a full turn (2π) in this system, starting at the center of the peeler, the full transfer can then be written as:

$$\begin{bmatrix} x \\ x' \end{bmatrix} = M_T(2\pi) \cdot \begin{bmatrix} x_0 \\ {x_0}' \end{bmatrix} = M_{T,r}(\beta) \cdot R(\Delta\theta_r) \cdot M_{T,r}(\alpha) \cdot P(\Delta\theta_p) \cdot \begin{bmatrix} x_0 \\ {x_0}' \end{bmatrix}$$

where α the angle between peeler and regenerator and β = 2π – α. The stability requirement is

$$\text{Trace } M_T(2\pi) < 2$$

that is, for the radial motion, in order to excite a resonance, we want the trace of the full-turn-transfer-matrix to be larger than 2. However, at the same time, in order to be able to extract the beam, we require vertical stability and thus a trace smaller than two for z motion.

In reality, it is not always necessary to have a peeler, the natural falloff of the main magnetic field can provide this action, and only a regenerator is placed to bend the particles back towards the center. This process can be seen in Fig. 73.

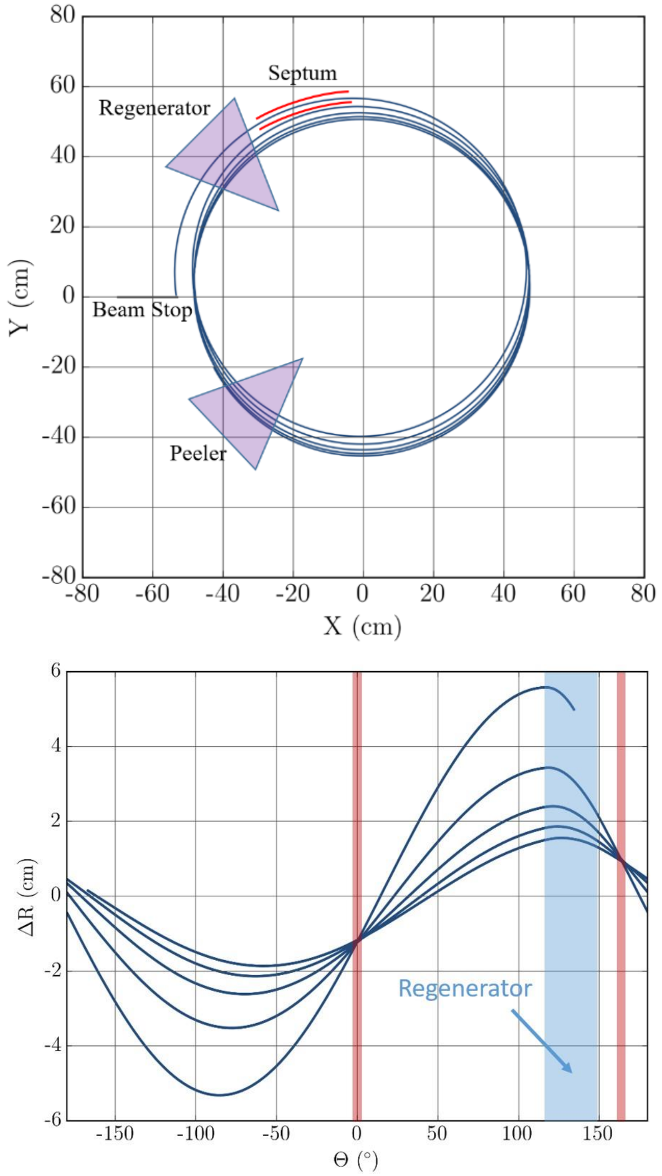

Fig. 73*: Particle tracking results using OPAL* [34]*, demonstrating the peeler-regenerator process. Upper: the final 5 orbits in the synchrocyclotron equipped with a regenerator and (optional) peeler at 135 degrees and 225 degrees, respectively. Lower: orbit excursion from the equilibrium orbit versus azimuthal position. The nodes are indicated in red and the regenerator position in blue. It can be seen how the regenerator bends the trajectories back to go through the node. The resonance is "locked in". Note that the net result is that the center of the particle orbit "walks" in the y-direction, but remains fixed in the x direction, until the particle is extracted.*

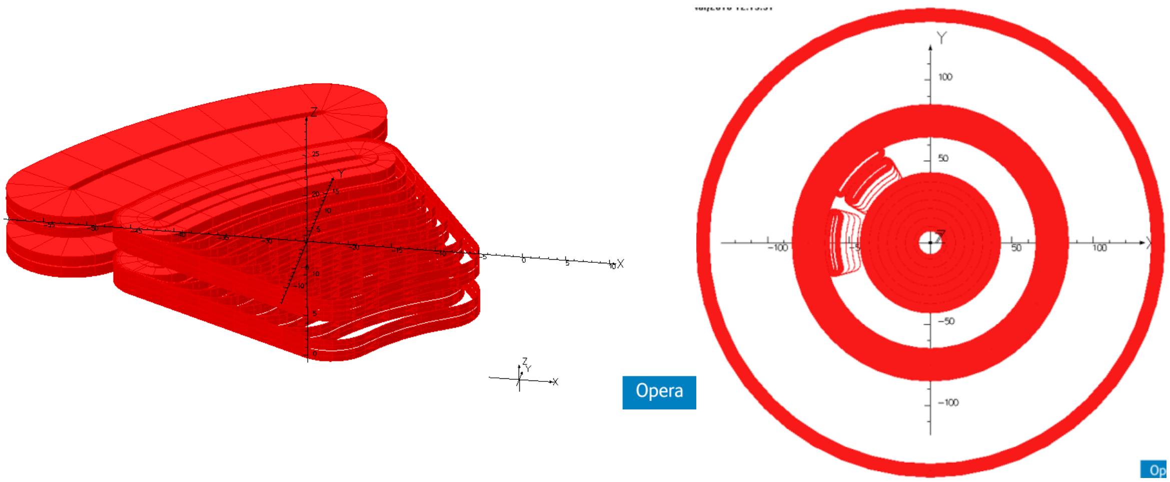

Fig. 74*: Left: 3D isometric view of a fringe-field compensated regenerator coil. Right: Example placement of a regenerator and a peeler coil among the main field coils.*

13.4.2 Peeler and Regenerator Coils

The design of the iron-free regenerator and (where applicable) peeler coils is driven by two basic principles:

1. All coils need to be iron-free. This is necessary to provide the smooth scalability of the fields with desired final energy, as explained earlier.
2. The coils within one system (e.g. the "regenerator") must be driven by the same power supply, hence the current density for each coil must be the same and the actual currents generating the magnetic field components are determined by the cross-sectional area of the individual coils (i.e. number of windings).

Item 1, the main premise of this project, leads to fringe fields that can extend deep into the inner regions of the cyclotron, as there are no iron poles to shape the fields and contain the return flux. These fringe fields need to be minimized as to not excite resonances earlier during the acceleration process in the cyclotron. We have devised a scheme to reduce the fringe fields by placing a single large compensation coil on the outside and a number of smaller compensation coils around the main coil as can be seen in Fig. 74.

13.4.2.1 Matrix Tracking and Coil Optimization in python

Based on the formalism described above, a simple matrix tracker was developed in python 3 [38] that takes the finite extent of the peeler and regenerator in radial direction into account. The transfer matrices can be subdivided into a product of matrices with smaller angles (the *step-size*) and applied subsequently. In addition, at each step, it can be checked, whether the angular position of an accelerating gap has been crossed and if so, the equilibrium orbit radius r_{eq} can be increased accordingly. Regenerator and peeler action are only applied if $r_{eq} + x \geq r_{0,j}$ where $r_{0,j}$ is the starting radius of the perturbation. This tracker has an optimization routine as well that helps designing the regenerator field.

The python script then takes the solution and builds compensated coils that can be loaded into OPERA. The *Scipy* optimizing routines are used to minimize the fringe fields. Examples can be seen in Fig. 75.

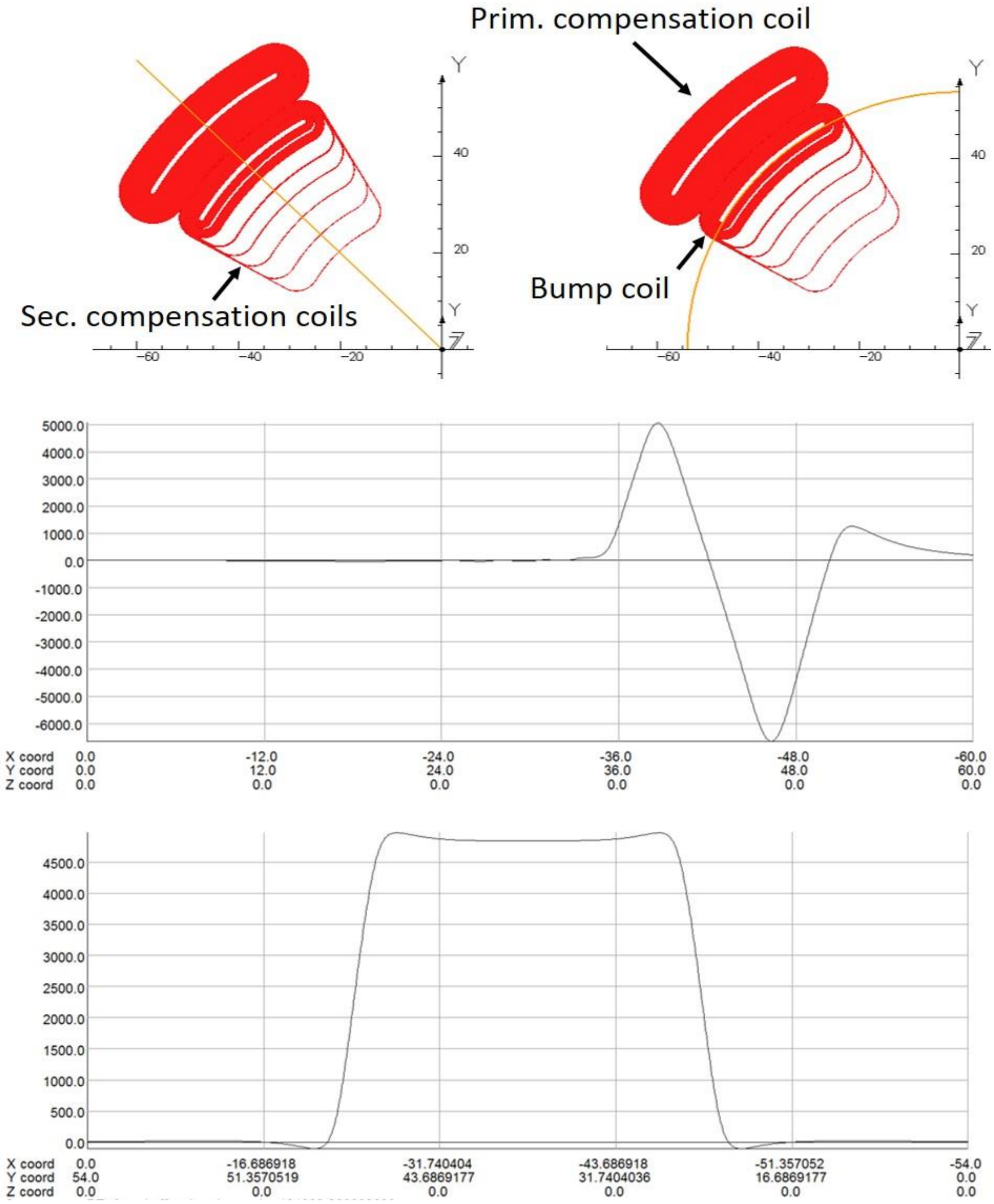

Fig. 75*: Top: view of an example regenerator coil with main bump coil, primary compensation coil and secondary compensation coils. The fields along the golden lines (top field plot – radial, bottom field plot – azimuthal). X, Y, Z coordinates (horizontal axes) in cm, fields*

(vertical axes) in Gauss. It can be seen that there is only a small residual fringe field outside of the coil area, and a sharp drop radially outside the bump that the beam will not see.

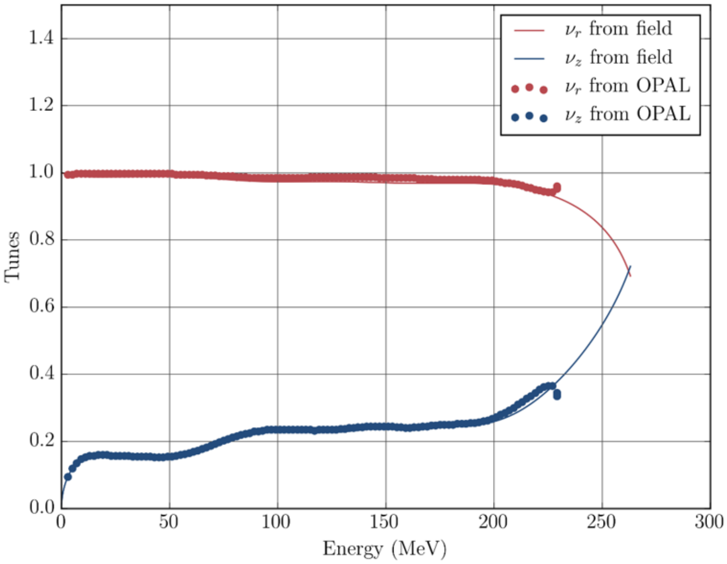

Fig. 76*: As a first step, the tunes are recalculated in the modified magnetic field. The effect of the regenerator coil together with the peeler action of the main field fall-off can be seen in the sharp rise/drop of the tunes at ~230 MeV. This is the "locking in" of the resonance.*

13.4.3 Particle Tracking in the Modified Magnetic Field

Single- and multi-particle tracking was performed in both OPERA and OPAL to show the feasibility of regenerative extraction in the completely iron-free system. Coils were prepared in the way described above and magnetic fields were calculated in OPERA, saved, and loaded into OPAL. Both regenerator and (optional) peeler are described by the following parameters:

- azimuthal position $\theta_{r/p}$
- azimuthal width $\Delta\theta_{r/p}$
- starting radius $r_{0,\,r/p}$
- field gradient $dB_{r/p}/dr$

In addition, we can choose the maximum current density and the number of compensation coils. A typical scenario that was used often in the presented studies is a regenerator at $\theta_r = 135°$ with $\Delta\theta_r = 30°$, and either the natural falloff of the main field as peeler or a discrete peeler at $\theta_r = 225°$ (see also Fig. 73). As a preliminary test, the tune calculation in OPAL was used to see the differences in the tunes compared to just the main field (see Fig. 76). The moment of resonance lock-in can be seen at the end, where the tunes exhibit the onset of a singularity.

13.4.3.1 Single Particle Tracking Results

All six cases showed the expected behavior of rapidly increasing turn separation in the last few turns before extraction. Particle trajectories (x/y) overlaid with a contour plot of the magnetic fields as well as R (cm) vs. time and E_{kin} (MeV) vs. time for cases 1a, 2a, and 3a are plotted in Fig. 77. These are representative for all six cases.

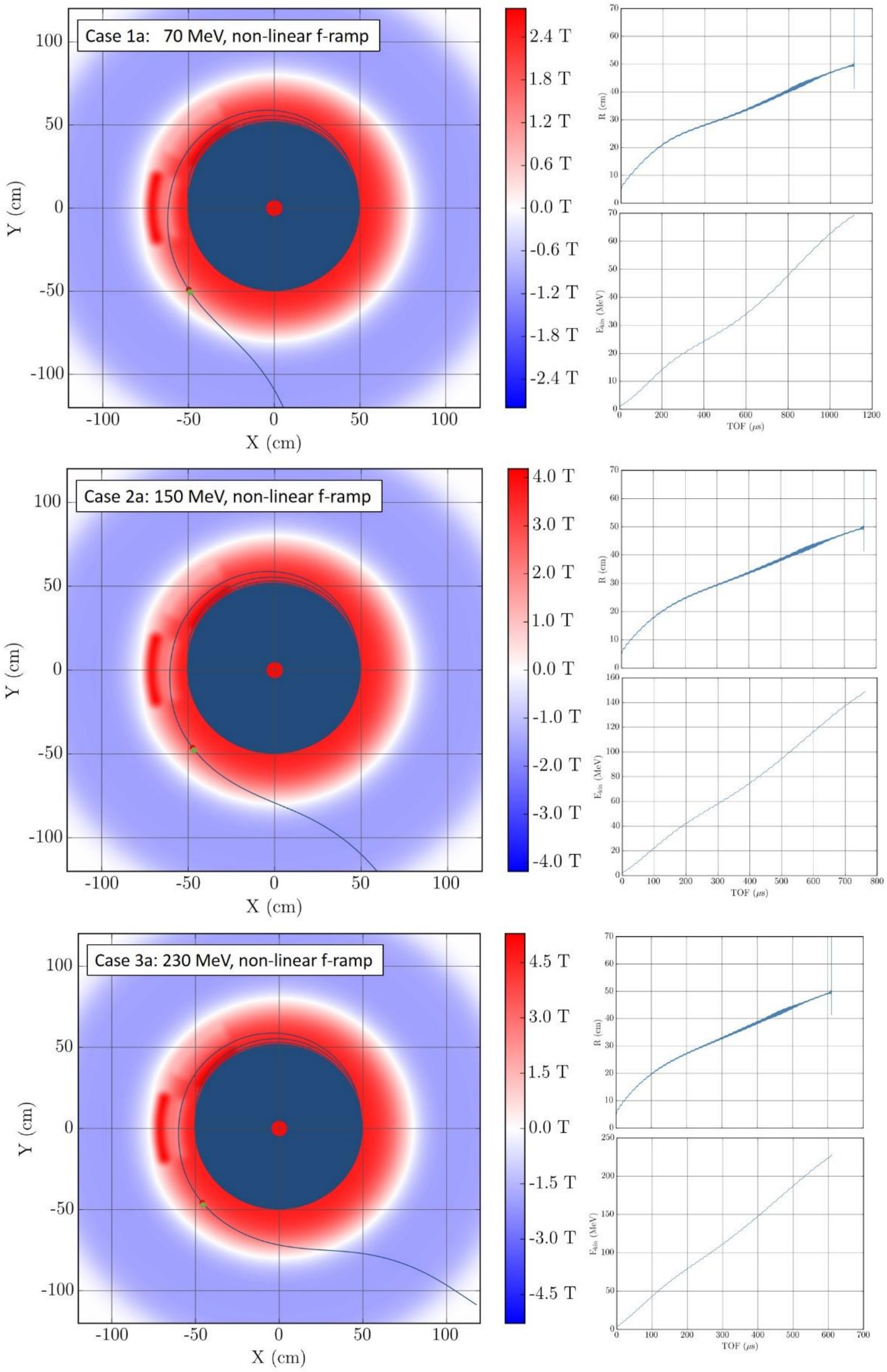

Fig. 77***: Single particle tracking results for regenerative extraction using only a regenerator (centered at a 135° azimuth). A modified peeler (centered at a 180° azimuth) is used as magnetic***

septum. The final trajectory (starting at the green dot) can be corrected using additional steering elements and changing the magnetic septum strength.

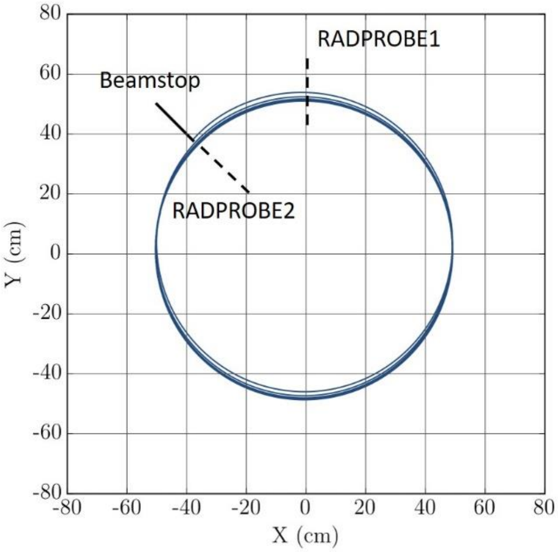

Fig. 78*: Case 3b with 10k particles. Positions of various probes for analysis are indicated. The regenerator is located where "Beamstop" and "Radial Probe 2" are. No peeler was used. The turn separation increases moderately in this preliminary simulation.*

13.4.3.2 Multi-particle Tracking Results

Multi-particle tracking with upwards of 5000 particles from the center using realistic dee voltages (5-10 kV) is very computationally intensive due to the ~20000 turns. To alleviate this, a small number of simulations were performed for the full cyclotron as a baseline and subsequently, the beam was started R = 45 cm, using 10000 particles per simulation. Comparing the final turns of the full simulations with the ones starting at 45 cm, negligible influence of the fringe fields pertaining to the extraction scheme were found.

For this preliminary study, cases 1b, 2b, and 3b were chosen for multi-particle tracking with regenerator and no peeler or septum. The x-y plot of the final turns of case 3b is shown in Fig. 78and the corresponding particle number and energy histograms of the beam passing through the Radial Probe 2 can be seen in Fig. 79 for all three test cases. A clear effect of the regenerative extraction system can be seen, albeit not yet at the level needed for clean extraction. The energy spread in the "extracted" beam is very good (at the 0.03% level), however, this is likely to increase when the more realistic beams from the central region design study are used.

Finally, in order to increase the turn separation and test, whether beam can be split off using a septum, a peeler was added back at 225° and an electrostatic septum was placed from 100° to 125°. Significantly increased turn separation was observed without compromising the small energy spread. The corresponding plots are shown in Fig. 80 (orbits and radial orbit excursion) and Fig. 81 (histogram of particle number density in radial direction). This simulation was only performed for 230 MeV final beam energy and linear frequency scaling (case 3b) so far.

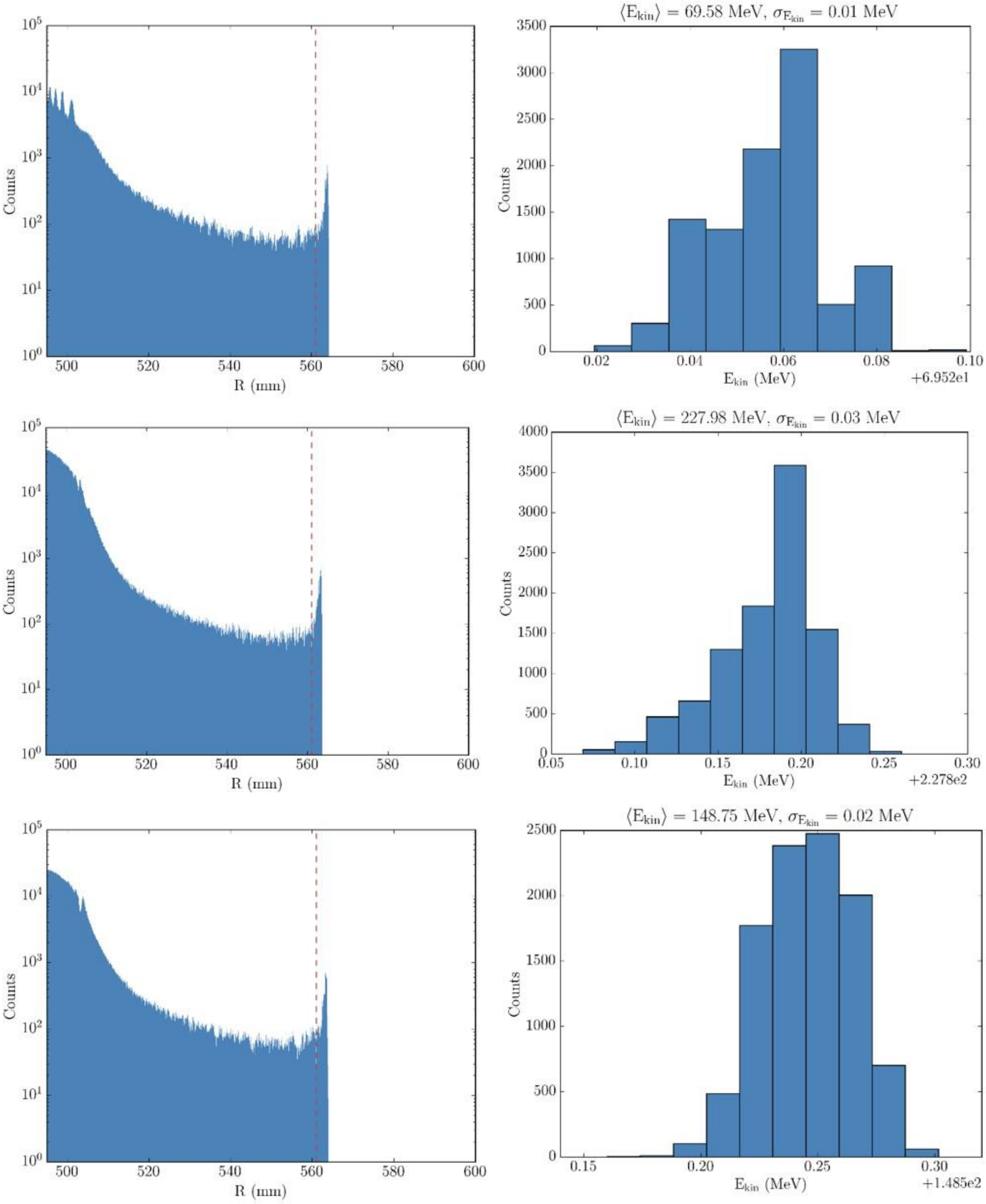

Fig. 79*: Left:* Histogram of the radial positions of the particles on a probe located at 180°. Right: histogram of particle energies in the peak at the end of acceleration. This peak can be

split off using a septum and represents the extracted beam. The plots show excellent scaling of beam dynamics with final energy, however more tuning of the peeler regenerator system is required to increase the turn separation in multi-particle simulations.

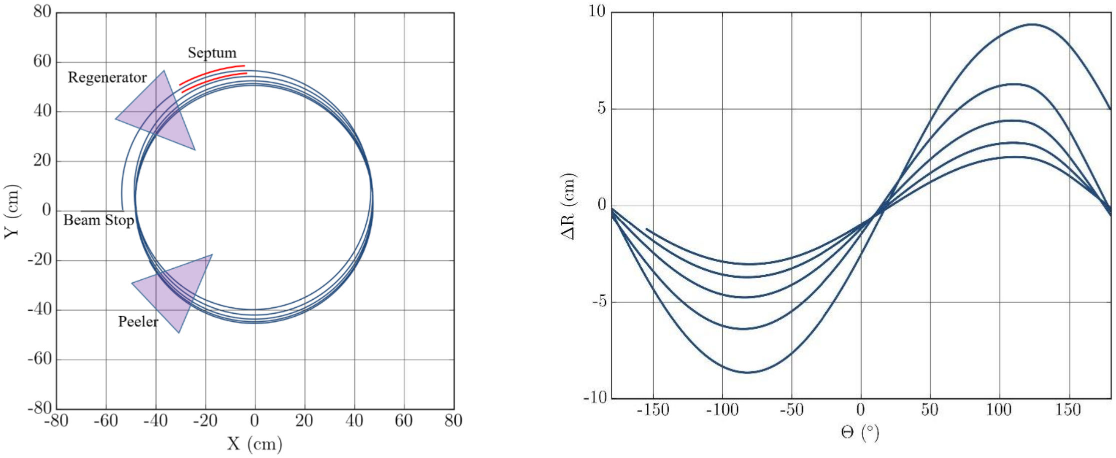

Fig. 80*: Left: the final 5 orbits in the synchrocyclotron equipped with a regenerator and peeler at 135° and 225°, respectively. Right: orbit excursion from the equilibrium orbit versus azimuthal position.*

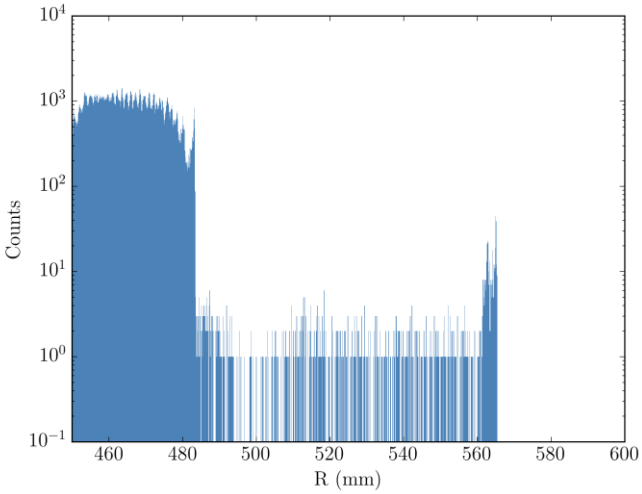

Fig. 81*: Histogram of the radial positions of the particles on a probe located at 180°. The peak at the end has σ_r ~ 1.5 mm and σ_z ~ 0.4 mm. The energy spread at this point is around 0.03%. This result corresponds to the trajectories plotted in* **Fig. 80***.*

13.5 Beam Dynamics Conclusions

The three main aspects (injection, acceleration, extraction) have been investigated for the ironless cyclotron concept. As one of the envisioned benefits of an ironless approach is smooth scaling of the final energy by adjusting the magnetic field strength, great care was taken not to introduce any magnetic materials (e.g. iron poles) to shape fields. Instead, all designs made use of superconducting coils and copper electrodes only. Furthermore, all simulations were tested with three different final energies (70 MeV, 150 MeV, 230 MeV) and two ways of adjusting the RF frequency over time (linear, non-linear), yielding a total of 6 test cases. A feasible central region design was presented that allows phase selection for all 6 test-cases. Acceleration of the beams was extensively simulated and no issues with either linear or non-linear frequency scaling are foreseen. Finally, different types of peeler-regenerator setups for regenerative extraction have been tested, making use of iron-free fringe-field compensated superconducting coils. It could be shown that the required resonance can be excited for all cases. While a final design will require further optimization of all beam shaping elements except the main field coils, we have demonstrated the feasibility of this approach and did not find any show-stoppers.

14 Power System Design for Variable Beam Energy

The desire to have a variable beam energy during the clinical treatment cycle imposes a new design burden on the power supply for the superconducting cyclotron magnet. Superconducting magnets typically have very low circuit resistance because the magnet itself is superconducting, with minor resistances in the current bus from the power supply to the cryostat and the high temperature end of the magnet current leads. Thus, a high current, low voltage (~10 V) power supply is usually sufficient for charging/discharging the magnet and maintaining a steady operating current. Variable beam energy in our concept, however, requires rapid charging and discharging of the superconducting magnet. This creates ac losses in superconducting windings, and requires a rather large inductive voltage to generate rapid magnetic field, and thus energy variation. The problem of ac losses has been shown to be not of major concern as demonstrated by the calculations in section 12.2. The need for high inductive voltage however can have a significant impact on the power system design. There are however, feasible existing technology power technology solutions as noted in the following sections.

14.1 Power System Concerns

The most desirable mode of operation requires high pulsed power for rapid transition between energy levels – “picket fencing” (Fig. 82). Beam acceleration requires a stable magnetic field – on the order of tens of ppm. Pulsed power can induce flicker (voltage variation) inside the treatment facility, affecting patient treatment, and on the utility supply grid, which is subject to regulatory control.

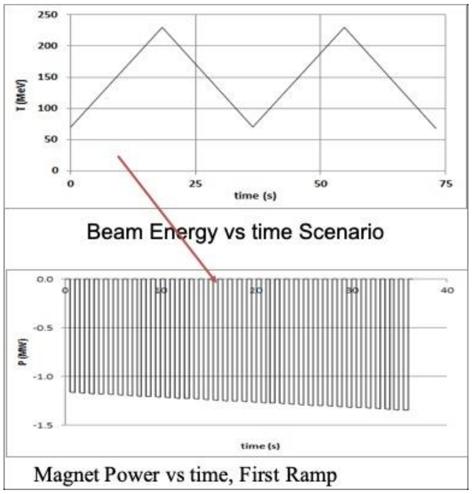

Fig. 82 Illustration of picket fencing requirement for magnet power supply system.

14.2 Power Supply Architecture

Picket fencing requires a high dynamic range on the order 0.5~1 kV during ramping with 2~3 V during plateau and alternating injection and removal of several MJ from magnet system during the ramp sequence. Fortunately, this is a non-unique circumstance as we have previously encountered this power supply scenario during operation of the C-MOD tokamak at the MIT Plasma Science and Fusion Center (PSFC). For that experiment the Toroid Field Coils required fast ramp to minimize resistive heating while a steady current/field needed for plasma confinement. At that time, in around 1989, K. Sueker (Robicon) developed an auto-tap changing power supply architecture to accommodate both requirements.

14.2.1 Auto-tap changing power supply

The original incarnation, shown in Fig. 83 had dual output stages in parallel, one connected to the high voltage transformer tap (for ramping), the other to a lower set of voltage taps (for steady operation). The output stages could be operated independently or in a cross-over mode.

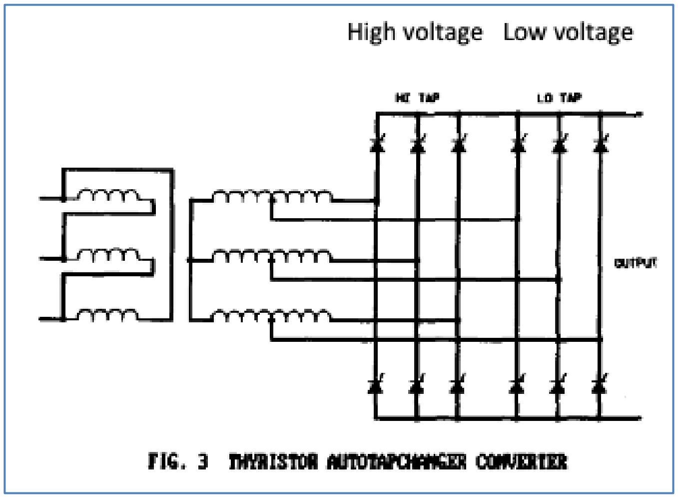

Fig. 83 Auto-tap changing power supply. K. Sueker, "Thyristor autotapchanger power supply for ALCATOR C-Mod Toroidal Field," IEEE 13th SOFE (1989)

14.2.2 Power quality concerns

The picket fence power time dependence creates power quality concerns. During the increasing magnetic field portion of the cycle, power can be pulled directly from the grid, but this can create power flicker issues. Alternatively, power can be pulled from an energy storage system, requiring a large energy storage system. One can also pull power from both the grid and storage offering, perhaps the lowest cost solution as shown schematically in Fig. 84. During the decreasing magnetic field portion of the cycle the energy can be returned to the storage system. One could also dissipate energy on the return cycle but this is inefficient and wasteful. Dumping energy back to the grid is generally prohibited by the power utility. The lowest impact on the utility grid is when power is drawn at the highest possible voltage and lowest current.

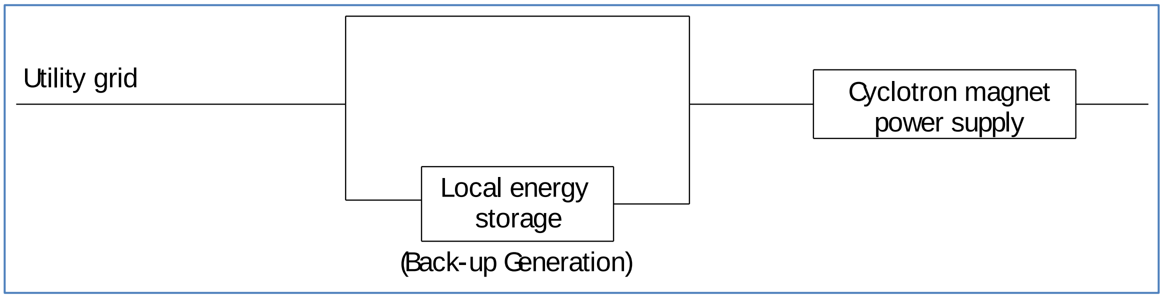

Fig. 84 Schematic one-line circuit diagram of a power system connected to both the utility grid and a local energy storage system. Prime power to magnet power system could be drawn directly from grid, from a local energy storage system, or by a combination of the two.

14.2.3 Energy Storage Options

The most efficient solution and the one which yields the highest power quality with minimum or no impact on the utility grid is by using an energy storage solution. There are at least two possible solutions:

1) **<u>Internal</u>** to the power supply, a previously developed option for fast pulsed synchrotrons in high energy and nuclear physics laboratories.

This option has been previously studied for the Brookhaven National Laboratory (BNL) fast cycle synchrotron. This design used a 0.7 F capacitive storage option at 6 kV (13 MJ) inside a power supply for fast ramped operation. A schematic of the circuit is shown in Fig. 85.

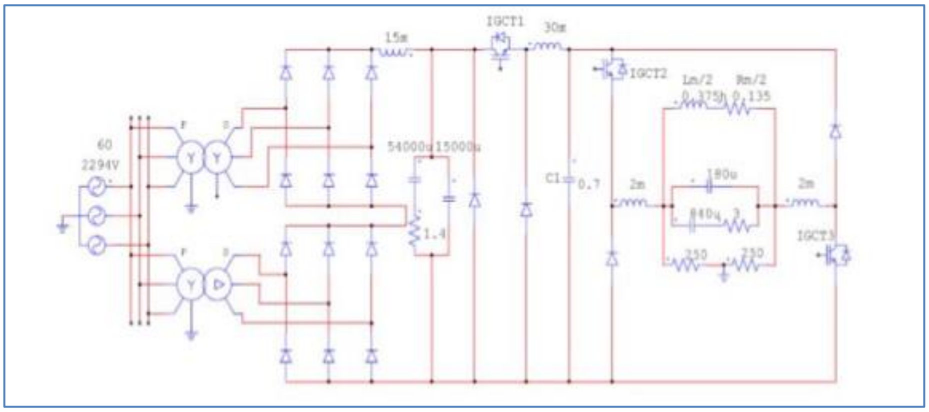

Fig. 85 BNL fast -ramp cyclotron schematic. I. Marneris, et. al, "Simulations of The AGS MMMPS Storing Energy in Capacitor Banks," MOPAS096 Proceedings of PAC07, Albuquerque, New Mexico, USA (2007).

2) **<u>External</u>** to the power supply. The most common option is a rotating flywheel coupled to an alternator/generator. Possible solutions may already exist in commercial back-up generators and uninterruptible power supplies.

a) Euro-Diesel “no-break” combines power quality enhancement with back-up power generation in a single unit. It would be possibility to incorporate this back-up solution into routine operation.

Some external backup systems are commercially available such as the Euro-Diesel (http://www.euro-diesel.com/) “no-break” power system which provides power quality correction in addition to back-up power capacity It uses a combination of rotating, energy storage unit with a back-up generator with a diesel drive. A photo of a Euro-Diesel system is shown in Fig. 86 and a cross-section of the stat-alternator is shown in Fig. 87.

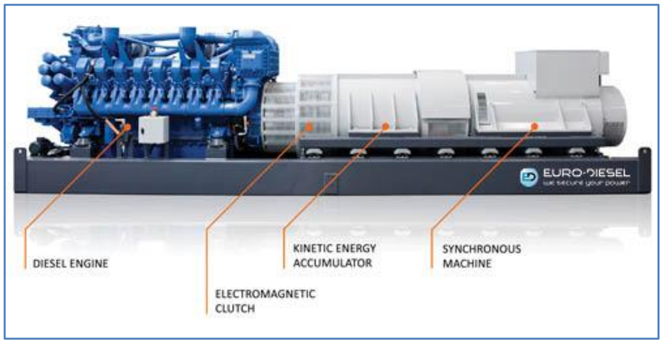

Fig. 86 The Euro-Diesel NO-BREAK KS® is made up of a diesel engine that is coupled to a stato-alternator, via an electromagnetic clutch. The stato-alternator is the combination of a kinetic energy accumulator and a synchronous machine.

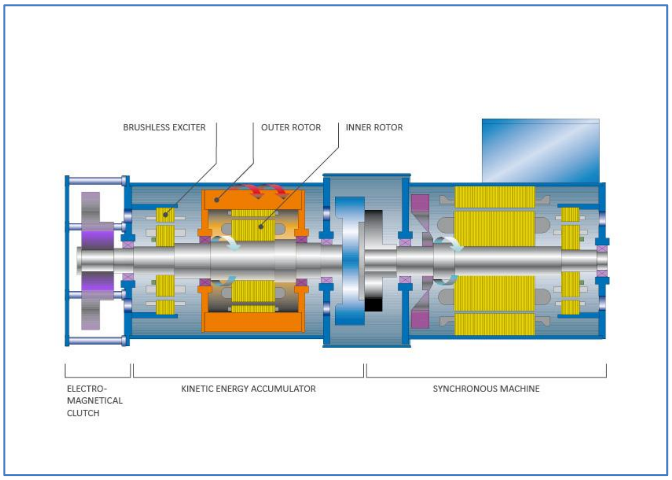

Fig. 87 Cross-section of the Euro-Diesel stato-alternator.

Note that back-up generation is already typically required for most medical systems. It might be possible to use this existing capacity for routine operation of the variable energy cyclotron.

15 Future work

The ironless cyclotrons are highly attractive for a wide range of applications, both for security (such as cargo interrogation) as well as for medical devices (hadron therapies, pet isotope production). To pursue the technology further, a detailed engineering design must be completed. Although feasibility has been demonstrated in this program, detailed designs of the different systems are required. Engineering analysis of the magnets, cryogenic systems, ion source, vacuum systems, RF and electrical systems, still need to be performed.

The engineering design phase would be followed by prototyping of the different systems, and integration of the components into a working prototype system. The working prototype which could then be commissioned and used for PBRT research purposes.

16 References

[1] R. R. Wilson, “Radiological uses of fast protons,” *Radiology*, vol. 47, no. 5, pp. 487–491, 1946.

[2] C. A. Tobias *et al.*, “Pituitary Irradiation with High-Energy Proton Beams A Preliminary Report*,” *CANCER Res.*, vol. 18, no. 2, pp. 121–34, 1958.

[3] “Workshop on Ion Beam Therapy Summary Report,” Bethesda, MD.

[4] A. W. Chao and W. Chou, Eds., “Reviews of Accelerator Science and Technology,” in *Reviews of Accelerator Science and Technology*, WORLD SCIENTIFIC, 2017, pp. i–vii.

[5] J. Cameron and N. Schreuder, “Smaller – lighter – cheaper: New technological concepts in proton therapy,” in *Ion Beam Therapy*, 2012, p. 673.

[6] H. Schneider, J. Fraser, and C. Bigham, “Superconducting cyclotrons,” *IEEE Trans. Magn.*, vol. 11, no. 2, pp. 443–446, Mar. 1975.

[7] D. Krischel *et al.*, “Design Aspects and Operation Experience With a Novel Superconducting Cyclotron for Cancer Treatment,” *IEEE Trans. Appl. Supercond.*, vol. 17, no. 2, pp. 2307–2310, Jun. 2007.

[8] J. H. Ormrod *et al.*, “Invited Paper: The Chalk River Superconducting Cyclotron,” 1979.

[9] H. G. Blosser, “The Michigan State University Superconducting Cyclotron Program,” *IEEE Trans. Nucl. Sci.*, vol. 26, no. 2, pp. 2040–2047, 1979.

[10] E. O. Lawrence, “Method and Apparatus for the Acceleration of Ions,” 1948384, 1934.

[11] E. O. Lawrence and M. S. Livingston, “The Production of High Speed Light Ions Without the Use of High Voltages,” *Phys. Rev.*, vol. 40, no. 1, pp. 19–35, Apr. 1932.

[12] T. A. Antaya, “High-Field Superconducting Synchrocyclotron,” US 7541905 B2, 2007.

[13] A. Antaya, Timothy, L. Radovinsky, Alexey, H. Schultz, Joel, H. Titus, Peter, A. Smith, Bradford, and L. Bromberg, “Magnet Structure for Parrticle Acceleration,” International Publication No. WO2007084701 A1, 27-Jul-2007.

[14] “http://www.mevion.com/about-mevion/treatment-centers.” [Online]. Available: http://www.mevion.com/about-mevion/treatment-centers.

[15] K. M. Subotic, “Multipurpose Air-Core Superconducting Cyclotrons,” in *EPAC 88 First European Particle Accelerator Conference*.

[16] H. Ueda *et al.*, “Conceptual Design of Next Generation HTS Cyclotron,” *IEEE Trans. Appl. Supercond.*, vol. 23, no. 3, pp. 4100205–4100205, Jun. 2013.

[17] A. Radovinsky, J. V. Minervini, C. E. Miller, L. Bromberg, P. C. Michael, and M. Maggiore, “Superconducting Magnets for Ultra Light and Magnetically Shielded, Compact Cyclotrons for Medical, Scientific, and Security Applications,” *IEEE Trans. Appl. Supercond.*, vol. 24, no. 3, 2014.

[18] L. Bromberg, J. V. Minervini, P. Le, L. Radovinsky, Alexey, P. C. Michael, and T. A. Antaya, “Ultra-Light, Magnetically Shielded, High -Current, Compact Cyclotron,” US 8975836 B2, 2015.

[19] Y. Lvovsky, E. W. Stautner, and T. Zhang, “Novel technologies and configurations of superconducting magnets for MRI,” *Supercond. Sci. Technol.*, vol. 26, no. 9, p. 093001, Sep. 2013.

[20] X. Wu, “Conceptual Orbit Dynamics in a 250 MeV Superconducting Synchrocyclotron,” Michigan State University, 1990.

[21] E. Pearson *et al.*, “Development of Cyclotrons for Proton and Particle Therapy,” in *Particle Radiotherapy : Emerging Technology for Treatment of Cancer*, A. K. Rath and N. Sahoo, Eds. Springer India, 2016, p. 21.

[22] L. Radovinsky, Alexey, “Baseline Build ab7a,” Cambridge, MA, ASGIC-MIT-ARadovinsky-150723-01, 2015.

[23] “Furukawa Electric Group, Low Temperature Superconductors, Catalog Page.” [Online].https://www.furukawa.co.jp/en/product/catalogue/pdf/superconductor_se001.pdf.

[24] A. Radovinsky, “Particle Acceleration in a Variable-Energy Synchrocyclotron by a Single-Tuned Variable-Frequency Drive,” US 10,028,369 B2, Jul. 17, 2018.

[25] M. Abs, “Variable Rotating Capacitor for Synchrocyclotron,” WO 2012/101143 Al, 2012.

[26] W. Kleeven, “The Superconducting Synchrocyclotron S2C2,” Part IV, MID 4223,” in *Joint University Accelerator School (JUAS-2015)*, 2015.

[27] T. Zhang *et al.*, “Beam Loss by Lorentz Stripping and Vacuum Dissociation in a 100 MeV Compact H- Cyclotron,” in *Particle accelerator. Proceedings, 23rd Conference, PAC’09, Vancouver, Canada, May 4-8, 2009*, 2010, p. FR5REP111.

[28] J.-P. Carneiro, B. Mustapha, and P. N. Ostroumov, “Numerical simulations of stripping effects in high-intensity hydrogen ion linacs,” *Phys. Rev. Spec. Top. - Accel. Beams*, vol. 12, no. 4, Apr. 2009.

[29] W. Kleeven *et al.*, “The IBA Supercondcuting Synchrocyclotron Project S2C2,” in *Proceedings of Cyclotrons 2013*, 2014, vol. MO4PB02, pp. 115–119.

[30] J. Van de Walle *et al.*, “The S2C2: From Source to Extraction,” in *Proceedings of Cyclotrons 2016*, 2017, vol. THB01, pp. 285–289.

[31] S. Henrotin *et al.*, “Commissioning and Testing of the First IBA S2C2,” in *Proceedings of Cyclotrons 2016*, 2017, vol. TUP07, pp. 178–180.

[32] “COMSOL Multiphysics®.” COMSOL AB.

[33] “Opera FEA Simulation Software.” .

[34] A. Adelmann, C. Krauss, Y. Ineichen, and J. J. Yang, “The OPAL (Object Oriented Parallel Accelerator Library) Framework.” Paul Scherrer Institut, Villigen, Switzerland, 2008.

[35] L. C. Teng and J. L. Tuck, “Magnetic Regenerative Reflector for Cyclotrons,” US2812463A, 1957.

[36] K. J. le Couteur, “The Regenerative Deflector for Synchrocyclotrons,” *Proc. Phys. Soc. Sect. B*, vol. 64, no. 12, pp. 1073–1084, Dec. 1951.

[37] A. C. Paul, “Study of a Multielement Regenerative Extraction System for the Berkeley 84-Inch Cyclotron,” Berkeley, 1970.

[38] G. Van Rossum and F. L. Drake, *Python 3 Reference Manual*. Paramount, CA: CreateSpace, 2009.

A. Appendix A

CICC TOOL Cable Design

NbTi-a for Circuit A

CICCTOOL-ASGIC-31MJ-3kA-6.56T-ab7a.xls

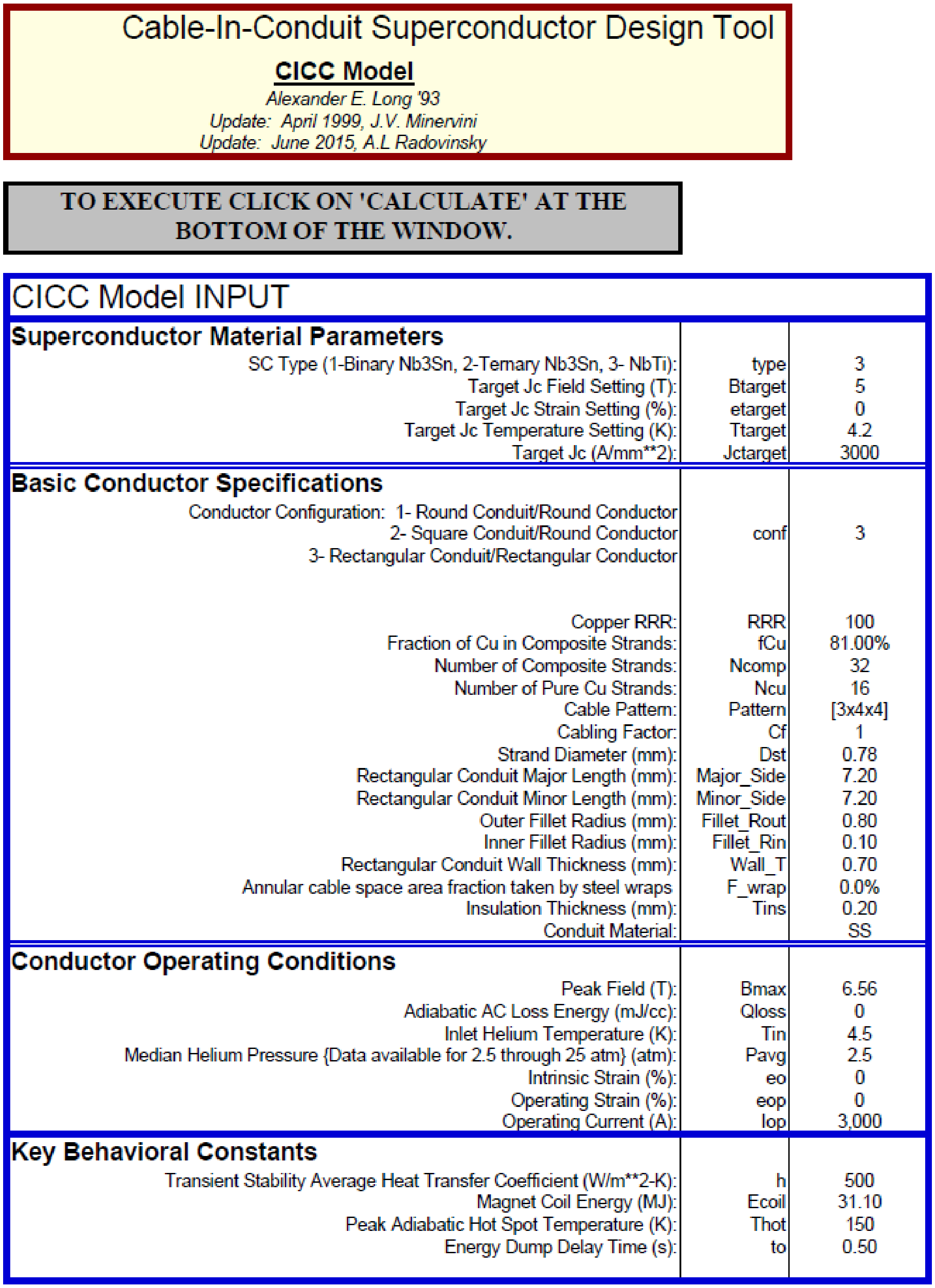

Cable-In-Conduit Superconductor Design Tool

CICC Model

Alexander E. Long '93
Update: April 1999, J.V. Minervini
Update: June 2015, A.L Radovinsky

TO EXECUTE CLICK ON 'CALCULATE' AT THE BOTTOM OF THE WINDOW.

CICC Model INPUT

Superconductor Material Parameters		
SC Type (1-Binary Nb3Sn, 2-Ternary Nb3Sn, 3- NbTi):	type	3
Target Jc Field Setting (T):	Btarget	5
Target Jc Strain Setting (%):	etarget	0
Target Jc Temperature Setting (K):	Ttarget	4.2
Target Jc (A/mm**2):	Jctarget	3000
Basic Conductor Specifications		
Conductor Configuration: 1- Round Conduit/Round Conductor 2- Square Conduit/Round Conductor 3- Rectangular Conduit/Rectangular Conductor	conf	3
Copper RRR:	RRR	100
Fraction of Cu in Composite Strands:	fCu	81.00%
Number of Composite Strands:	Ncomp	32
Number of Pure Cu Strands:	Ncu	16
Cable Pattern:	Pattern	[3x4x4]
Cabling Factor:	Cf	1
Strand Diameter (mm):	Dst	0.78
Rectangular Conduit Major Length (mm):	Major_Side	7.20
Rectangular Conduit Minor Length (mm):	Minor_Side	7.20
Outer Fillet Radius (mm):	Fillet_Rout	0.80
Inner Fillet Radius (mm):	Fillet_Rin	0.10
Rectangular Conduit Wall Thickness (mm):	Wall_T	0.70
Annular cable space area fraction taken by steel wraps	F_wrap	0.0%
Insulation Thickness (mm):	Tins	0.20
Conduit Material:		SS
Conductor Operating Conditions		
Peak Field (T):	Bmax	6.56
Adiabatic AC Loss Energy (mJ/cc):	Qloss	0
Inlet Helium Temperature (K):	Tin	4.5
Median Helium Pressure {Data available for 2.5 through 25 atm} (atm):	Pavg	2.5
Intrinsic Strain (%):	eo	0
Operating Strain (%):	eop	0
Operating Current (A):	Iop	3,000
Key Behavioral Constants		
Transient Stability Average Heat Transfer Coefficient (W/m**2-K):	h	500
Magnet Coil Energy (MJ):	Ecoil	31.10
Peak Adiabatic Hot Spot Temperature (K):	Thot	150
Energy Dump Delay Time (s):	to	0.50

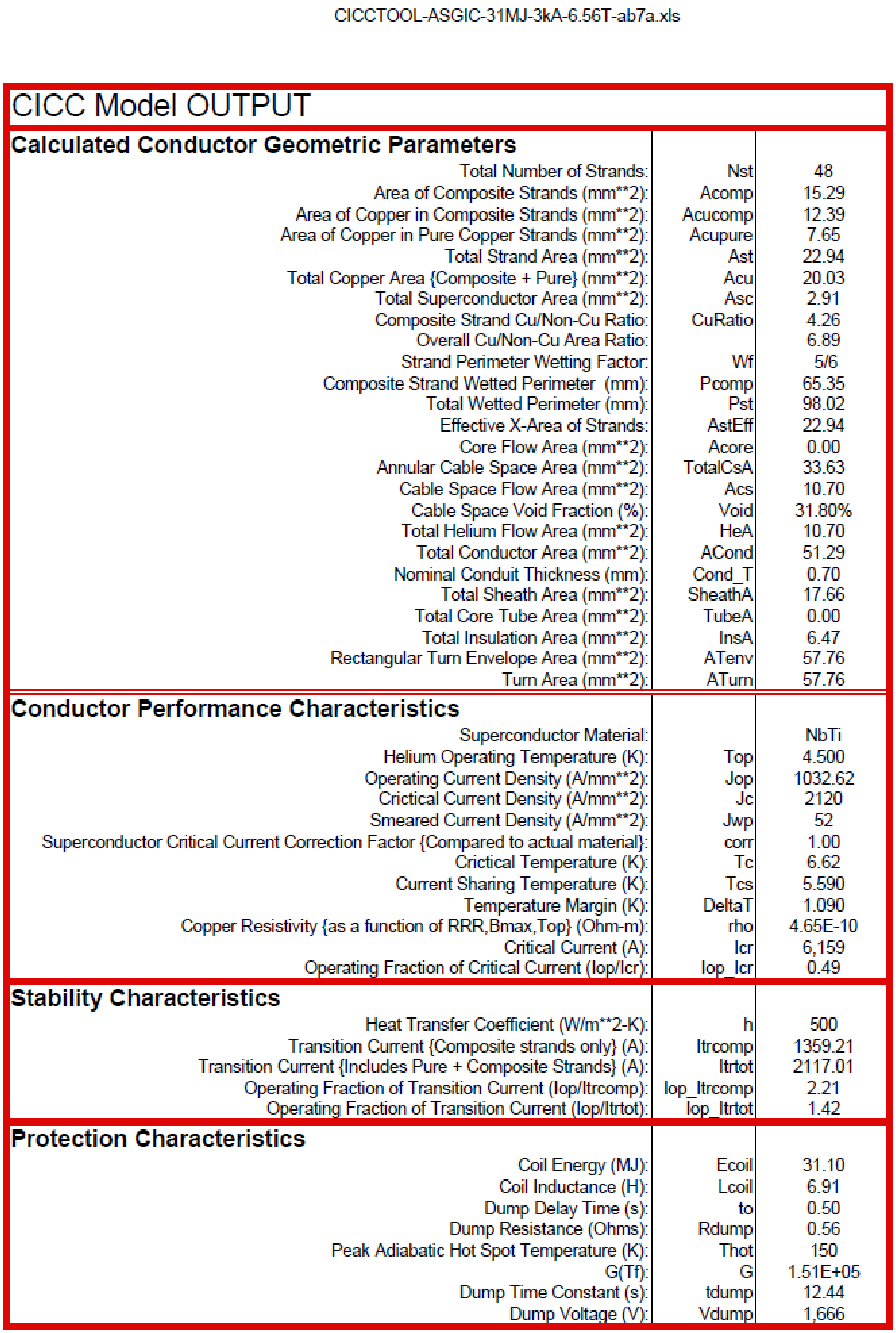

CICCTOOL-ASGIC-31MJ-3kA-6.56T-ab7a.xls

CICC Model OUTPUT		
Calculated Conductor Geometric Parameters		
Total Number of Strands:	Nst	48
Area of Composite Strands (mm**2):	Acomp	15.29
Area of Copper in Composite Strands (mm**2):	Acucomp	12.39
Area of Copper in Pure Copper Strands (mm**2):	Acupure	7.65
Total Strand Area (mm**2):	Ast	22.94
Total Copper Area {Composite + Pure} (mm**2):	Acu	20.03
Total Superconductor Area (mm**2):	Asc	2.91
Composite Strand Cu/Non-Cu Ratio:	CuRatio	4.26
Overall Cu/Non-Cu Area Ratio:		6.89
Strand Perimeter Wetting Factor:	Wf	5/6
Composite Strand Wetted Perimeter (mm):	Pcomp	65.35
Total Wetted Perimeter (mm):	Pst	98.02
Effective X-Area of Strands:	AstEff	22.94
Core Flow Area (mm**2):	Acore	0.00
Annular Cable Space Area (mm**2):	TotalCsA	33.63
Cable Space Flow Area (mm**2):	Acs	10.70
Cable Space Void Fraction (%):	Void	31.80%
Total Helium Flow Area (mm**2):	HeA	10.70
Total Conductor Area (mm**2):	ACond	51.29
Nominal Conduit Thickness (mm):	Cond_T	0.70
Total Sheath Area (mm**2):	SheathA	17.66
Total Core Tube Area (mm**2):	TubeA	0.00
Total Insulation Area (mm**2):	InsA	6.47
Rectangular Turn Envelope Area (mm**2):	ATenv	57.76
Turn Area (mm**2):	ATurn	57.76
Conductor Performance Characteristics		
Superconductor Material:		NbTi
Helium Operating Temperature (K):	Top	4.500
Operating Current Density (A/mm**2):	Jop	1032.62
Crictical Current Density (A/mm**2):	Jc	2120
Smeared Current Density (A/mm**2):	Jwp	52
Superconductor Critical Current Correction Factor {Compared to actual material}:	corr	1.00
Crictical Temperature (K):	Tc	6.62
Current Sharing Temperature (K):	Tcs	5.590
Temperature Margin (K):	DeltaT	1.090
Copper Resistivity {as a function of RRR,Bmax,Top} (Ohm-m):	rho	4.65E-10
Critical Current (A):	Icr	6,159
Operating Fraction of Critical Current (Iop/Icr):	Iop_Icr	0.49
Stability Characteristics		
Heat Transfer Coefficient (W/m**2-K):	h	500
Transition Current {Composite strands only} (A):	Itrcomp	1359.21
Transition Current {Includes Pure + Composite Strands} (A):	Itrtot	2117.01
Operating Fraction of Transition Current (Iop/Itrcomp):	Iop_Itrcomp	2.21
Operating Fraction of Transition Current (Iop/Itrtot):	Iop_Itrtot	1.42
Protection Characteristics		
Coil Energy (MJ):	Ecoil	31.10
Coil Inductance (H):	Lcoil	6.91
Dump Delay Time (s):	to	0.50
Dump Resistance (Ohms):	Rdump	0.56
Peak Adiabatic Hot Spot Temperature (K):	Thot	150
G(Tf):	G	1.51E+05
Dump Time Constant (s):	tdump	12.44
Dump Voltage (V):	Vdump	1,666

NbTi-b for Circuit B

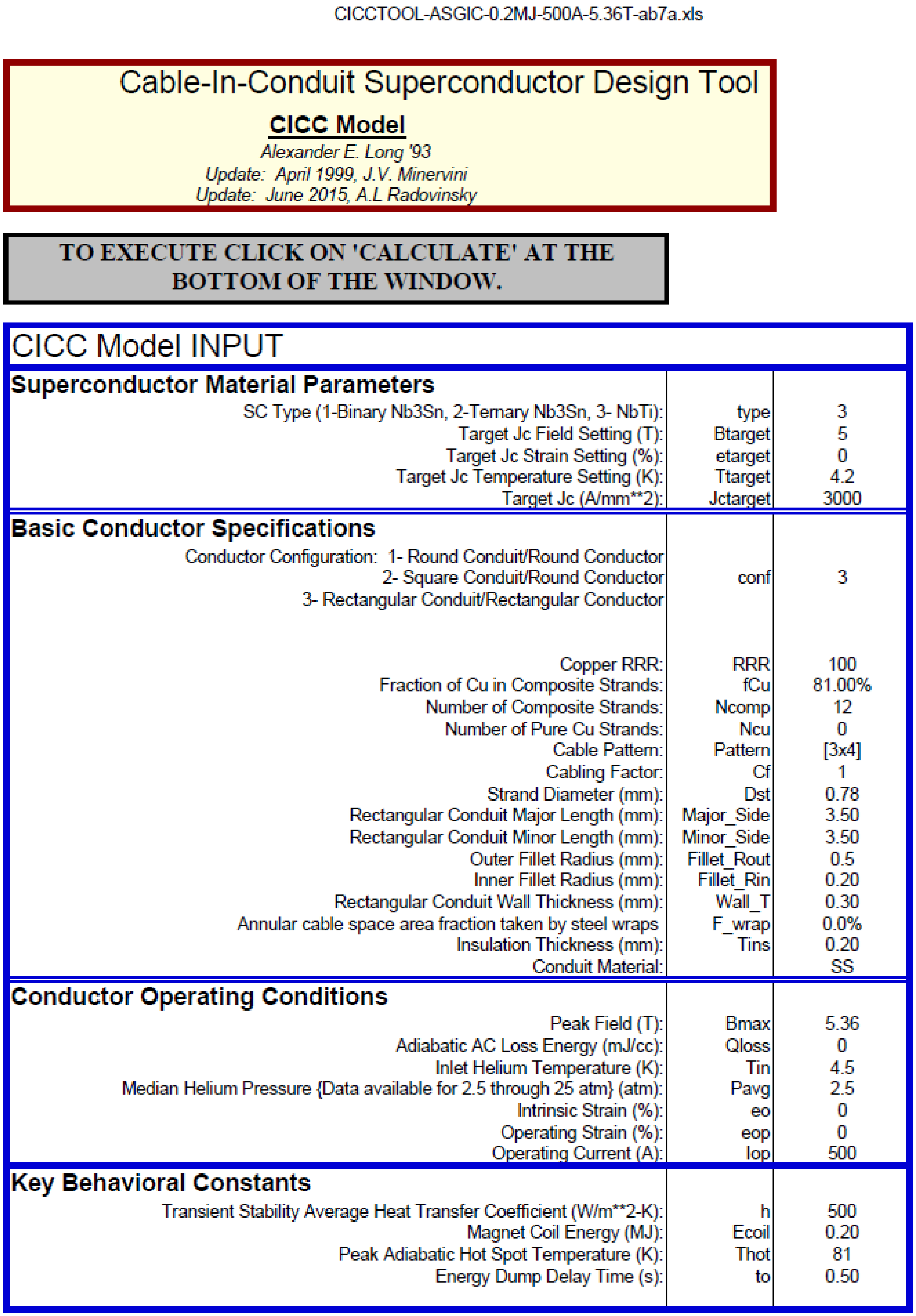

CICCTOOL-ASGIC-0.2MJ-500A-5.36T-ab7a.xls

Cable-In-Conduit Superconductor Design Tool

CICC Model

Alexander E. Long '93
Update: April 1999, J.V. Minervini
Update: June 2015, A.L Radovinsky

TO EXECUTE CLICK ON 'CALCULATE' AT THE BOTTOM OF THE WINDOW.

CICC Model INPUT

Superconductor Material Parameters		
SC Type (1-Binary Nb3Sn, 2-Ternary Nb3Sn, 3- NbTi):	type	3
Target Jc Field Setting (T):	Btarget	5
Target Jc Strain Setting (%):	etarget	0
Target Jc Temperature Setting (K):	Ttarget	4.2
Target Jc (A/mm**2):	Jctarget	3000
Basic Conductor Specifications		
Conductor Configuration: 1- Round Conduit/Round Conductor 2- Square Conduit/Round Conductor 3- Rectangular Conduit/Rectangular Conductor	conf	3
Copper RRR:	RRR	100
Fraction of Cu in Composite Strands:	fCu	81.00%
Number of Composite Strands:	Ncomp	12
Number of Pure Cu Strands:	Ncu	0
Cable Pattern:	Pattern	[3x4]
Cabling Factor:	Cf	1
Strand Diameter (mm):	Dst	0.78
Rectangular Conduit Major Length (mm):	Major_Side	3.50
Rectangular Conduit Minor Length (mm):	Minor_Side	3.50
Outer Fillet Radius (mm):	Fillet_Rout	0.5
Inner Fillet Radius (mm):	Fillet_Rin	0.20
Rectangular Conduit Wall Thickness (mm):	Wall_T	0.30
Annular cable space area fraction taken by steel wraps	F_wrap	0.0%
Insulation Thickness (mm):	Tins	0.20
Conduit Material:		SS
Conductor Operating Conditions		
Peak Field (T):	Bmax	5.36
Adiabatic AC Loss Energy (mJ/cc):	Qloss	0
Inlet Helium Temperature (K):	Tin	4.5
Median Helium Pressure {Data available for 2.5 through 25 atm} (atm):	Pavg	2.5
Intrinsic Strain (%):	eo	0
Operating Strain (%):	eop	0
Operating Current (A):	Iop	500
Key Behavioral Constants		
Transient Stability Average Heat Transfer Coefficient (W/m**2-K):	h	500
Magnet Coil Energy (MJ):	Ecoil	0.20
Peak Adiabatic Hot Spot Temperature (K):	Thot	81
Energy Dump Delay Time (s):	to	0.50

CICCTOOL-ASGIC-0.2MJ-500A-5.36T-ab7a.xls

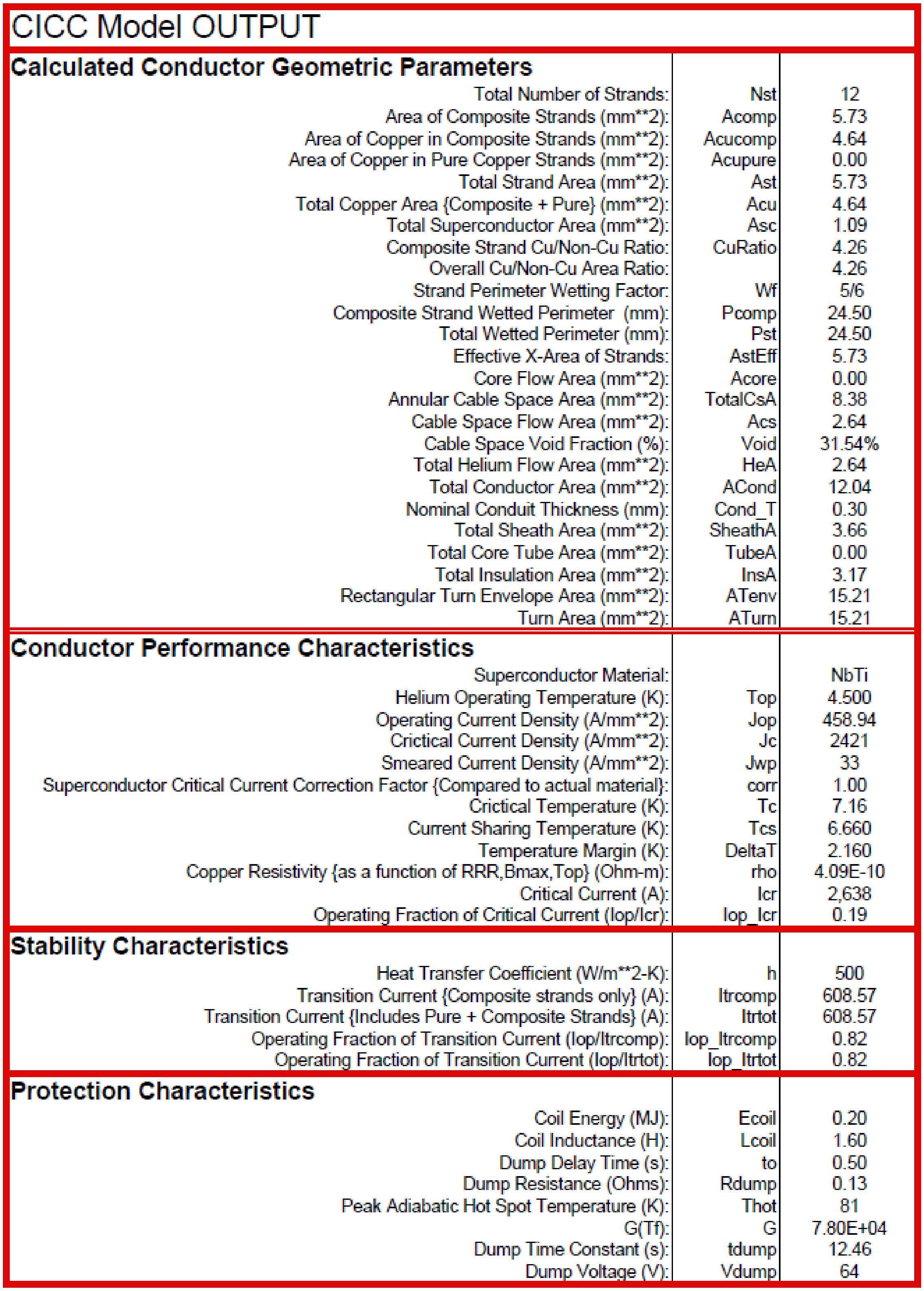

CICC Model OUTPUT		
Calculated Conductor Geometric Parameters		
Total Number of Strands:	Nst	12
Area of Composite Strands (mm**2):	Acomp	5.73
Area of Copper in Composite Strands (mm**2):	Acucomp	4.64
Area of Copper in Pure Copper Strands (mm**2):	Acupure	0.00
Total Strand Area (mm**2):	Ast	5.73
Total Copper Area {Composite + Pure} (mm**2):	Acu	4.64
Total Superconductor Area (mm**2):	Asc	1.09
Composite Strand Cu/Non-Cu Ratio:	CuRatio	4.26
Overall Cu/Non-Cu Area Ratio:		4.26
Strand Perimeter Wetting Factor:	Wf	5/6
Composite Strand Wetted Perimeter (mm):	Pcomp	24.50
Total Wetted Perimeter (mm):	Pst	24.50
Effective X-Area of Strands:	AstEff	5.73
Core Flow Area (mm**2):	Acore	0.00
Annular Cable Space Area (mm**2):	TotalCsA	8.38
Cable Space Flow Area (mm**2):	Acs	2.64
Cable Space Void Fraction (%):	Void	31.54%
Total Helium Flow Area (mm**2):	HeA	2.64
Total Conductor Area (mm**2):	ACond	12.04
Nominal Conduit Thickness (mm):	Cond_T	0.30
Total Sheath Area (mm**2):	SheathA	3.66
Total Core Tube Area (mm**2):	TubeA	0.00
Total Insulation Area (mm**2):	InsA	3.17
Rectangular Turn Envelope Area (mm**2):	ATenv	15.21
Turn Area (mm**2):	ATurn	15.21
Conductor Performance Characteristics		
Superconductor Material:		NbTi
Helium Operating Temperature (K):	Top	4.500
Operating Current Density (A/mm**2):	Jop	458.94
Crictical Current Density (A/mm**2):	Jc	2421
Smeared Current Density (A/mm**2):	Jwp	33
Superconductor Critical Current Correction Factor {Compared to actual material}:	corr	1.00
Crictical Temperature (K):	Tc	7.16
Current Sharing Temperature (K):	Tcs	6.660
Temperature Margin (K):	DeltaT	2.160
Copper Resistivity {as a function of RRR,Bmax,Top} (Ohm-m):	rho	4.09E-10
Critical Current (A):	Icr	2,638
Operating Fraction of Critical Current (Iop/Icr):	Iop_Icr	0.19
Stability Characteristics		
Heat Transfer Coefficient (W/m**2-K):	h	500
Transition Current {Composite strands only} (A):	Itrcomp	608.57
Transition Current {Includes Pure + Composite Strands} (A):	Itrtot	608.57
Operating Fraction of Transition Current (Iop/Itrcomp):	Iop_Itrcomp	0.82
Operating Fraction of Transition Current (Iop/Itrtot):	Iop_Itrtot	0.82
Protection Characteristics		
Coil Energy (MJ):	Ecoil	0.20
Coil Inductance (H):	Lcoil	1.60
Dump Delay Time (s):	to	0.50
Dump Resistance (Ohms):	Rdump	0.13
Peak Adiabatic Hot Spot Temperature (K):	Thot	81
G(Tf):	G	7.80E+04
Dump Time Constant (s):	tdump	12.46
Dump Voltage (V):	Vdump	64